WIDEBAND TWO-DIMENSIONAL AND MULTIPLE BEAM PHASED ARRAYS AND MICROWAVE APPLICATIONS USING PIEZOELECTRIC TRANSDUCERS

A Dissertation

by

SANG GYU KIM

Submitted to the Office of Graduate Studies of
Texas A&M University
in partial fulfillment of the requirements for the degree of

DOCTOR OF PHILOSOPHY

May 2005

Major Subject: Electrical Engineering

WIDEBAND TWO-DIMENSIONAL AND MULTIPLE BEAM PHASED ARRAYS AND MICROWAVE APPLICATIONS USING PIEZOELECTRIC TRANSDUCERS

A Dissertation

by

SANG GYU KIM

Submitted to Texas A&M University
in partial fulfillment of the requirements
for the degree of

DOCTOR OF PHILOSOPHY

Approved as to style and content by:

Kai Chang (Chair of Committee)	
Robert D. Nevels (Member)	Chin B. Su (Member)
Donald G. Naugle (Member)	Chanan Singh (Head of Department)

May 2005

Major Subject: Electrical Engineering

ABSTRACT

Wideband Two-Dimensional and Multiple Beam Phased Arrays and Microwave Applications Using Piezoelectric Transducers. (May 2005)

Sang Gyu Kim, B.S.; M.S., Kyungpook National University

Chair of Advisory Committee: Dr. Kai Chang

Modern satellite, wireless communication, and radar systems often demand wideband performance for multi-channel operation and the ability to steer multiple beams for multiple moving targets. This dissertation covers a variety of topics to design low-cost and wideband antenna systems. The main areas of study are microwave devices controlled piezoelectric transducers (PETs) and wideband baluns and balanced microwave circuits using parallel-strip lines. Some focus has also been given to the design of Rotman lens for multiple beam generation and Vivaldi antenna arrays for wideband two-dimensional scanning.

The dielectric perturbation technique controlled by PET is introduced to design a wideband phase shifter and a QPSK modulator, and to tune the resonant frequency of a slot dipole. The designed PET-controlled phase shifters are used for beam steering in a dual beam phased array using a bidirectional feeding scheme and a five-beam phased array using a microstrip Rotman lens.

Vivaldi-type antennas are commonly used to achieve wideband performance. Very wideband performance can be achieved using an antipodal tapered slot antenna because of its inherent simple wideband transition from microstrip line to parallel-strip line. An

antipodal tapered slot antenna and a phased array are designed to span 10 to 35 GHz. In addition, a 4×4 two-dimensional antenna array is designed using wideband antipodal tapered slot antennas, and two sets of PET-controlled phase shifters for *E*- and *H*-plane scanning are fabricated to steer the beam. As a microwave system using wideband antenna array, a new low-cost and wideband phased array radar is developed using a modulated pulse over 8 to 20 GHz band.

The double-sided parallel-strip line as a balanced line is presented. The parallel-strip line offers much flexibility for microwave circuit designs. This transmission line makes it possible to realize a low impedance line and allows the design of a compact wideband balun and junction. Wideband transitions (or baluns) from parallel-strip line to microstrip line, a typical unbalanced transmission line, are realized to cover several octave bandwidth. Balanced microwave filters and a hybrid coupler are developed using the parallel-strip line.

To my parents,
whose encouragement, love, and support have made all of this possible

ACKNOWLEDGMENTS

My first appreciation goes out to God, the Lord guiding my life.

I would like to express my deepest appreciation to Dr. Kai Chang for his support and guidance throughout my Ph.D. education at Texas A&M University. I also appreciate Dr. Robert D. Nevels, Dr. Chin B. Su, Dr. Donald G. Naugle, and Dr. Ugur Cilingiroglu for serving as members on my dissertation committee and for their helpful comments. I would like to thank the U.S. Army, the NASA Glenn Research Center, the Texas Telecommunications and Informatics Task Force (TITF), and the National Science Foundation for their financial support as a research assistantship. I gratefully acknowledge Mr. Ming-yi Li, Chunlei Wang, Chris Rodenbeck, Sam Kokel, and other members of the Electromagnetics and Microwaves Lab for their technical assistance, incentives, critical review of the papers, and invaluable discussions. I would also like to express my gratitude to Dr. Tae-Yeoul Yun of Hanyang University, Korea, for his invaluable discussions and help.

I would like to thank my parents, sister's family, and parents-in-law for their constant love, encouragement, and support. I also thank my son and daughter, Joonbum and Juyoung, for their love. Finally, my sincere thanks is given to my lovely wife, Hyekyoung, for all her patience, love, and support while completing this work. This work would not have been possible without their support and patience.

TABLE OF CONTENTS

Page

CHAPTER Page

CHAPTER Page

LIST OF FIGURES

FIGURE Page

FIGURE Page

FIGURE Page

FIGURE Page

FIGURE Page

LIST OF TABLES

CHAPTER I

INTRODUCTION

1. Introduction

Modern satellite, wireless communication, and radar systems often demand the wideband performance for multi-channel operation and the ability to steer multiple beams for multiple moving targets. Phased array antennas have proven useful for satellite communication systems and radar. Multiple beam antennas which use beam-switching techniques offer a less expensive and compact alternative to traditional phased arrays requiring more complex fabrication.

Because the beam is steered by controlling the phases at antenna elements, the phase shifter naturally becomes one of the most important components. Conventional solid-state, photonically controlled, or ferroelectric phase shifters are narrowband, lossy, or provide small phase shift [1]. A multi-line phase shifter controlled by a piezoelectric transducer (PET), published recently, enables the design of a phased array with low-cost, low-loss, wideband performance, and easy fabrication [1]. This technique uses electronically perturbed microstrip lines. The perturbation is controlled by the small movement achieved using PET. Additionally, the dielectric perturbation technique using PET can also be used to realize phase modulation, or to tune the operating frequency of a resonant antenna or microwave circuit.

The journal model for this dissertation is *IEEE Transactions on Microwave Theory and Techniques*.

Numerous techniques have been reported to generate multiple beams [2-15]. Typical techniques include lens-based beamformers such as Ruze, Rotman, and R-KR, as well as circuit-based beamformers including Blass and Butler matrix [16]. Dielectric lenses such as a Luneberg lens also can be used, though are expensive to manufacture at millimeter-wave frequencies [2, 3]. Multi-point feedings have been used widely to achieve circular polarization or cross-polarization suppression in a single antenna, or to synthesize different polarized multiple beams in microstrip patch arrays [17]. However, little has been reported for bi-directional feeding to achieve same-polarized multiple beams. In this research, a dual beam and a five-beam phased array are designed using new techniques. A bi-directionally-fed microstrip patch array is designed to make dual beams, and a sum/difference pattern is synthesized using a rat-race coupler. A microstrip Rotman lens is designed to generate five beams and the beams are steered using PET-controlled phase shifters.

Vivaldi-type antennas are commonly used to achieve wideband performance [18-28]. However, a balun is necessary to feed the antenna, and the bandwidth is limited by the transition performance. Very wideband performance can be achieved using an antipodal tapered slot antenna because of its inherently simple wideband transition from microstrip line to parallel-strip line. Antipodal tapered slot antennas and arrays are designed to cover from 10 to 35 GHz in this research.

Two-dimensional beam steering techniques are frequently required in satellite communications and target tracking radar. Present-day technology results in very high cost and complex systems. A simple and low-cost scheme to steer a beam in two-

dimensions is realized and tested. A 4×4 two-dimensional antenna array is designed using a wideband antipodal tapered slot antenna, and two sets of PET-controlled phase shifters for *E*- and *H*-plane scanning are fabricated to steer the beam. Additionally, a new low-cost and wideband phased array radar is developed using a modulated pulse over the 8 to 20 GHz band.

A balanced line such as coplanar stripline is often useful to feed printed antennas, or to fabricate lumped devices on planar circuits [29-30]. However, coplanar striplines have considerable limitations: (1) to realize low characteristic impedance requires extremely narrow strip or slot dimensions; and (2) to design planar microwave components such as power dividers and junctions requires complex circuit structures compared with their microstrip counterparts. As a balanced line, the parallel-strip line makes it possible to realize a low impedance line. It also allows the design of compact wideband baluns and junctions. In this research, wideband transitions (or baluns) from parallel-strip line to microstrip line, a typical unbalanced transmission line, are realized, and a microwave filter and hybrid coupler are developed using parallel-strip lines.

A PET is a promising candidate for microwave and millimeter-wave devices to satisfy the requirements such as low cost, small size, light weight, wide operating frequency range, and low power consumption. In this dissertation, new beam steering schemes and microwave applications using PET have been developed. This chapter will introduce the fundamental concept of the PET bender which is used in this research.

2. Piezoelectric transducer (PET)

Piezoelectricity is defined as "electric polarization produced by mechanical strain in crystals belonging to certain classes, the polarization being proportational to the strain and changing sign with it" [31]. It was discovered in 1880 by Pierre and Jacques Curie during their systematic study of the effect of pressure on the generation of electrical charge by crystals such as quartz, zinc blende, tourmaline, and Rochelle salt. Two effects are manifest in piezoelectricity: the direct effect and the converse or inverse effect. The direct effect is identified with the phenomenon whereby electrical charge (polarization) is generated from a mechanical stress, whereas the converse effect, which will be applied for this research, is associated with the mechanical movement generated by the application of an electrical field.

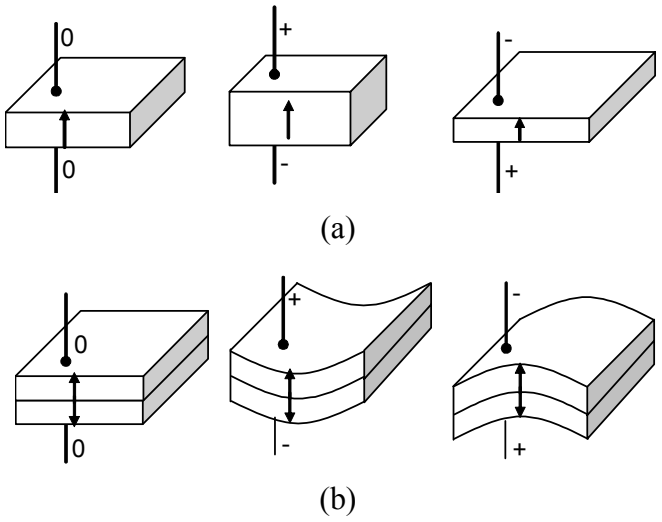

Fig. 1. Mechanical deformation of piezoelectric plates by an external electric field; (a) expansion and contraction in thickness and length, (b) bending.

In Fig. 1 (a), thickness expansion or contraction in a plate occurs when the electric field is alternately positive or negative. When two plates are cemented together and activated as Fig. 1(b), one plate will contract and the other will simultaneously expand producing a bending action. Mechanical displacement (twist, bending, expansion/contraction) occurs by the applied voltage and the polarization of material. Electric/mechanical characteristics are changed according to the composition ratio of piezoelectric material. Fig. 2 shows the structure of the PET to be used in this research.

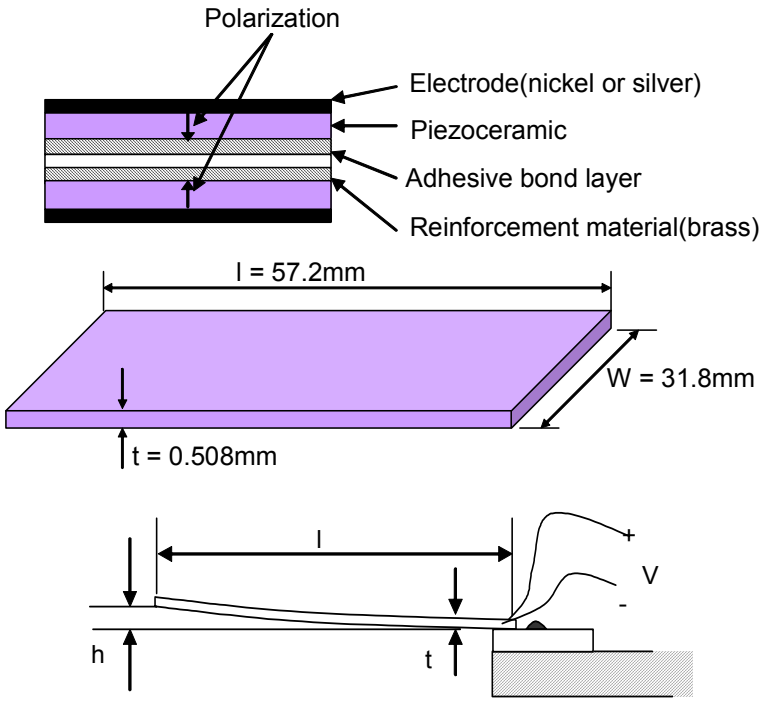

Fig. 2. PET bender moving up/down by external voltage.

The deflection at the end of the cantilevel piezoelectric bender in Fig. 2 is calculated as [1]

$$h = 4d_{31} \times \frac{l^2}{t^2} \times V$$

where, the mechanical strain coefficient d_{31} is 1.9×10^{-7} mm/V for the piezoceramic used in this research, and V is the applied voltage. The length L and the thickness t of PET are 57.2 mm and 0.508 mm, respectively. At maximum voltages V of ±90 V, the deflection is ±1.3 mm which are the maximum values for the PET used here.

3. Research conducted and accomplishments

Using the PET bender introduced above, new beam steering schemes and microwave applications are demonstrated. The research conducted is summarized in the following.

A. PET-controlled devices for microwave applications

Recently, a new phase shifter using a piezoelectric transducer (PET)-controlled dielectric layer to perturb the electromagnetic fields of a microstrip line was developed [1, 32]. An increased phase shift is achieved using a PET-controlled perturbation on coplanar waveguide (CPW), rather than on microstrip [33]. The electromagnetic fields on CPWs are less confined than those on microstrip lines, thereby making them more sensitive to perturbers placed above the guide. As other applications, novel dielectric perturbing and frequency tuning techniques using PET are introduced to design a low-loss QPSK modulator and a frequency agile slot dipole [34-35]. The resonant frequency of a slot dipole is shifted by the effective dielectric constant of the slot varied using an external dielectric perturbation. The air gap between the slot dipole substrate and the

perturber attached to the PET is varied by an external voltage. This gap changes the effective dielectric constant of the substrate, causing the different electrical length of the slot dipole. This technique thus provides the ability to change the resonant or operating frequency.

B. Dual beam phased array and monopulse antenna using bi-directionally-fed microstrip patch array

An independently controllable dual beam phased array with the same polarization is designed. A single or dual beam is synthesized by controlling the phases on both sides of a series-connected microstrip patch array. Two beams having the same polarization are obtained by feeding both sides of four series fed 1×8 microstrip patch antenna arrays, and each beam is steered in the *H*-plane using two PET-controlled phase shifters [36]. Additionally, a simple-structured bi-directionally-fed microstrip patch array is designed to achieve a sum/difference pattern [37]. A sum/difference pattern with an excellent front-to-back ratio and low cross-polarization levels is realized by adjusting the phases of the input signals to both sides of a bi-directionally-fed microstrip array.

C. Multiple beam phased array

A simple and low-cost multiple beam phased array to overcome the drawbacks of the switched beam antenna array is designed using a microstrip Rotman lens and PET-controlled phase shifter [38]. A microstrip Rotman lens with five beam ports and nine array ports is used as a feed for a multiple beam antenna to make the scan angle of 0°, ±15°, and ±30° at *Ka*-band. Using two PET-controlled phase shifters, the five beams are

steered ±8° completely covering ±38° from the broadside.

D. Design of wideband antenna array and two-dimensional beam steering

An antipodal exponentially-tapered slot antenna (ATSA) is designed to achieve two octaves of bandwidth, and low-cost one- and two-dimensional beam scannings are demonstrated using ATSA arrays and PET-controlled phase shifters [39-40]. A 4×4 ATSA array is designed for two-dimensional scanning, and the beam is steered using two sets of PET-controlled phase shifters. One set consisting of four identical PET-controlled phase shifters is used to steer the beam in the *E*-plane, and the other is used for the *H*-plane. Using two sets of PET-controlled phase shifters, the beam is steered over 30° in both planes. A wideband 1×4 *H*-plane phased array is also designed for a multi-channel communication system at 10 to 35 GHz band.

E. Microwave circuits using parallel-strip lines

A double-sided parallel-strip line as a balanced line is introduced to realize very wideband transition from microstrip line and balanced circuits. The ultra wideband microstrip to double-sided parallel-strip transitions using simply tapered ground strips are designed. Several new microwave circuits including a bandpass filter, a lowpass filter, and a rat-race hybrid are designed as examples of new balanced circuits using parallel-strip lines [41].

F. Wideband low-cost phased array radar

A new low-cost and wideband phased array radar is developed. The radar system uses a modulated pulse over 8 to 20 GHz band, and consists of PET-controlled phase

shifters, microwave monolithic integrated circuits (MMIC) of power amplifier and low noise amplifier, and ATSA arrays.

4. Dissertation organization

This dissertation presents new multiple beam steering technique, two-dimensional beam scanning scheme, wideband phased antenna array, microwave applications using PET, and balanced microwave circuits. The dissertation consists of eight chapters.

Chapter II presents several microwave devices controlled by PET. A PET-controlled phase shifter is designed on CPW to achieve the increased phase shift. Relative phase shifts on microstrip line and CPW of the same length are compared. As other applications, novel dielectric perturbing and frequency tuning techniques using PET are introduced to design a low-loss QPSK modulator and a frequency agile slot dipole.

Chapter III introduces a bi-directional feeding scheme on a series-connected microstrip patch antenna array. Dual beam and sum/difference pattern are synthesized using bi-directional feeding scheme. This technique is applied to fabricate a dual beam phased array and monopulse antenna.

Chapter IV describes a multiple beam phased array using the PET-controlled phase shifter and Rotman lens. The PET-controlled phase shifter and lens design are discussed.

Chapter V discusses a wideband antenna array and two-dimensional beam scanning scheme. An ATSA is designed to cover from 10 to 35 GHz, and a low-cost two-dimensional beam steering is demonstrated using two sets of PET-controlled phase

shifters.

Chapter VI introduces new microwave circuits using parallel-strip lines. The parallel-strip line as a planar transmission line is analyzed, and microwave filters and coupler using parallel-strip line are developed.

Chapter VII contains a wideband low-cost phased array radar with the design and measured data.

Chapter VIII summarizes the research accomplishments in this dissertation, and presents conclusions and recommendations for further research.

CHAPTER II*

PIEZOELECTRIC TRANSDUCER CONTROLLED DEVICES FOR MICROWAVE APPLICATIONS

1. Introduction

A phase shifter is one of important components in microwave and millimeter wave systems. It is commonly used for beam steering and beam forming for antenna arrays, timing recovery circuits, phase equalizers, etc. Therefore it naturally requires wideband and low loss characteristics. Most of published results using MMIC, ferroelectric, and solid state phase shifters show narrow bandwidths, high losses, or small phase shifts [1].

Recently, a new phase shifter using a piezoelectric transducer (PET)-controlled dielectric layer to perturb the electromagnetic fields of a microstrip line was published [1, 32]. By the fact that the characteristic impedance of the line is only slightly affected by perturbation, this phase shifter could be used in very wideband applications[32]. In this research, an increased phase shift is realized using a PET-controlled perturbation on CPW rather than on microstrip. The electromagnetic fields on CPW are less confined

---

than those on microstrip lines, thereby making them more sensitive to perturbers placed above the guide [42].

As an another application using the dielectric perturbation controlled by PET, a low-loss phase modulator is introduced. A binary-phase-shift-keying (BPSK) or quadri-phase-shift-keying modulator (QPSK) can be designed using PET-controlled phase shifters with 90° and 180° phase shifts. I/Q data can be modulated directly on a carrier signal. This modulator has the advantages of low loss, high power handling capability, low power consumption, and simple structure. However, the data rate is limited by the response time of PET, which is in the order of milli-second.

Tunable devices can be also useful in many microwave applications. However, whatever the method of tuning may be, they must conserve as much as possible their original *S*-parameters and output characteristics over a tuning range [43]. Most tunable microwave devices described in literatures are categorized in four types [44]: mechanically, magnetically, electrically, and optically tuning.

Microstrip dipoles have the drawback of inherently narrow bandwidth due to resonant characteristics, while possessing desirable properties such as simplicity, small size, and good linear polarization. Many efforts have been tried to increase the bandwidth of resonant antenna elements [45-50]. These techniques use a variable capacitance of varactor with a bias voltage, or change the electrical length of antenna using a switching element such as a pin diode inserted serially in a dipole antenna. Magill et al. used a dielectric sheet spaced in front of the array to reduce the variation of reflection coefficient with scan angle [50]. In this research, a frequency tunable CPW-

fed slot dipole antenna using a PET is designed and measured as a simple technique to change the resonant frequency. The air gap between the substrate for slot dipole and the perturber attached on a PET is varied due to an external voltage. This gap changes the effective dielectric constant of the substrate, causing the different electrical length of the slot dipole. This technique thus provides a tuning ability to change the resonant or operating frequency.

2. Wideband phase shifter controlled by PET

A. Design

A PET-controlled dielectric layer is used to perturb the electromagnetic fields of CPW. A perturber attached to a PET plate is deflected in the up/down direction under an external voltage, as shown in Fig. 3. The air gap between the CPW and the perturber is changed. This varies the effective dielectric constant of the CPW and causes a different phase shift. The PET is composed of Lead Zirconate Titanate and has dimensions of 70 mm (length) × 31.8 mm (width) × 0.508 mm (thickness).

The substrate used for CPW and microstrip is an RT/Duroid 6010.5 with a dielectric constant of 10.5 and a height of 0.635 mm. The CPW has a width of 0.42 mm, a gap of 0.254 mm, and a length of 74 mm. The same length is used in microstrip line for comparison, and the line width of microstrip is 0.56 mm. The characteristic impedances are 54 Ω and 52 Ω for microstrip line and CPW, respectively. The dielectric perturber used has a dielectric constant of 6.15, a height of 1.27 mm, and a length of 25.4 mm.

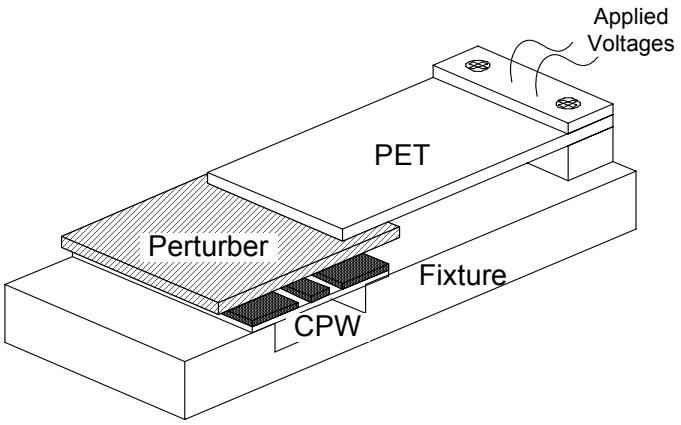

Fig. 3. Configuration of a phase shifter using dielectric perturbation controlled by a PET on CPW.

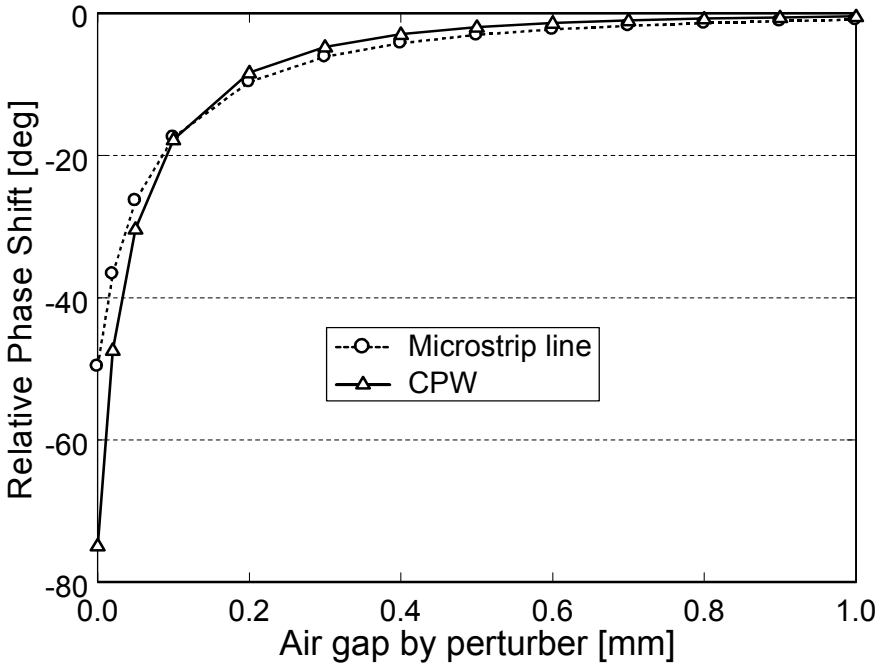

Fig. 4. Simulated relative phase shift as a function of air gap between the transmission line (CPW and microstrip) and perturber at 5 GHz.

A commonly available software, PCAAMT [51], which uses a full-wave spectral domain moment method, is used to calculate the effective dielectric constant of the multilayered transmission line using CPW and microstrip. Fig. 4 shows the simulated results in both CPW and microstrip line. The phase shift in CPW is 50% larger than that in microstrip line at maximum perturbation.

B. Measurements

An Agilent 8510C network analyzer is used to measure the phase shift and *S*-parameters, and Thru-Reflect-Line (TRL) calibration is used to remove the effect of the coaxial connectors to the CPW/microstrip line transitions. Fig. 5 shows the measured and simulated relative phase shifts, which are the phase difference between the perturbed line and the unperturbed CPW or microstrip line. The maximum phase shifts along the CPW and microstrip line are 75° and 50°, respectively. The phase shift of CPW is 50 % larger than that of microstrip line.

Fig. 6 shows the insertion loss (S_{21}) and return loss (S_{11}) for the CPW line with and without perturbation. The return loss and insertion loss are better than 10 dB and 1 dB, respectively, up to 6.5 GHz. The characteristic impedances of the line, which are calculated using the spectral-domain analysis of the moment method, change from 54 Ω to 48 Ω in microstrip line and 52 Ω to 43 Ω in CPW by perturbation. As the characteristic impedance of the line is relatively insensitive to the air-gap variation, the *S*-parameters does not change much by perturbation.

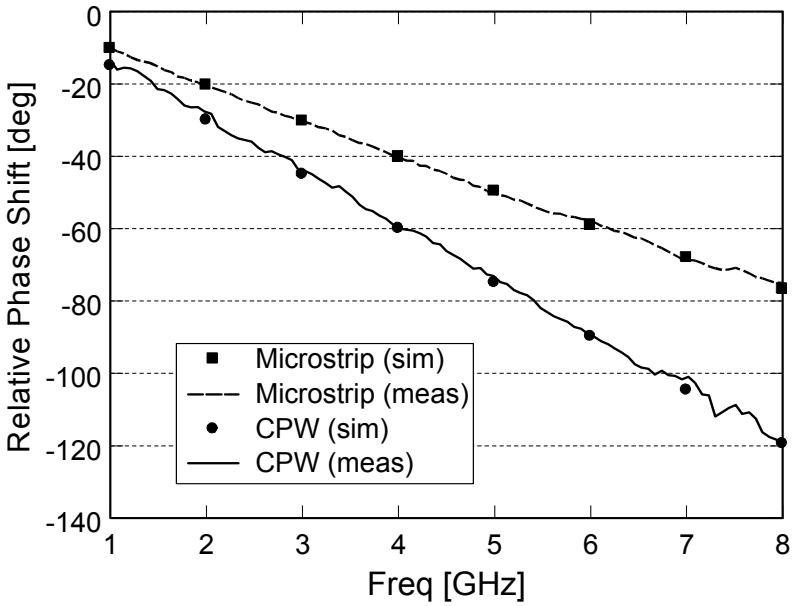

Fig. 5. Relative phase shifts in microstrip line and CPW (at maximum perturbation). Both simulated and measured results are shown.

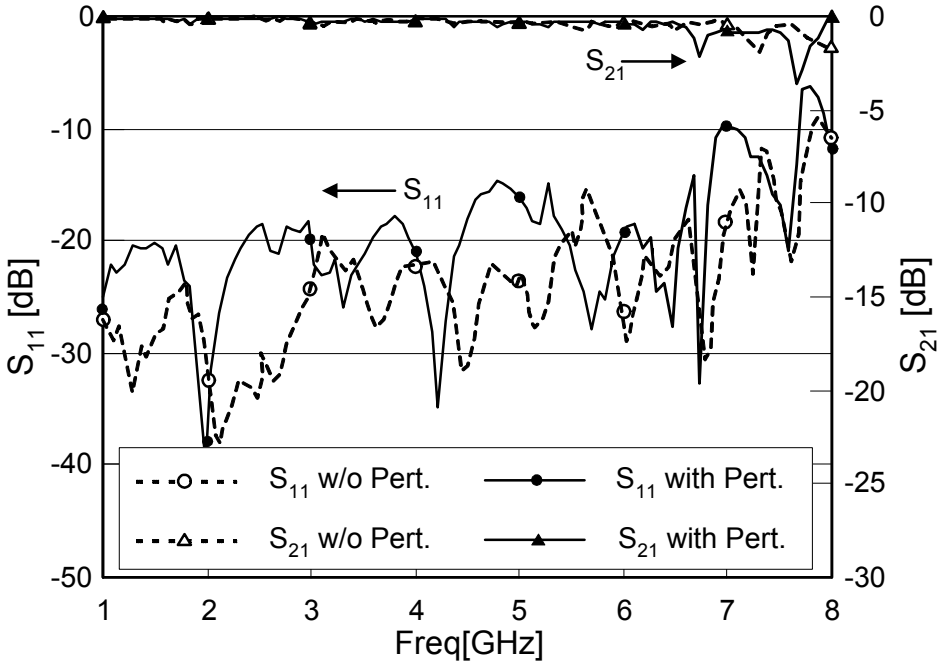

Fig. 6. *S*-parameters of the CPW phase shifter with the maximum perturbation and without perturbation.

Fig. 7 shows the relative phase shifts with respect to the unperturbed case for the applied voltages from 0 V to 40 V. The amount of phase shift depends on the voltage-controlled PET deflection. A non-zero phase shift at 0 V is due to the initial alignment of PET. A larger phase shift can be achieved by a perturber with a higher dielectric constant not larger than that of a substrate.

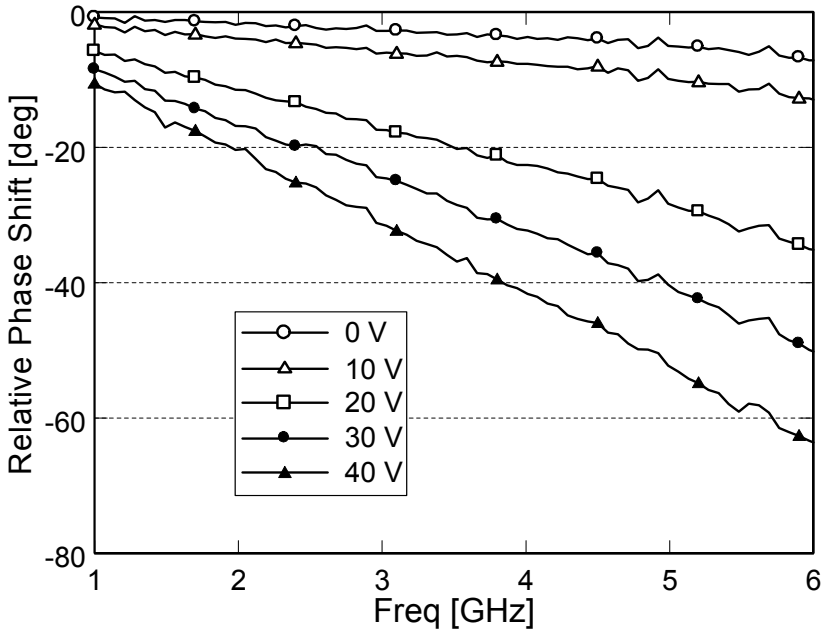

Fig. 7. Relative phase shift vs. frequency at different PET voltages.

3. Simple microwave QPSK modulator using PET

A. Design

Fig. 8 shows the QPSK modulator controlled by two PETs for I/Q modulation. The dielectric perturber attached to a PET is deflected by an external voltage. This voltage

causes the air gap between the microstrip line and perturber to change. An RT/Duroid 6002 with a dielectric constant of 10.2 and thickness of 1.27 mm is used as the dielectric perturber for the PET-controlled QPSK modulator.

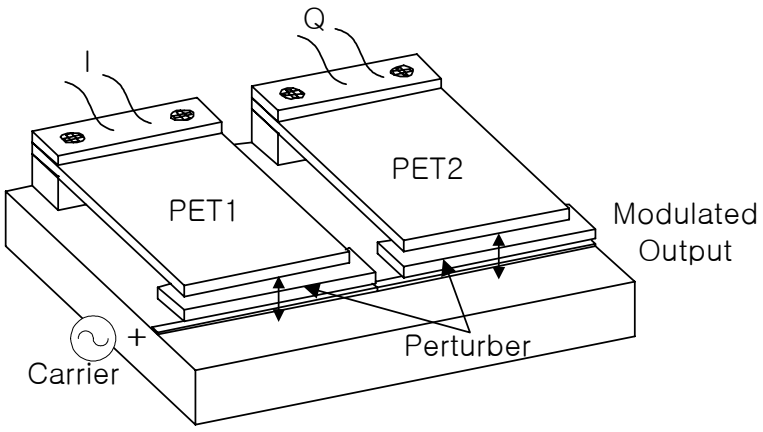

Fig. 8. Configuration of QPSK modulator.

Because the phase shift is proportional to the coverage length of the perturber, the lengths of the perturber over microstrip line are designed as 30 mm and 15 mm at I/Q modulator to achieve 180° and 90° phase responses at 15 GHz, respectively. The differential phase shift $\Delta\phi$ on a microstrip line caused by dielectric perturbation is calculated as

$$\Delta\phi = L_1 \cdot \frac{2\pi}{\lambda_o}\left(\sqrt{\varepsilon_{eff}(f)} - \sqrt{\varepsilon'_{eff}(f)}\right) \tag{1}$$

where L_1 is the length of perturber over a microstrip line, and $\varepsilon_{eff}(f)$ and $\varepsilon'_{eff}(f)$ are the effective relative permittivities of the unperturbed and perturbed microstrip line, respectively. However, a permittivity of the perturber should be less than that of the

substrate to reduce the loss due to leaky wave mode generation at a high frequency range (over 20 GHz) [33]. Table 1 shows the designed specification of the modulator, and the PETs are tuned to use the external voltages of ±25V for I/Q data.

Table 1. QPSK modulator using PETs

Data input		Applied voltages to PET (V)		Phase response (°)
I	Q	I	Q	
0	0	-25	-25	0
0	1	-25	+25	90
1	0	+25	-25	180
1	1	+25	+25	270

B. Measurements

The substrate used for the QPSK modulator is an RT/Duroid 5880 with a dielectric constant of 2.2 and thickness of 0.254 mm. Figs. 9 and 10 show the measured *S*-parameters and differential phase shifts, respectively. The measured return loss of the modulator with full perturbation is better than 10 dB at 15 GHz. The measured results include the effects of connectors and assembling errors. The differential phase shift is defined as the difference from the phase at the data '00', which means the unperturbed state using -25V at both PETs. The modulator exhibits a maximum insertion loss of 3.5 dB with full perturbation by both perturbers and the phase shifts of 90°, 180°, and 270° at 15 GHz. The phase error is around 3°.

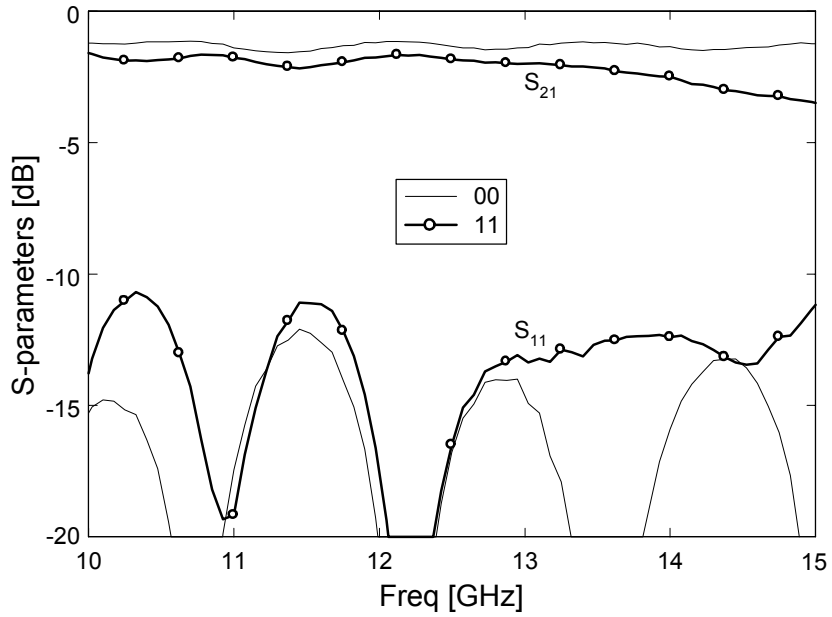

Fig. 9. Measured *S*-parameters of the QPSK modulator.

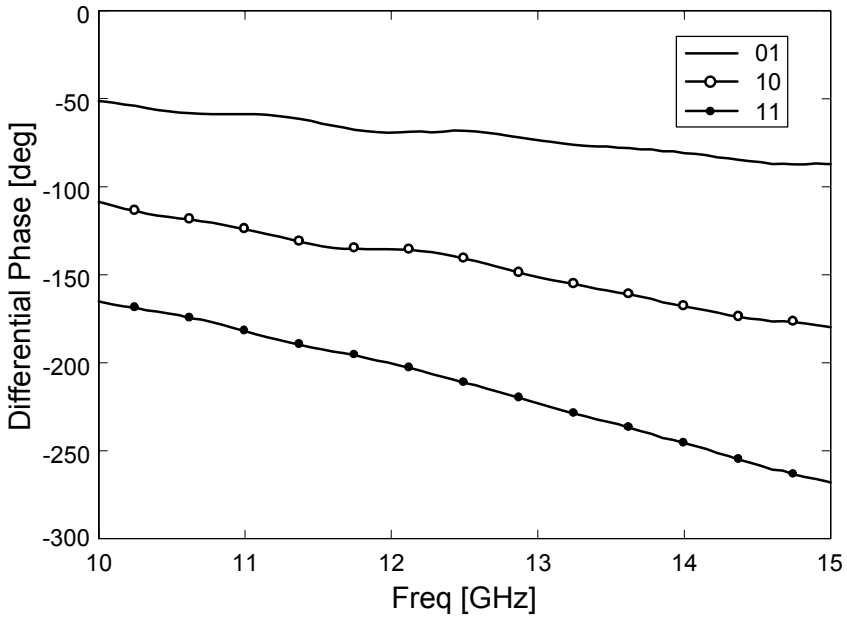

Fig. 10. Measured phase responses of the QPSK modulator.

The maximum data rate is limited by the response time of PET, which is dependent on the physical size. Fig. 11 shows the setup for the measurement of response time. The results given by an oscilloscope (LeCroy 9314AM) is shown in Fig. 12. When an external voltage (P1) is applied to a PET, the conductor attached on the one side of a PET is moved down connecting two microstrip lines. The probe 2 (P2) measures the voltage drop at the microstrip line. The measured response time of the PET used (57.2 [mm] × 31.8 [mm]) is 2.87 msec using an external voltage of 50 V as shown in Fig. 12, achieving the maximum data rate of 600 Hz. However, the response time can be reduced by using smaller PETs.

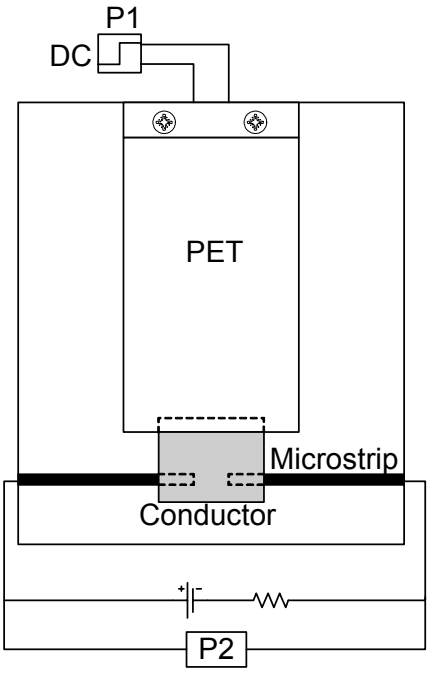

Fig. 11. Setup diagram for the measurement of response time.

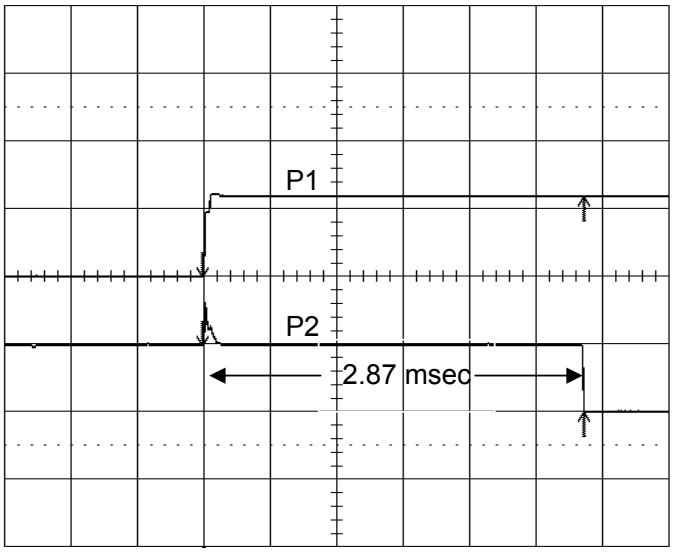

Fig. 12. Measured response time.

4. Frequency agile slot dipole perturbed using PET

A. Design

The designed CPW fed slot dipole is shown in Fig. 13. It is etched on a 1.27 mm thick RT-Duroid substrate with a dielectric constant of 6.15. The width of the center conductor of the CPW is 1.524 mm and the gap is 0.254 mm for the line impedance of 50 Ω. The slot antenna has the overall length L of 30.02 mm and width W of 4.47 mm. In general, high input impedance values are observed for ideal half-wavelength slot dipoles, and one-wavelength slot dipoles ($L=\lambda_s$) are matched easily to 50 Ω feed line [49]. However, the input impedance depends on the slot width and substate characteristics. The optimized dipole has the approximate length of 0.7 λ_s in this design. λ_s is the slot line wavelength at 4.8 GHz. The return loss and pattern simulations for the antenna are

realized with the aid of the IE3D, a full-wave electromagnetic simulator based on the method of moments [52].

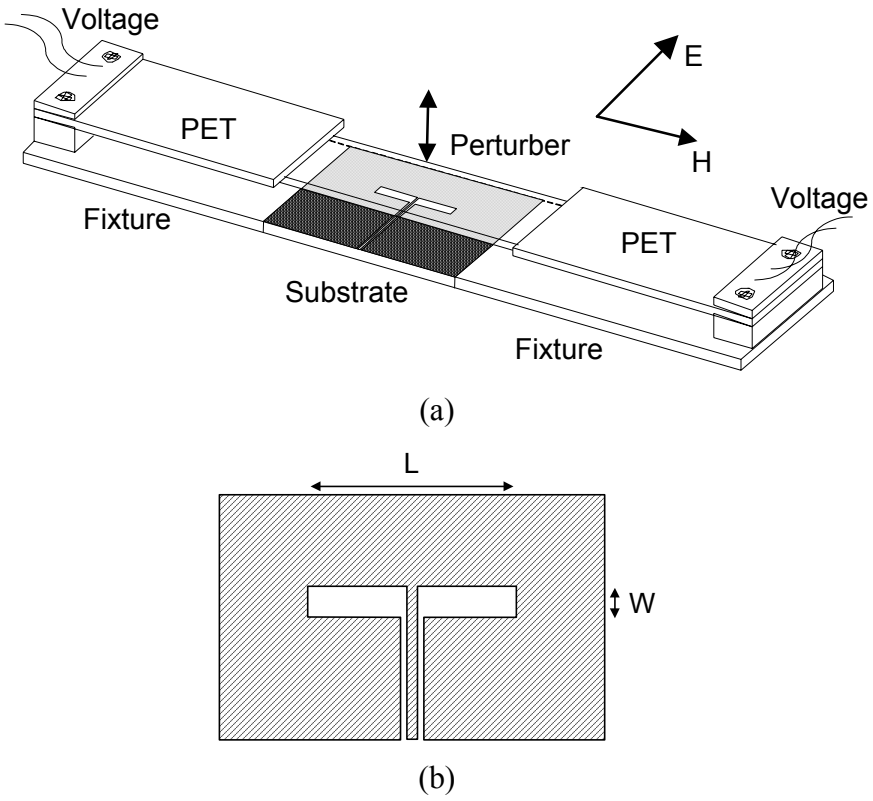

Fig. 13. CPW-fed slot dipole controlled by PET; (a) overall configuration, (b) CPW-fed slot dipole.

A PET-controlled dielectric perturber is used to change the effective dielectric constant of the printed slot dipole. The dielectric perturber has the thickness of 1.27 mm and a dielectric constant of 6.15. The PET is positioned at the endfire direction in the *H*-plane to reduce the interference on radiation pattern. The perturber is moved up and down parallel to the substrate. The air gap between the substrate and dielectric perturber

is varied using a piezoelectric plate deflected by an external voltage.

B. Measurements

A maximum external voltage of 60 V is used to perturb the substrate, and the resonant frequency of the dipole is changed from 4.65 to 4.35 GHz making the resonant frequency tuning range of 300 MHz as shown in Fig. 14. Fig. 15 shows the radiation patterns of the cases with maximum perturbation and without perturbation. The patterns are maintained similar at both cases with a figure eight shape. Although an ideal slot dipole radiates omni-directionally in the *E*-plane, the measured pattern gives some amplitude variations due to the finite ground plane and the attached port. The measured cross-polarization levels in both planes are maintained less than 20 dB.

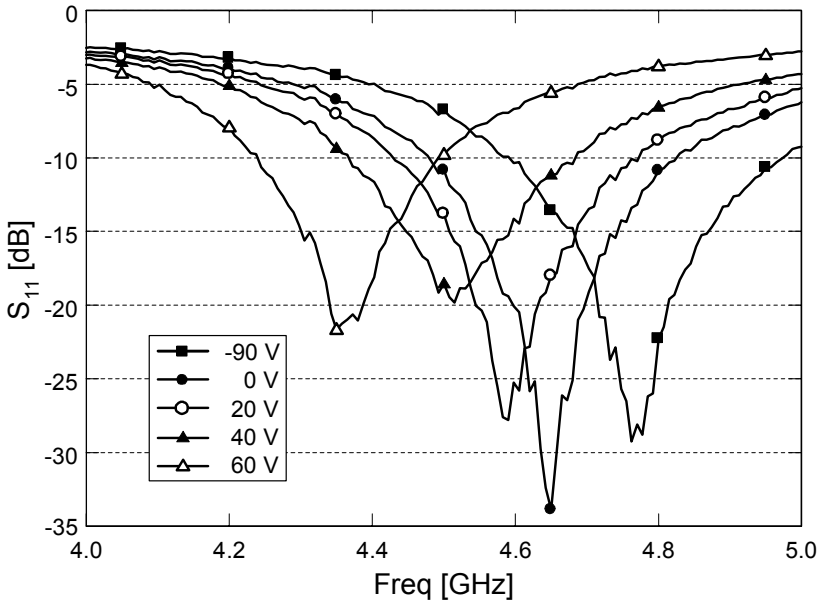

Fig. 14. Measured resonant frequency variation of the slot dipole tuned by PET.

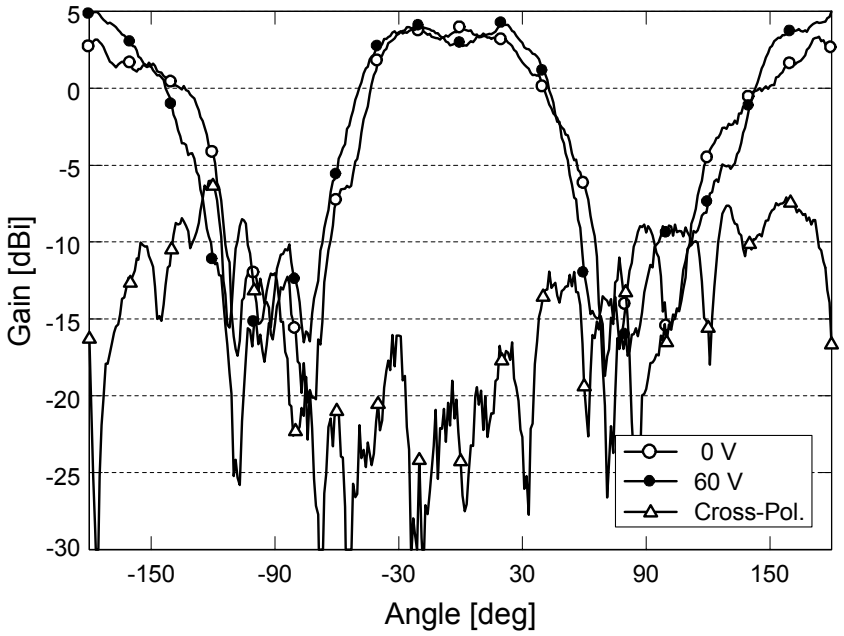

(a)

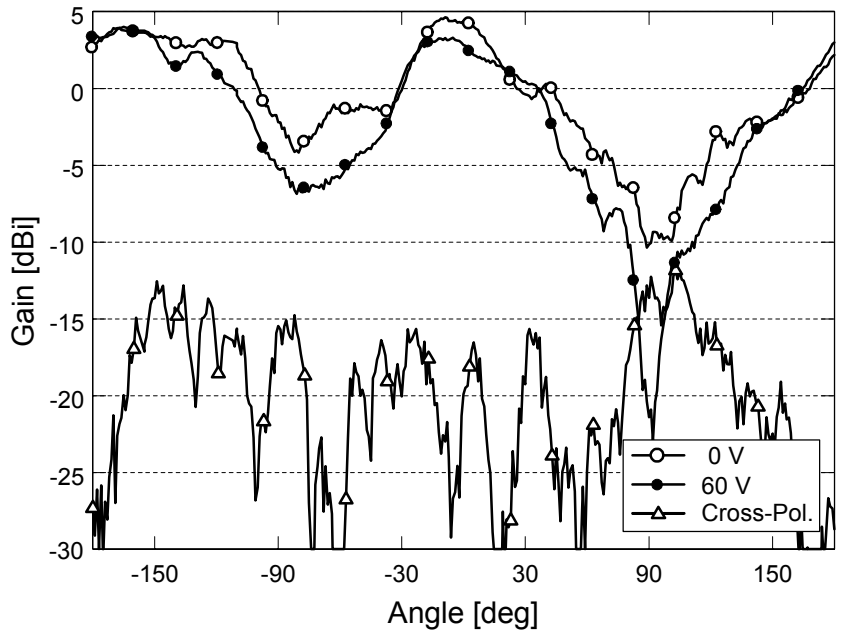

(b)

Fig. 15. Measured radiation patterns at zero and maximum perturbation; (a) *H*-plane patterns, (b) *E*-plane patterns.

5. Conclusions

Several microwave devices using piezoelectric transducer (PET) have been introduced in this chapter. A PET-controlled phase shifter using dielectric perturbation on CPW has been realized and compared with that using microstrip line. The simulated results agreed very well with the measured data. The phase shift of CPW is 50 % larger than that of microstrip, and the insertion loss is less than 1 dB.

The application of a PET-controlled phase shifter as a BPSK or QPSK modulator has been demonstrated at 15 GHz. The QPSK modulator using PETs gives the advantages of low loss, high power handling capability, and small power consumption. This technique can be applied to any frequency range with simple tuning process. However, the data rate is limited by the response time of PET.

As an application using controllability of PET, a novel PET-controlled frequency tunable CPW-fed slot dipole has been demonstrated. The resonant frequency of the slot dipole is tuned over 300 MHz from 4.65 to 4.35 GHz using an external voltage of 60 V to deflect the PET. The radiation patterns are similar with or without the perturbation.

CHAPTER III*

DUAL BEAM PHASED ARRAY AND MONOPULSE ANTENNA ARRAY USING BI-DIRECTIONALLY-FED MICROSTRIP PATCH ARRAY

1. Introduction

Microstrip patch antennas have been used widely in antenna designs because of its conformal and low-profile characteristics. Feed networks such as the series feeds, the corporate feeds, the electromagnetic coupled feeds, etc. have been used for array design. Multi-point feed is also used to achieve circular polarization or cross-polarization suppression in a single antenna, or to generate different polarized multiple beams in antenna arrays [17, 53]. However, little has been reported for using multi-point feeds to achieve multiple beams of the same polarization.

Monopulse, also called a simultaneous lobe comparison, has been developed as a solution to overcome the erroneous angle indication or the slow searching speed of the lobe switching and the conical scan of a classical radar system [54]. Monopulse techniques compare information received simultaneously by the sum (Σ) and difference

---

(Δ) channels of the target tracking receiver in an interference canceller or a radar system. Two common methods are to excite appropriate modes within a single feed horn and to use external combining networks on antenna arrays [55]. Sum/difference patterns using a slot line antenna and a low noise amplifier on a dual-feed Yagi antenna were recently reported [56, 57].

Phased array, which can steer a beam to the desired direction, is an important element for multi-point communication, satellite communication, and radar system. It has been designed with the diverse characteristics of a switched or a simultaneous, or a single or multiple beams, with same or different polarization. Same polarized multiple beam array is especially useful in tracking multiple and/or moving targets, or in reducing the scanning time. A conventional beam-forming network consists of a large number of transmission lines and phase shifters, the cost of which is about half of that of the whole system, making the system very expensive. A new low-cost and low-loss multi-line phase shifter and a phased array system were presented recently using a piezoelectric transducer (PET) [1, 58].

This research proposes a low-cost and simple-structured bi-directionally-fed microstrip patch array to achieve a sum/difference pattern and a same polarized dual beams. The total radiation pattern is the sum of fields radiated from the array by both feedings. As the bi-directionally-fed array is symmetrical in configuration, the matching network must be designed with consideration of array symmetry. A monopulse antenna can be designed easily by adjusting the input phases of both sides of the bi-directionally-fed microstrip array. The sum/difference pattern with excellent front-to-back ratio and

low cross-polarization levels is achieved from the in-phase and out-of-phase signals made by a hybrid coupler on both sides of the bi-directionally-fed microstrip array. A dual beam phased array system is also developed. Two beams of the same polarization are obtained by feeding both sides of the planar microstrip patch array, and these beams have a beam squint determined by the length of inter-connection line between the patch elements. Two PETs are used to form the phase shifters for a series-fed 4×8 microstrip patch antenna phased array.

2. Bi-directional feeding

The sum/difference pattern is synthesized using two squinted beams achieved from a bi-directionally-fed microstrip patch array. As shown in Fig. 16, a series-fed microstrip patch array consists of rectangular patch elements inter-connected by a high impedance line (100 Ω) [59]. The inter-connecting line length D introduces a progressive phase shift ϕ that makes a beam squint in the E-plane. The beam squint angle θ_o in the E-plane is determined by the progressive phase shift ϕ and is given by

$$\theta_o = \sin^{-1}\left(\frac{\phi}{k_o d}\right) \tag{2}$$

where k_o is the propagation constant in free space, and d is the distance between two neighboring antenna elements.

The input impedance is calculated from the $ABCD$ matrix of the 1×8 array calculated using IE3D, a full-wave electromagnetic simulator based on the method of moments [52, 60]. The matching circuit could be consisted of a tuning stub to

compensate for the imaginary part of the impedance of the array and a quarter-wave transformer to match the real part to 50 Ω lines.

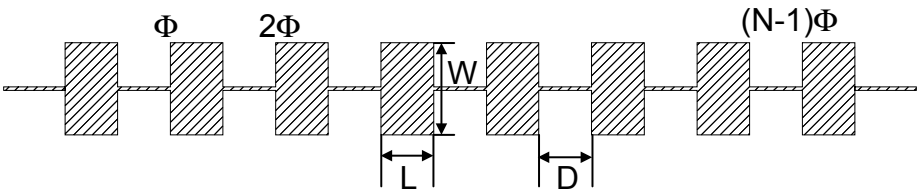

Fig. 16. Bi-directionally-fed microstrip patch array.

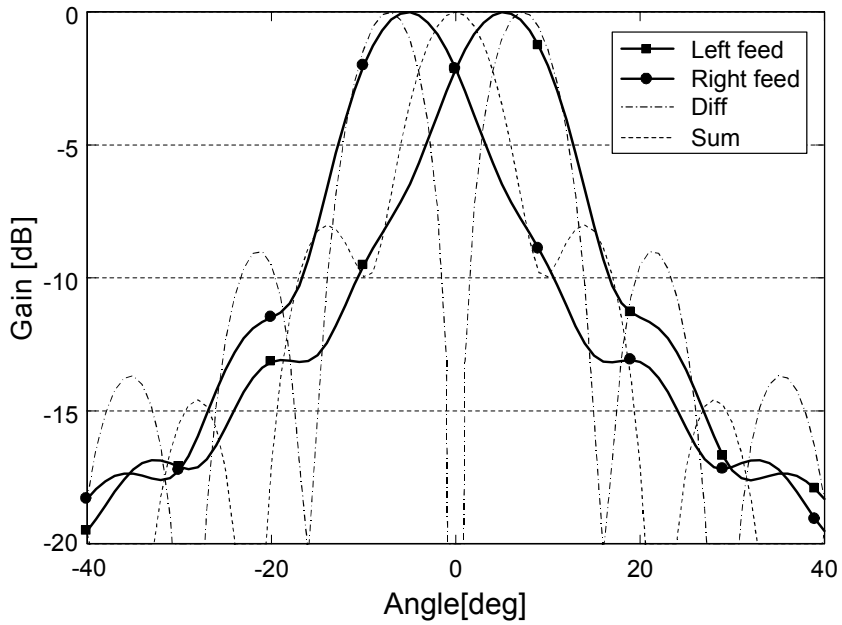

Fig. 17. Simulated *E*-plane pattern.

Since the radiation by the patch array from each feeding has the same polarization, the total radiation pattern is the sum of patterns made from each feed. The

sum/difference pattern is realized by adjusting the input phases of the bi-directionally-fed array. Fig. 17 shows the simulated patterns from each feeding and the sum/difference patterns in the *E*-plane for the 1×8 array with a beam squint of 5°.

3. Dual beam phased array

A. Design of the antenna array and phase shifter

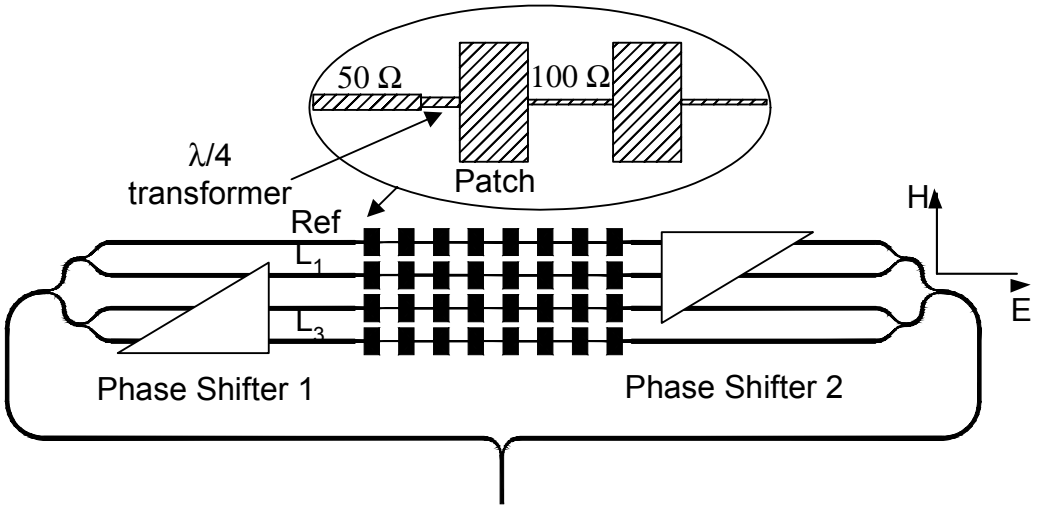

Fig. 18. Dual beam microstrip patch array.

The overall configuration for a dual beam phased array is shown in Fig. 18. It consists of a 2-way power divider, two 4-way power dividers, two phase shifters using piezoelectric transducers (PETs), and a 4×8 microstrip patch array. A binomial multisection impedance matching transformer is used to obtain the lowest possible return loss in the design of the power dividers, since this transformer has the maximally flat characteristics in the passband [60]. The designed power divider and the

characteristic impedances for line sections are shown in Fig. 19.

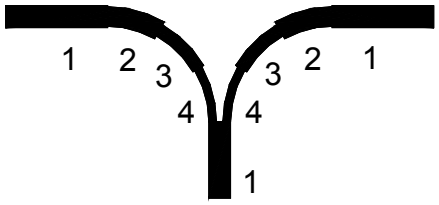

No	Characteristic Impedance [Ω]
1	50
2	54.535
3	70.71
4	91.685

Fig. 19. Power divider using binomial multisection matching transformer.

The dielectric constant and thickness are 2.2 and 0.254 mm for the substrate, and are 6.15 and 1.27 mm for the perturber, respectively. The operating frequency is 30 GHz. As shown in Fig. 20, the dielectric perturber attached to the PET is deflected by an external voltage. This voltage causes the air gap between the microstrip line and perturber to change. Because the phase shift is proportional to the coverage length of the perturber using a triangular shape, the perturber's lengths over each microstrip lines are designed to be 15, 30, and 45 mm. The differential phase shift $\Delta\phi$ caused by the perturbation is calculated as

$$\Delta\phi = L_p \cdot \frac{2\pi}{\lambda_o}\left(\sqrt{\varepsilon_{eff}(f)} - \sqrt{\varepsilon'_{eff}(f)}\right) \tag{3}$$

where L_p is the length of perturber over the microstrip line, λ_o is the wavelength in free space, and $\varepsilon_{eff}(f)$ and $\varepsilon'_{eff}(f)$ are the effective relative permittivities of the unperturbed

and perturbed microstrip line, respectively [1].

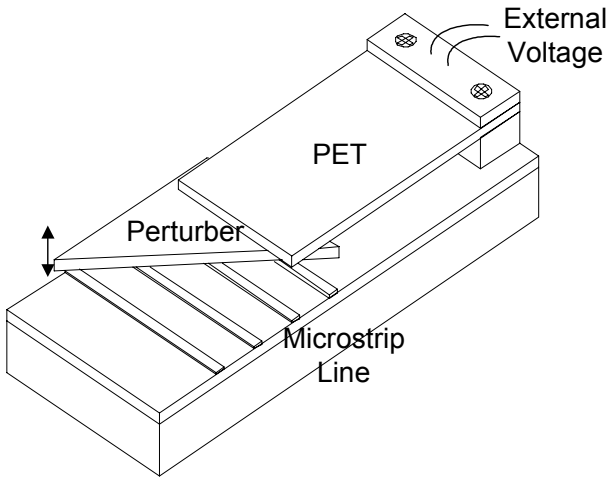

Fig. 20. PET-controlled phase shifter.

Each series-fed microstrip array is designed for a return loss of better than 10 dB. Since less than 10 % of the input power is transmitted to the input line on the other side, this array can be considered as a traveling wave array. The high impedance lines (100 Ω) are used as inter-connection lines for the series patch elements [59].

If the inter-element electrical length between the patch elements in a series traveling wave array is one wavelength, it presents a large impedance mismatch at the input port [61]. Thus, the array is designed to have a beam squint at 7° in the *E*-plane for good impedance matching. The inter-element distances in the *E* and *H*-plane are $0.67\lambda_o$ and $0.69\lambda_o$. Two inputs to 4-way dividers are maintained in-phase to achieve good antenna patterns. Two independent beams are obtained by feeding both sides. The two beams are *E*-plane polarized and steered independently in the *H*-plane.

B. Measurements

The input return loss shown in Fig. 21 is measured using an Agilent 8510C network analyzer, and is 14 dB at 30 GHz. Fig. 22 shows the measured phase shifts in each microstrip lines when the lines are perturbed by a PET with different applied voltages. A differential phase shift (in L_1 of Fig. 18) of 80° is obtained in the perturbed microstrip line with the length of 15 mm at the applied voltage of 50 V.

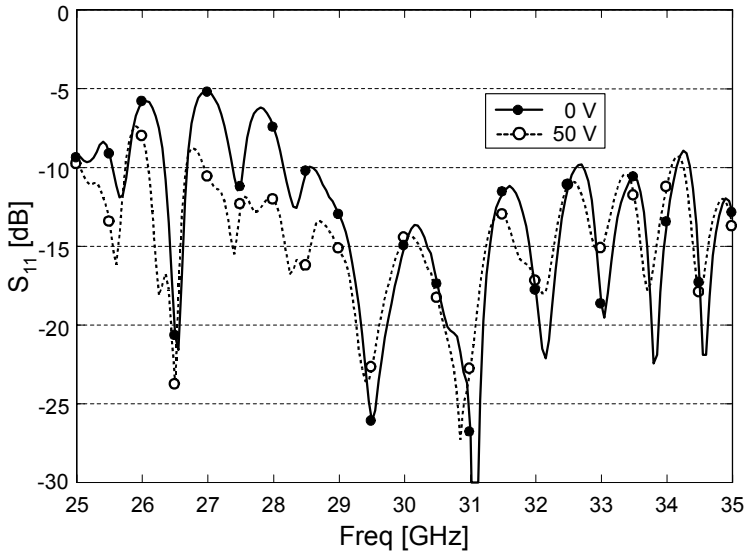

Fig. 21. Return loss of the microstrip patch array.

Fig. 23 shows the *E*- and *H*-plane radiation patterns measured in an anechoic chamber for the array without perturbation. The two beams have a beam squint at ±7° in the *E*-plane, and are at the broadside in the *H*-plane. The measured antenna gain including all losses is 13 dBi. The measured antenna patterns agree well with the simulation results carried out by the electromagnetic simulator IE3D.

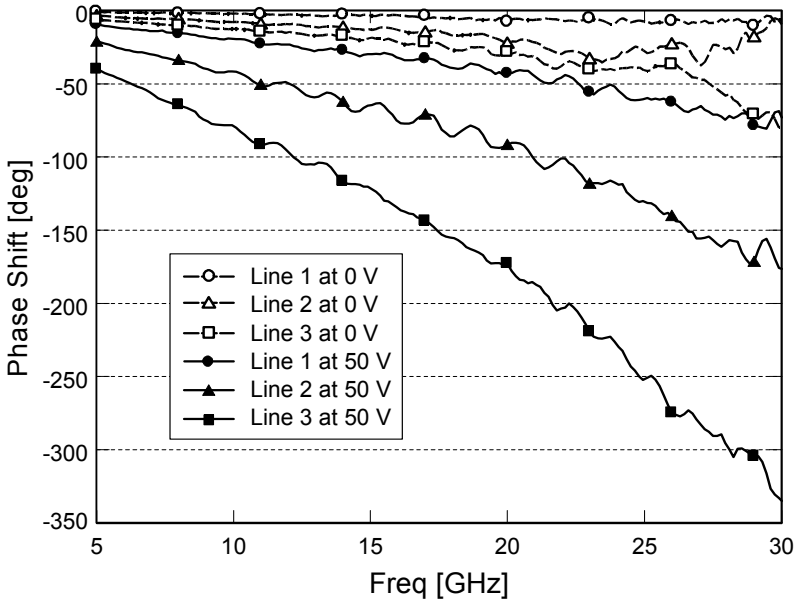

Fig. 22. Phase shift on microstrip lines controlled by PET

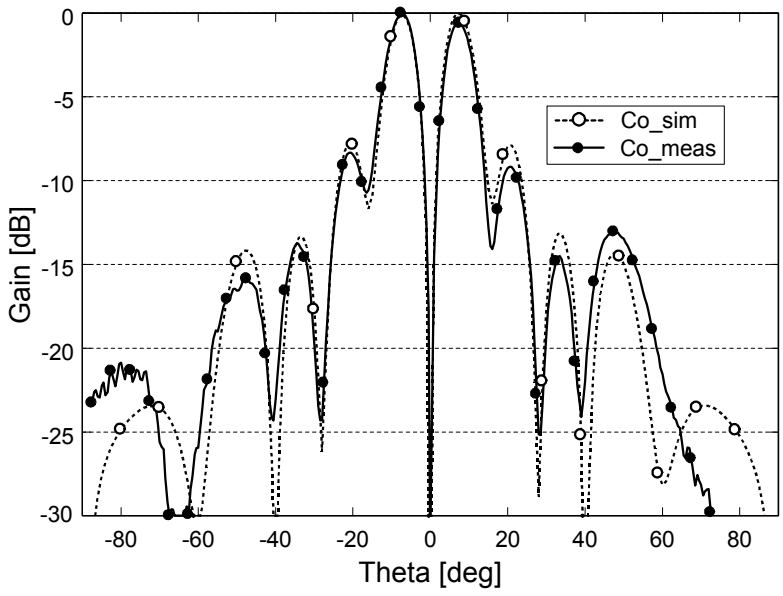

(a)

Fig. 23. *E*- and *H*-plane radiation patterns without perturbation; (a) *E*-plane, (b) *H*-plane.

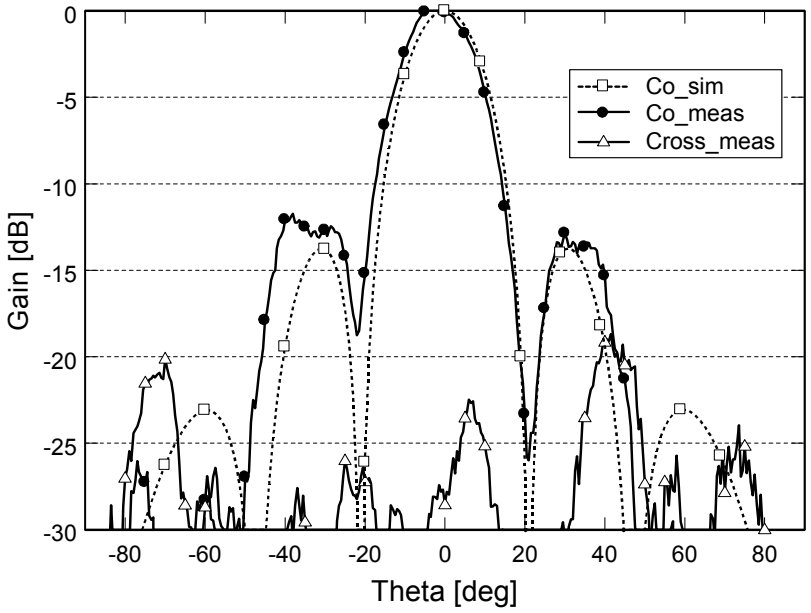

(b)

Fig. 23. Continued.

One PET is used for beam steering to steer one beam at a time during measurements. The maximum beam steering angle of each beam is 20° in the *H*-plane, when an applied voltage is changed from 0 to 50 V as shown in Fig. 24 (a). The beam is steered at 7° with 0 V. This means that the microstrip line is unintentionally perturbed slightly without an external voltage, and it can be solved by adjusting the initial gap between the microstrip line and perturber. The slightly widened beamwidth and reduced gain is measured at 50V due to the imperfect progressive phase shift. Fig. 24 (b) shows the other beam pattern in the *H*-plane that is not affected by the perturber. The beam is only moved slightly when the applied voltage is changed from 0 V to 50 V.

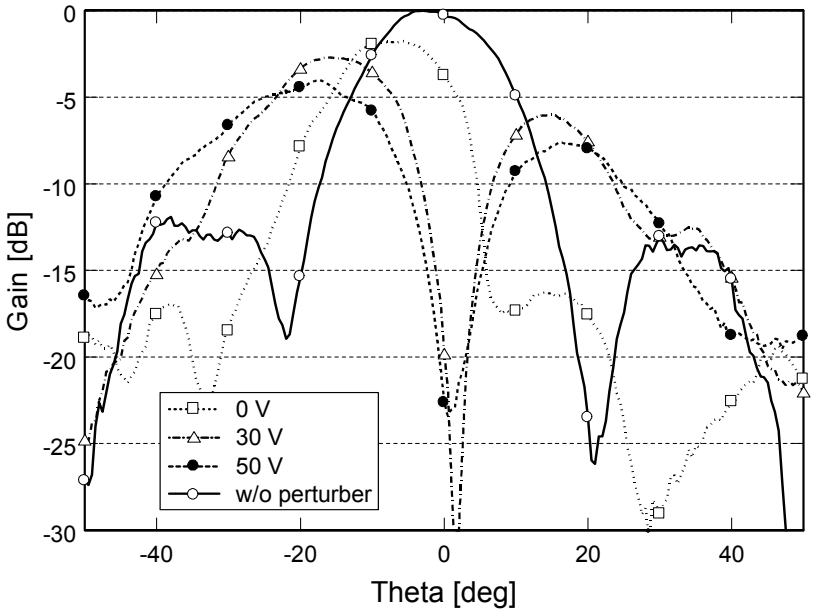

(a)

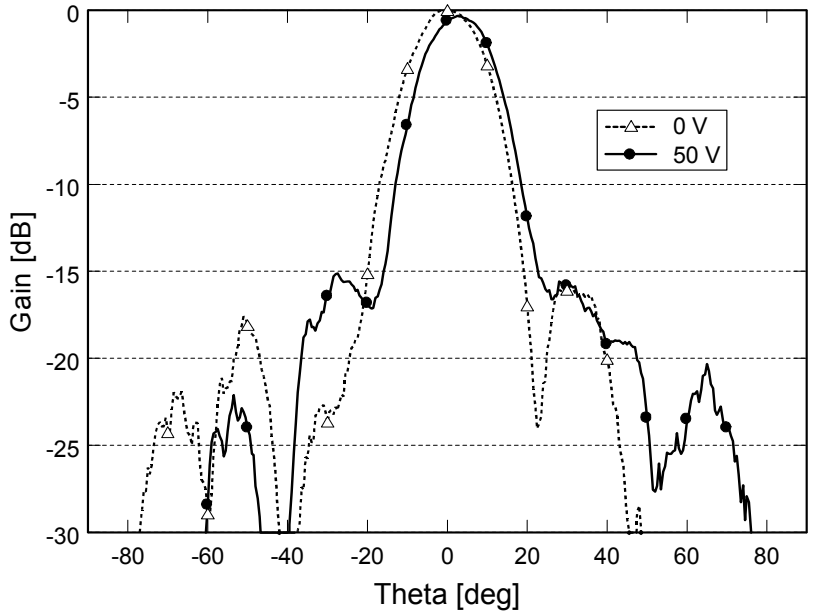

(b)

Fig. 24. *H*-plane radiation patterns with perturbation; (a) the steered beam by PET phase shifter, (b) the other broadside beam.

4. Monopulse antenna array

A. Design

A sum/difference pattern is synthesized using two squinted beams achieved from a bi-directionally-fed microstrip patch array. The input impedance is calculated from the *ABCD* matrix of the 1×8 array calculated using IE3D, a full-wave electromagnetic simulator based on the method of moments. The matching circuit consists of a tuning stub to compensate for the imaginary part of the impedance of the array and a quarter-wave transformer to match the real part to 50 Ω lines. Fig. 25 shows the monopulse patch antenna designed for sum/difference pattern. The length L_1 of the designed open stub with the characteristic impedance of 100 Ω is 4.62 mm, and the characteristic impedance and length L_2 of the quarter-wave transformer is 70.7 Ω and 1.84 mm.

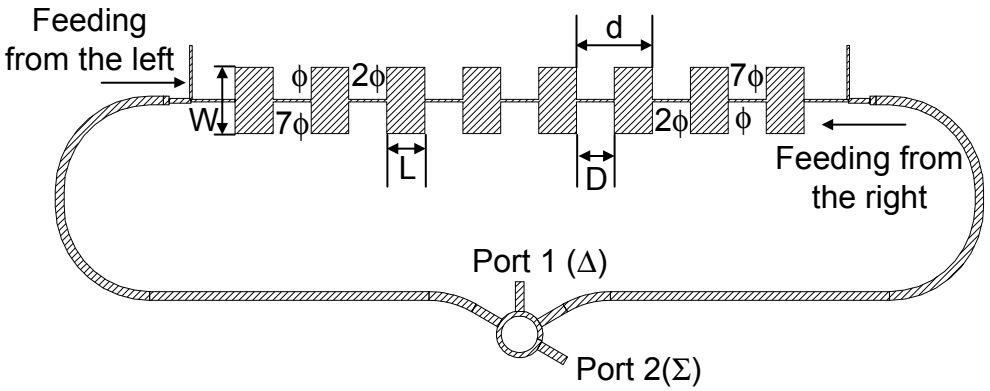

Fig. 25. Monopulse patch antenna for sum/difference pattern.

Since the feeding from the right and left side of the array has an inherent 180°

phase difference, inputs with 180° out of phase make a sum pattern at the broadside, and those with same phases give the difference pattern. A hybrid ring coupler is used to make in-phase and out-of-phase signals on both sides of the array, and to realize the sum and difference patterns. A simultaneous sum/difference pattern is realized by feeding port 1 and 2 of the coupler.

B. Measurements

The radiation pattern from each feeding has a beam squint at 5°, which is determined by the length of an inter-connection line. The inter-element distance is 0.64 λ_o, causing a beam squint at 5°. The test array is fabricated on an RT/Duroid substrate with a thickness of 0.254 mm and a dielectric constant of 2.2. The design frequency is 30 GHz. The patch element has a width *W* of 5.61 mm and a length *L* of 3.2 mm.

The measured return losses at both ports are maintained better than 10 dB, as shown in Fig. 26. Fig. 27 (a) and (b) shows the measured patterns in the *E*- and *H*-plane. The gain of the sum pattern is 13 dBi and the null depth (gain difference between the sum and difference patterns) at the broadside is more than 30 dB. The cross-polarization level is less than -25 dB at the broadside.

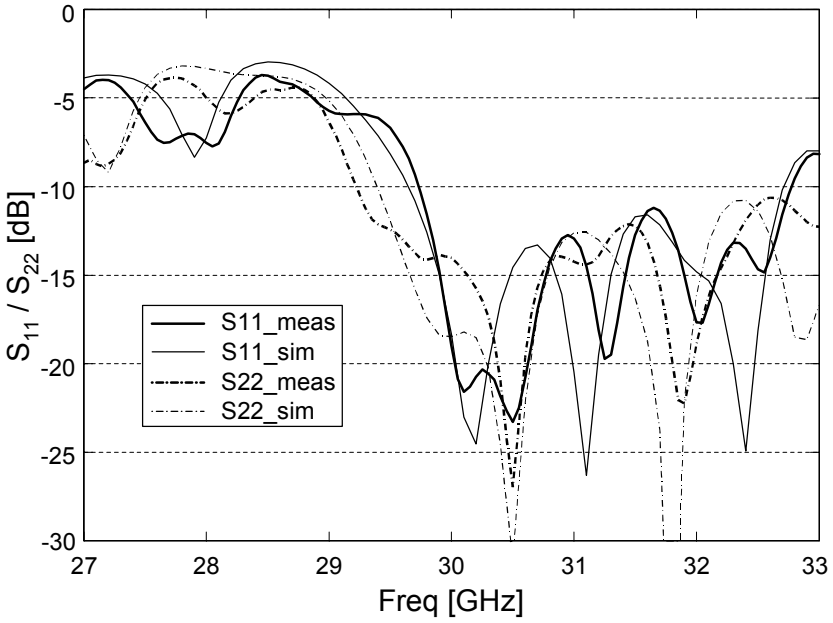

Fig. 26. Return loss of the monopulse antenna at the sum/difference port.

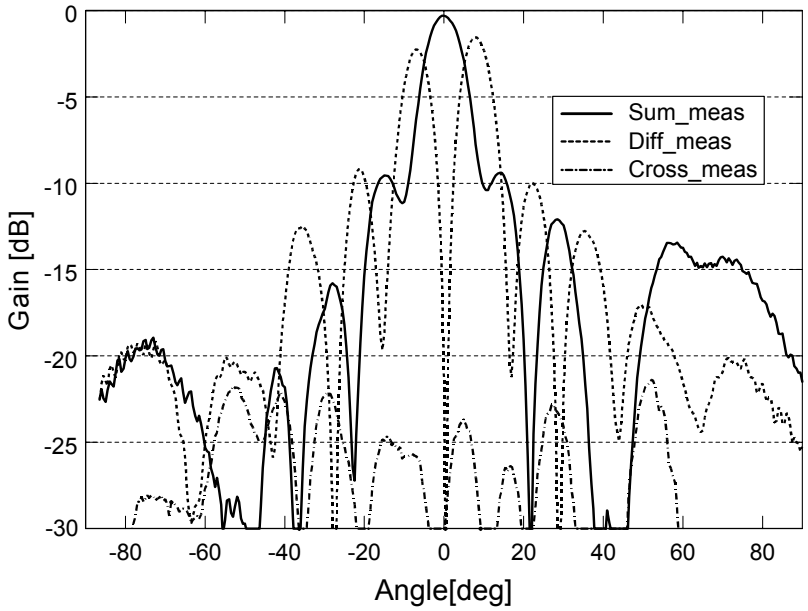

(a)

Fig. 27. Radiation patterns of the monopulse antenna; (a) measured *E*-plane patterns, (b) measured *H*-plane patterns.

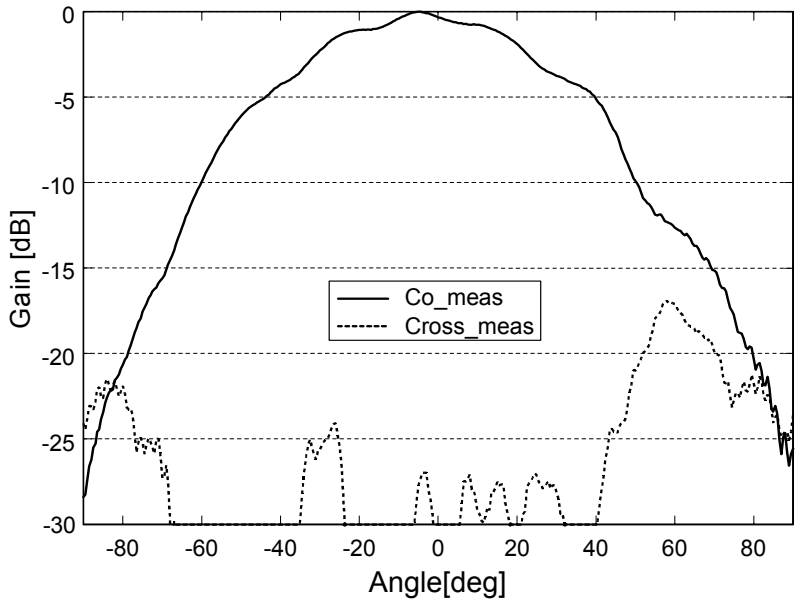

(b)

Fig. 27. Continued.

5. Conclusions

A novel multi-point feeding technique to achieve multiple beams of the same polarization has been introduced, and the bi-directionally-fed microstrip array was applied to fabricate a dual beam phased array and to synthesize sum/difference patterns. A dual beam phased array using bi-directional feeding to a common 4×8 patch array was designed and tested. Signals split by the T-junction power dividers are fed to both sides of a 4×8 microstrip patch array. Both steerable beams have the same polarization and are controlled independently by PET phase shifters. The antenna gain is 13 dBi, and the maximum beam steering angle is 20° when the external voltage is applied from 0 to 50 V. A simple monopulse array for a sum/difference pattern has been realized using a

symmetrical bi-directionally-fed array and a hybrid ring coupler feed. The gain of the sum pattern and the null depth of the difference pattern at the broadside are 13 dBi and more than 30 dB, respectively.

CHAPTER IV*

MULTIPLE BEAM PHASED ARRAY USING MICROSTRIP ROTMAN LENS

1. Introduction

Modern communication systems often demand wide bandwidth, multiple beams, and beam steering capability. Phased array antennas have proven useful for satellite communication systems and radar. Multiple beam antennas which use beam switching offer a less expensive and compact alternative to traditional phased arrays requiring more complex fabrication. A multiple beam antenna has a capability to form many beams using multiple input ports in different directions from the same aperture. It differs from an electronically steered array because each port corresponds to a different beam.

Several lens-based beamformers such as Ruze, Rotman and R-KR, and circuit-based beamformers such as Blass and Butler matrix are commonly used in multiple beam antennas [16]. Dielectric lenses such as a Luneberg lens can also be used, though are expensive to manufacture at millimeter-wave frequencies [2, 3]. With circuit-based beamformers, it is known that the hardware complexity grows exponentially with increasing array size [4]. Consequently, lens based beamformers are attractive in large

---

array design.

Ruze reported the design of a lens using two focal points. Shelton then greatly simplified the design equations with a symmetrical lens contour, however its design options are constrained [5]. Katagi *et al.* improved the Rotman lens to allow different values in focal angle and scan angle [6, 62]. Most papers on lens feeds have been based on the Rotman lens using three perfect focal points.

A Rotman lens with the capability of wide-band and wide-angle multiple beam feed to a linear array is an extremely useful beam forming network due to its frequency invariant beam pointing [7, 8]. Recently, several microstrip and stripline Rotman lenses have been reported [9-13]. Planar microstrip lenses on a dielectric substrate reduce circuit size and manufacturing complexity through its simple etching process.

In phased array systems, phase shifters are critical components due to their cost and complexity. As an alternative to phase shifters, a McGrath lens controlling the amplitude of the dual spatial feeds has been introduced to steer the multiple beams [63], but did not demonstrate sufficient steering ability. A multi-line phase shifter controlled by a piezoelectric transducer (PET), published recently, enables the design of a phased array with low-cost, low-loss, and easy fabrication [1, 58].

In this research, a simple and low-cost multiple beam phased array is designed using a microstrip Rotman lens and PET-controlled phase shifter. A microstrip Rotman lens with five beam ports and nine array ports is used as a feed for a multiple beam antenna to make the scan angle of 0°, ±15°, and ±30° at *Ka*-band. The tapered ports of the Rotman lens are matched using a quarterwave transformer, and dummy loads

terminated using resistive absorbers are used to reduce the wave reflections at the lens walls. Using two PET-controlled phase shifters, the five beams are steered at ±8°, completely covering ±38° from the broadside. The phase shifter is designed to steer the beams in 8° which is needed to cover between the adjacent beams.

2. Design of microstrip Rotman lens

A. Configuration of the designed Rotman lens

Fig. 28 shows the designed microstrip Rotman lens with resistive pads as dummy loads. The operating frequency is 30 GHz. Signals are coupled into five beam ports resulting in five beams radiated by nine patch antennas connected to nine array ports. Five beam ports are coupled to the lens at the angles φ = 0°, ±15°, and ±30°. Nine microstrip patches are used in an equally spaced linear array. Dummy loads are used to reduce the reflections by the walls of the lens.

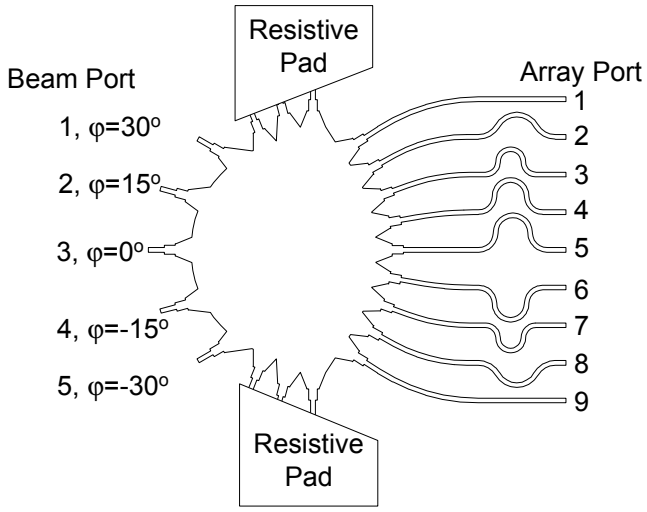

Fig. 28. The designed microstrip Rotman lens.

B. Design of lens contour

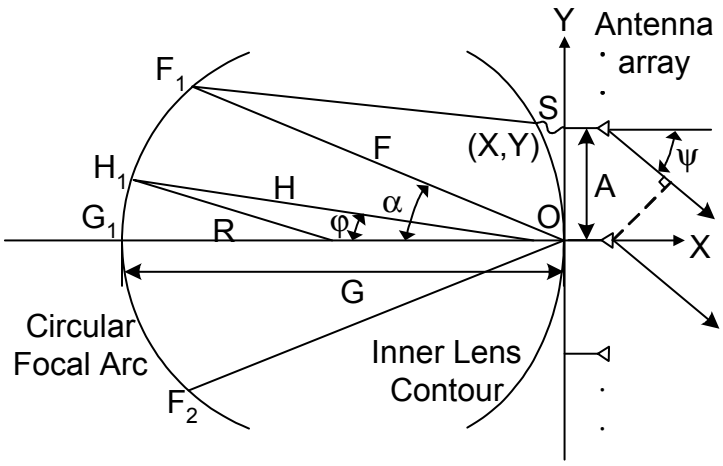

Fig. 29. Microstrip Rotman lens parameters.

The design parameters of the lens are shown in Fig. 29. The basic design parameters are the focal angle α and the ratio of the on-axis focal length to the off-axis focal length G/F. H_1 is a point on the circular focal arc with an angle φ from the axis. R is the radius of the circular focal arc. In this design, the focal angles to the axis of rays radiated from the three focal points F_1, G_1, and F_2 are designed as 30°, 0°, and −30°, respectively. The scan angle ψ is the same as a focal angle. Since the off-axis focal points are located symmetrically about the center axis, the lens contours are also symmetrical.

To correctly focus the lens, the effects of the dielectric constant ε_r of the substrate and the effective dielectric constant ε_{eff} of the microstrip line should be considered in defining the design parameters. The related variables normalized to F are described as

$$x = \frac{X}{F},\ y = \frac{Y}{F},\ g = \frac{G}{F},\ \eta = \frac{A}{F},\ s = \frac{S}{F},\ a_O = \cos\alpha,\ b_O = \sin\alpha$$

where A is the distance between elements (array port 4 and 5 in Fig. 28) and S is the length of microstrip line at array ports. Then, the design equations can be derived for x, y, and s through the algebraic manipulation on the geometry of Fig. 29 as (Appendix A) [7, 9, 10]

$$y = \frac{\eta}{\sqrt{\varepsilon_r}}\left(1 - \frac{\sqrt{\varepsilon_{eff}}}{\sqrt{\varepsilon_r}}s\right), \tag{4}$$

$$x^2 + y^2 + 2a_O x = \frac{\varepsilon_{eff}}{\varepsilon_r}s^2 + b_O^2\frac{\eta^2}{\varepsilon_r} - 2\frac{\sqrt{\varepsilon_{eff}}}{\sqrt{\varepsilon_r}}s, \tag{5}$$

and

$$x^2 + y^2 + 2gx = \frac{\varepsilon_{eff}}{\varepsilon_r}s^2 - 2g\frac{\sqrt{\varepsilon_{eff}}}{\sqrt{\varepsilon_r}}s \tag{6}$$

where g , A, and F in this design are set to 1.1, 0.5 λ_O , and 2.7 λ_O , respectively. λ_O is the wavelength in free space. The normalized coordinates (x, y) for the inner lens contour and the length s for microstrip line are calculated at each array port.

Fig. 30 shows the lens contour drawn using the calculated x and y. Since the electrical length in the lens cavity is reduced by a factor of $1/\sqrt{\varepsilon_r}$, using a substrate with high dielectric constant reduces the physical size of the lens.

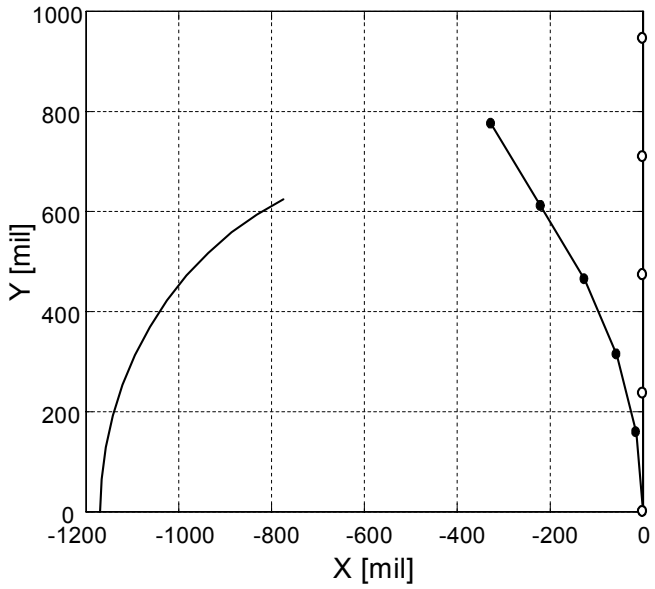

Fig. 30. Designed microstrip Rotman lens contour.

C. Calculation of the path length errors and array factor (Appendix B)

For wide-angle scanning the lens must focus well, not only at these three points, but also at all intermediate angles. As derived in [7, 10], the path length error of the lens is defined as the difference between the path length from a beam point H_1 to the origin O and the path length from H_1 to any other array port. These path lengths are traced from an arbitrary point on the focal arc through the lens and terminate normal to the emitted wavefront.

The path length error ΔL is expressed as

$$\Delta L = F\sqrt{\varepsilon_r}\,(h^2 + x^2 + y^2 + 2hx\cos\alpha - 2hy\sin\alpha)^{0.5} + \sqrt{\varepsilon_{eff}}\,s + \eta\sin\varphi - \sqrt{\varepsilon_r}\,h \qquad (7)$$

where h ($=H/F$) is the normalized distance from a point H_1 on the focal arc to the origin [7]. φ is the angle between central axis and an arbitrary point on the focal arc. The

calculated lens contour and phase aberrations is described extensively in Appendix B.

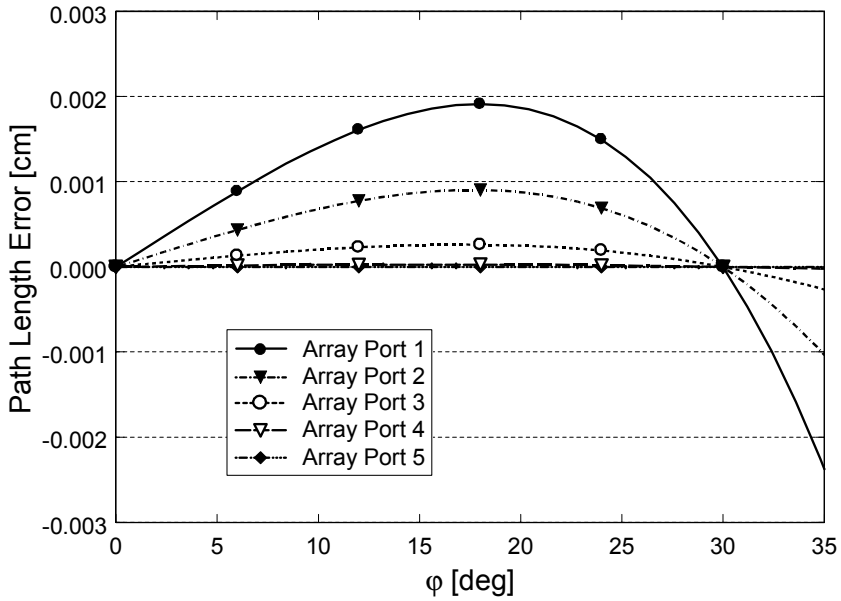

Fig. 31. Path length error in the design of a microstrip Rotman lens.

Fig. 31 shows the calculated path length errors at array ports as a function of arc angle φ. As the lens is designed to achieve perfect focal points at 0° and ±30°, the path length errors are zero resulting in an ideal beam when fed at the arc angles of 0° and ±30°. The path length error is calculated at five array ports considering the symmetry of lens.

The total radiation pattern (P_{total}) is equal to the product of the the pattern of single microstrip patch element (E_{single}) and the array factor (AF) of a nine-element array

$$P_{total}[dB] = 20 \times \log(E_{single} \times AF) \tag{8}$$

where E_{single} is approximately proportional to $\cos\theta$. In addition, AF is

$$AF = \sum_{n=1}^{9} a_n e^{j[(n-1)(k_o d \cos\theta)+\Phi_n]} \tag{9}$$

where k_o and d are the propagation constant in free space and the array spacing, respectively. a_n is assumed to be 1 for an equal amplitude distribution and Φ_n is the input phase shift at each array port. These phase shifts are calculated from the path lengths between the beam ports and array ports including the microstrip lines of electrical lengths S_n. Although an improved design rule may be used to reduce the path length errors [6], the amounts of the errors are negligible in most practical array designs.

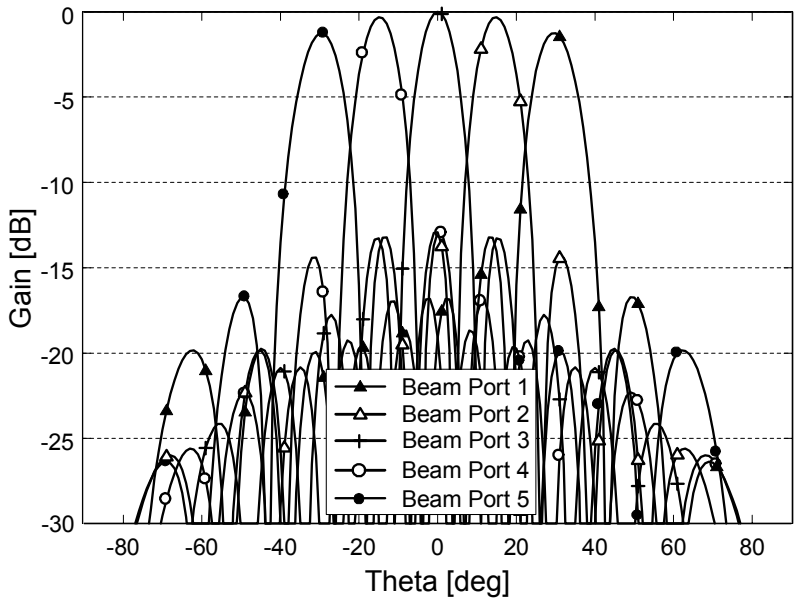

Fig. 32. Normalized radiation pattern calculated from the path length of the lens.

Fig. 32 shows the calculated *H*-plane radiation pattern as a function of angular

position θ using the path length which is determined from the lens contour of Fig. 30. The array factor shows an excellent pattern reaffirming that the path length errors are sufficiently small.

D. Matching network and dummy load

S-parameters are calculated using IE3D, a full-wave electromagnetic simulator using the method of moments. The *S*-parameters are then used to determine the input impedance including the effect of the tapered line at each port of the lens. The calculated input impedance is around 20 Ω with small reactance at the five beam ports and nine array ports. A quarterwave transformer is used to match each port to 50 Ω line. Although the lens has a wideband characteristic, the bandwidth of a microstrip Rotman lens is limited by the matching network of each port. It is possible to improve the bandwidth using a multi-section impedance transformer. Fig. 33 shows a wideband matching circuit using two three-step Chebyshev transformers. The lens design equations do not specify the shape of the sidewall that joins the circular focal arc and the inner lens contour. It is necessary to design the lens edge carefully, as this can affect the lens performance with the sidelobe level and insertion loss [14]. Dummy ports with matched loads are used on the unused ports to reduce the reflections at lens walls. Component dimensions of chip resistors for matched loads at *Ka*-band are very small (less than 0.5 mm) making fabrication difficult. So a magnetic absorber (ARC-DD-10214) manucfactured by ARC Technologies, Inc. is used as matched loads. The measured return loss of the dummy load terminated by the resistive absorber shows better than 10 dB at the operating frequency. This technique is effective for low dielectric substrate [15].

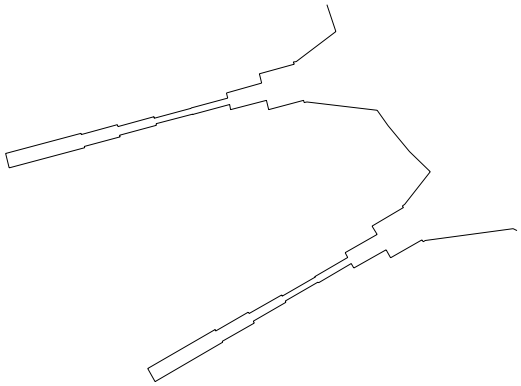

Fig. 33. Ports of the lens using three-step Chebyshev transformer for impedance matching.

E. Design of the microstrip array

Element spacing is critical as it controls the appearance of grating lobes. In general, for a maximum beam angle of θ_o from the broadside, the spacing d is kept below the value calculated by the following equation [64].

$$d = \frac{\lambda_o}{1 + |\sin \theta_o|}. \tag{10}$$

The spacing is designed as 0.6 λ_o, because it is limited by the width of the microstrip patch. Nine microstrip patches are used in an equally spaced linear array.

F. PET-controlled phase shifter and beam steering

Fig. 34 shows the fabricated PET-controlled phase shifter with nine microstrip lines used for beam steering. The dielectric perturber attached to a PET is deflected by an external voltage. This voltage causes the air gap between the microstrip line and perturber to change. Because the phase shift is proportional to the coverage length of the

perturber with a trapezoidal shape, the perturber's length over each microstrip line is designed to be 1 and 8 cm at line number 1 and 8, respectively, for progressive phase shift. Two PETs are used to move the perturber up/down parallel to the microstrip lines.

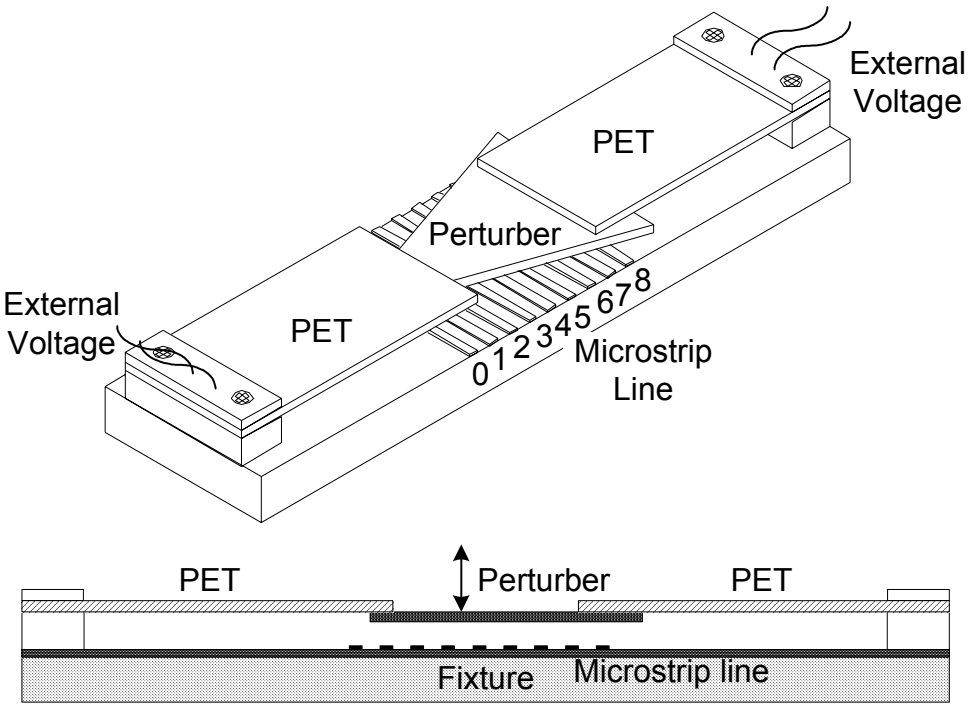

Fig. 34. PET-controlled phase shifter, the side view is also shown.

The differential phase shift $n\Delta\phi$ on the nth microstrip line caused by the perturbation is calculated as

$$n\Delta\phi = nL_1 \cdot \frac{2\pi}{\lambda_o}\left(\sqrt{\varepsilon_{eff}^{'}(f)} - \sqrt{\varepsilon_{eff}(f)}\right),\ n = 1, 2, ..., 8 \tag{11}$$

where L_1 is the length of perturber over microstrip line number 1, and $\varepsilon_{eff}^{'}(f)$ and $\varepsilon_{eff}(f)$ are the effective relative permittivities of the perturbed and unperturbed

microstrip line, respectively. The progressive phase shift between any two neighboring microstrip lines is $\Delta\phi$. The scanning angle θ_o of the phased array is given by the following equation.

$$\theta_o = \sin^{-1}\left(\frac{\Delta\phi}{k_o d}\right). \tag{12}$$

$\Delta\phi$ of 30° is designed to achieve the scanning angle of 8°. Although a higher permittivity of the perturber than that of the substrate increases the amount of phase shift, this degrades the performance of phase shifter by becoming very lossy at a high frequency range due to leaky wave mode generation [1]. An RT/Duroid 6002 with a dielectric constant of 2.94 close to that of the substrate and thickness of 1.524 mm is used as the dielectric perturber for the PET-controlled phase shifter. The perturber covers eight microstrip lines and the longest coverage on microstrip line has the length of 8 cm. The insertion loss at the perturbed line is generally small, as shown in [1].

3. Experiments

The substrate used for the Rotman lens array is an RT/Duroid 5880 with a dielectric constant of 2.2 and thickness of 0.254 mm. The measured return loss of the Rotman lens without phase shifters is better than 15 dB for all beam ports at the operating frequency, as shown in Fig. 35. The measured results include the effects of connectors and assembling errors.

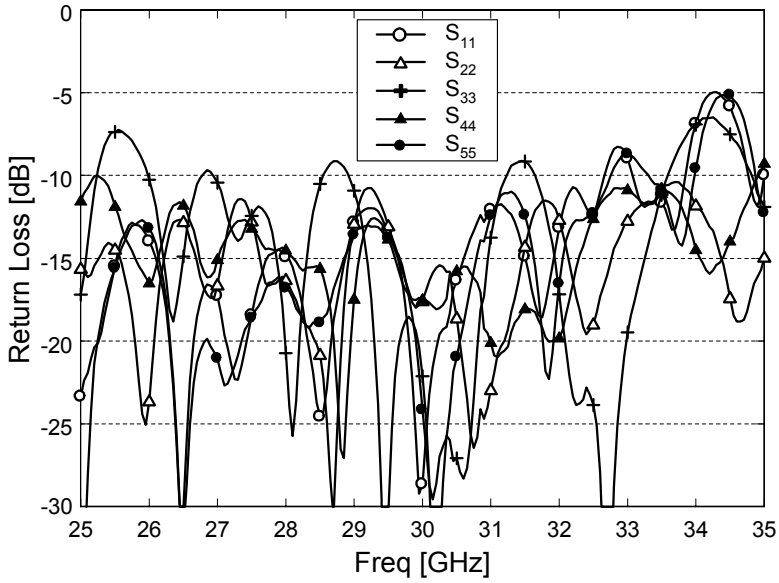

Fig. 35. Measured return loss at five beam ports of the microstrip Rotman lens.

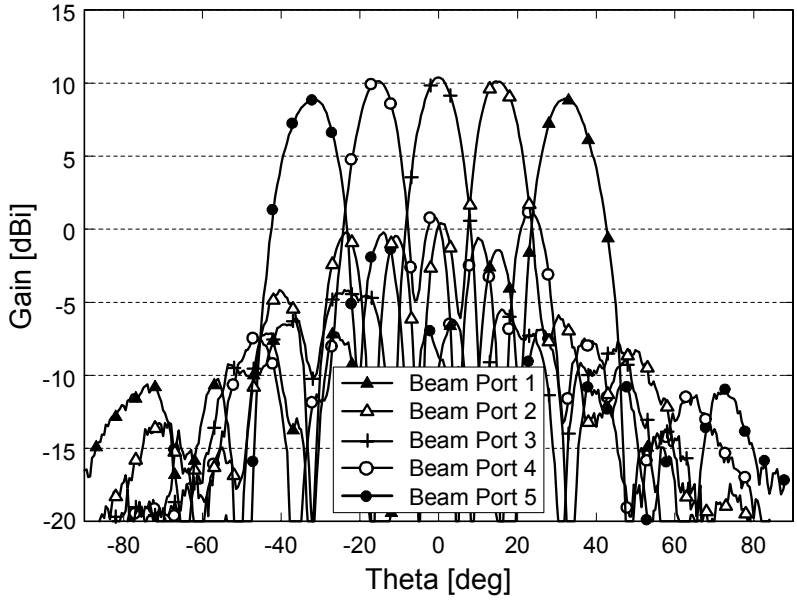

(a)

Fig. 36. Measured radiation patterns of a microstrip Rotman lens fed patch antenna array without PET-controlled phase shifter; (a) *H*-plane pattern, (b) *E*-plane pattern.

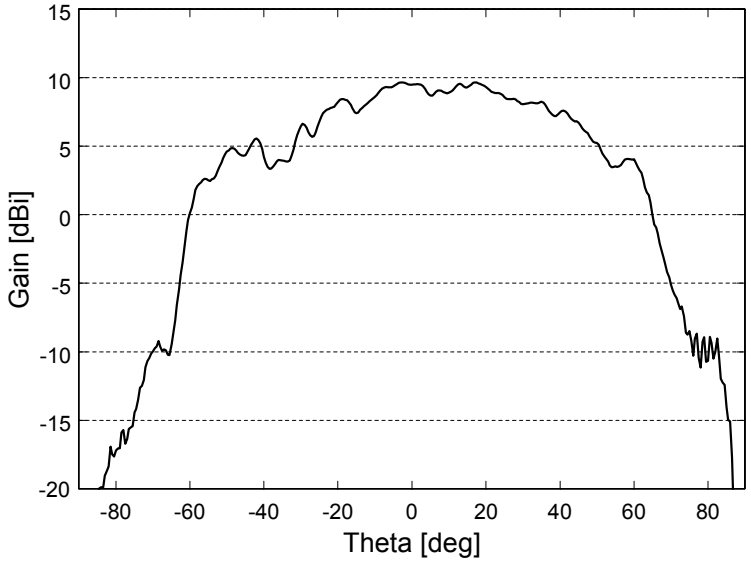

(b)

Fig. 36. Continued.

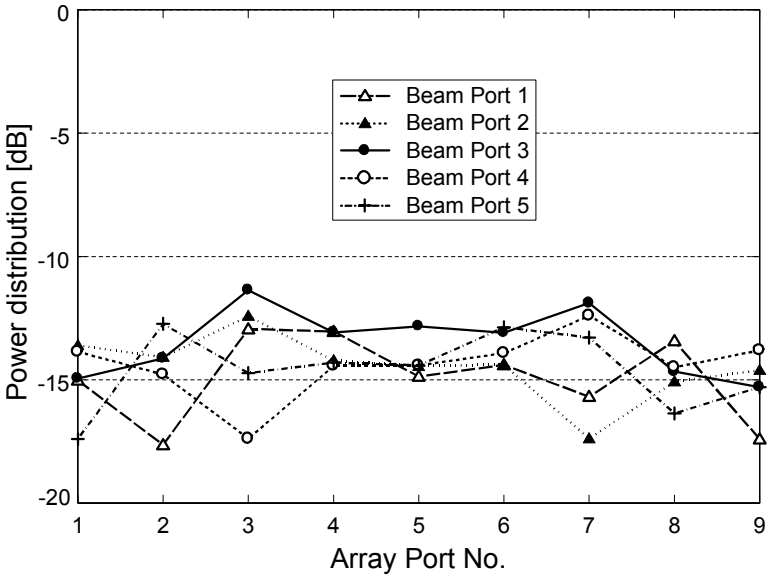

(a)

Fig. 37. Measured power distribution and differential phase shift of the microstrip Rotman lens; (a) power distribution at nine array ports fed by five beam ports, (b) differential phase shift at nine array ports compared with the phase at array port 1.

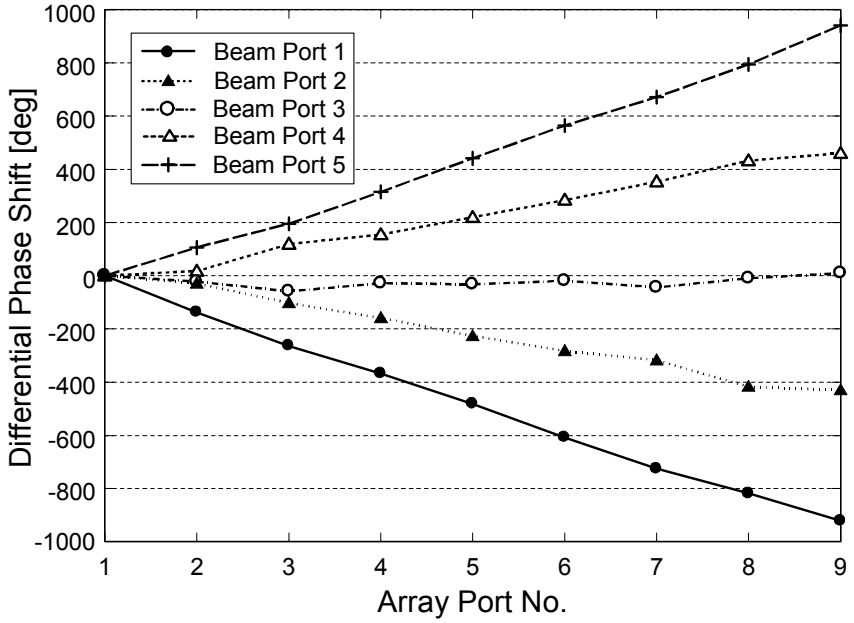

(b)

Fig. 37. Continued.

Fig. 36 shows the radiation patterns measured in the *H*- and *E*-plane without perturbation made by the phase shifter. The measured antenna gain is around 10 dBi including all losses by the lens and phase shifter, and the sidelobe level is less than −10 dB. However, the measured patterns show slightly higher sidelobe levels compared with the calculated ones due to the phase errors by the internal reflections in the open-circuited lens wall between the beam ports, and the spurious radiation due to the phase shifter and lens.

Fig. 37 (a) shows the power distribution of the Rotman lens at the array ports, and Fig. 37 (b) shows the differential phase shifts made at the array ports of the Rotman lens, compared with that of the array port 1. The power variation of ±3 dB seems to be partly

due to internal reflections in the open-circuited lens wall between the beam ports and the dummy loads. The tapered amplitude distributions could be achieved using additional matched ports between the beam ports. It can be further improved through the optimization in sidewall matched with dummy loads, lens port width, port angle, and other lens parameters such as focal arc [8, 14, 15]. However, the lens could become bigger than the proposed one. The differential phase shifts made from signals fed by five beam ports are almost progressive at nine array ports to make the beams radiate at 0°, ±15°, and ±30°.

The insertion loss of the lens is defined as

$$IL_n = 10 \times \log[\sum_{m=1}^{9} S_{mn}^2] \tag{13}$$

where m and n are array port number and beam port number, respectively. The insertion loss measured at each beam port of the lens varies between 3.7 to 5.1 dB, as indicated in Table 2. The loss includes ohmic and dielectric loss by the microstrip line and lens, and spill-over loss into dummy loads.

Table 2. Insertion loss of the microstrip Rotman lens

Beam Port No.	Insertion Loss [dB]
1	5.1
2	4.8
3	3.7
4	4.7
5	4.8

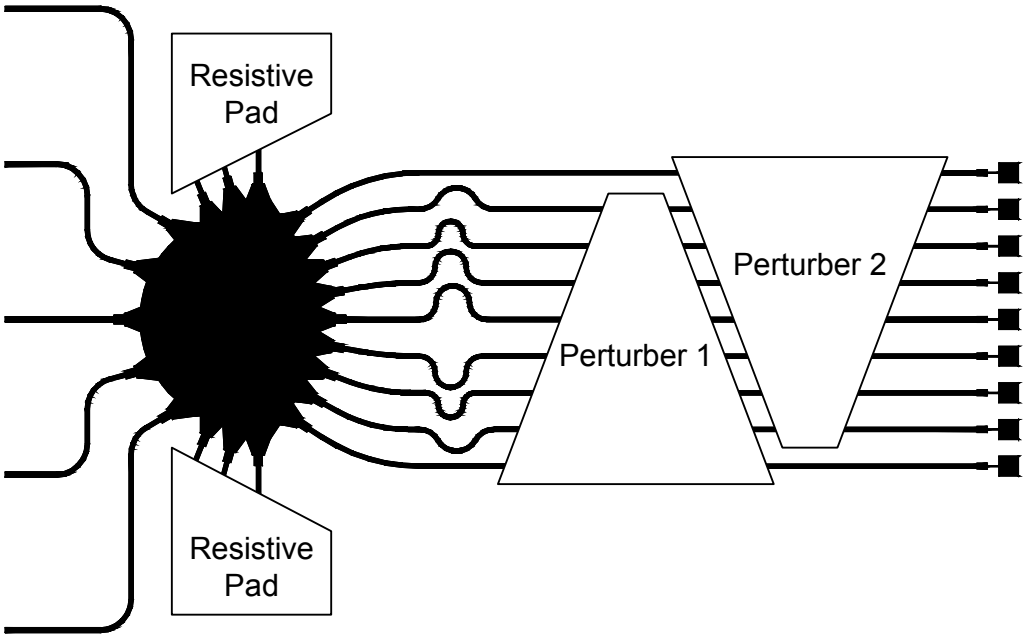

Fig. 38. Configuration of a PET-controlled multiple beam phased array using microstrip Rotman lens.

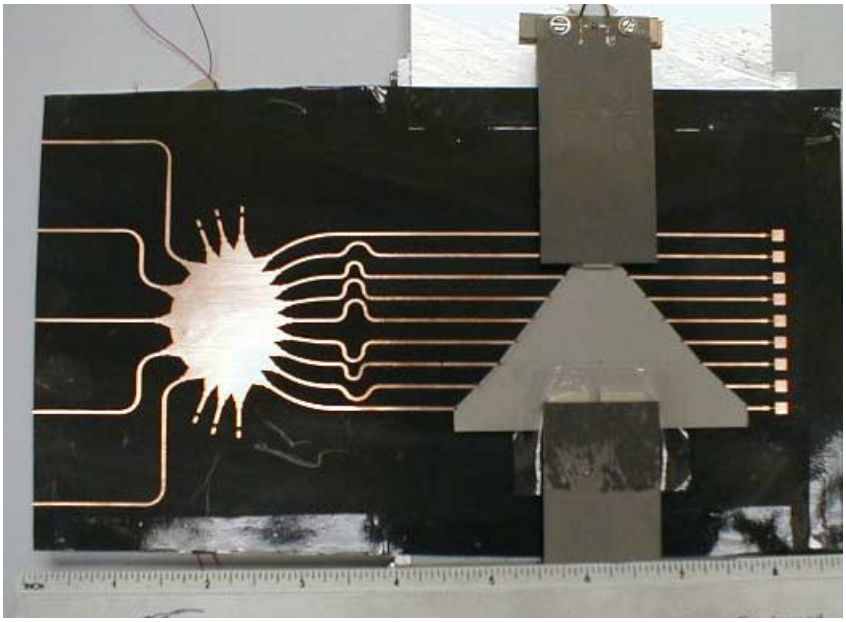

Fig. 39. Photograph of the phased array fabricated using one perturber.

Fig. 38 shows the five-beam phased array designed using the microstrip Rotman lens controlled by PETs. Each beam is steerable in either direction of the *H*-plane using two PET-controlled phase shifters. The photograph of the five-beam phased array fabricated using one perturber is shown in Fig. 39.

Fig. 40 shows the differential phase shifts achieved using a PET-controlled phase shifter at each array port. The progressive phase shifts of 30° using 60 V are designed on nine microstrip lines of Fig. 38 to achieve the beam steering of 8°. Thru-reflect-line (TRL) calibration is used to remove the coaxial connector-to-microstrip transition effect in phase shift measurement. Fig. 40 (a) shows that the microstrip lines are perturbed slightly at 0 V. Although the beams at 0 V are very similar with the beams without perturbation, an external voltage of –20 V may be applied to remove the perturbation completely on the microstrip lines.

Fig. 41 shows the steered beam patterns of the five beams fed by five beam ports and controlled by the phase shifter with an external voltage. Five beams are steered about ±8° using two perturbers shown in Fig. 38. Five beams cover a total of ±38° from the broadside. The nine-element patch array gives 10 dBi antenna gain. The measured antenna patterns show some variations in the sidelobes and antenna gain. The errors are partly due to the integration process. After the phase shifter and the lens are individually optimized on the separate substrate, the complete system including the lens, phase shifter, and array are fabricated in a single substrate. This is to avoid soldering and connectors to the lens and the array, because it is quite difficult to use the connectors due to the small line spacing (6 mm) and additional loss at *Ka*-band. During this process, the lens

performance could be degraded somewhat. The flatness and position of microstrip lines under the perturber might be changed slightly during the integration. Five beams are steered about 8° in one direction, and beams are steered in the other direction by another phase shifter covering ±38° from the broadside.

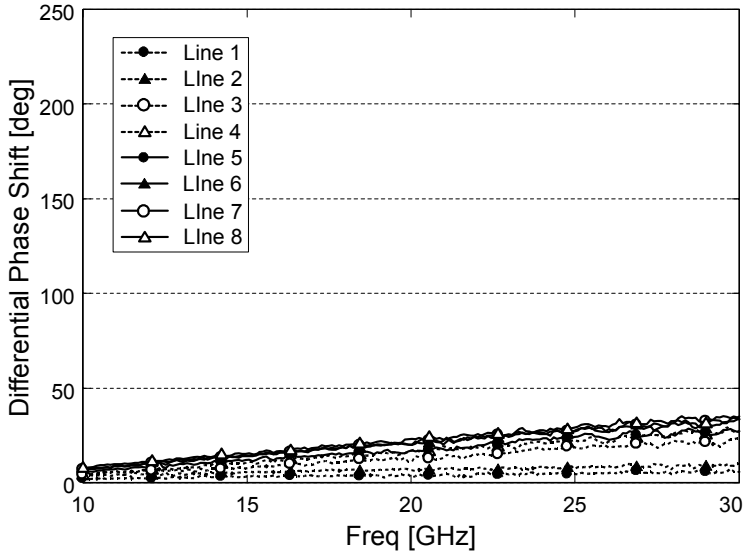

(a)

Fig. 40. Measured differential phase shift of the PET-controlled phase shifter with an external voltage; (a) at 0 V, (b) at 60 V.

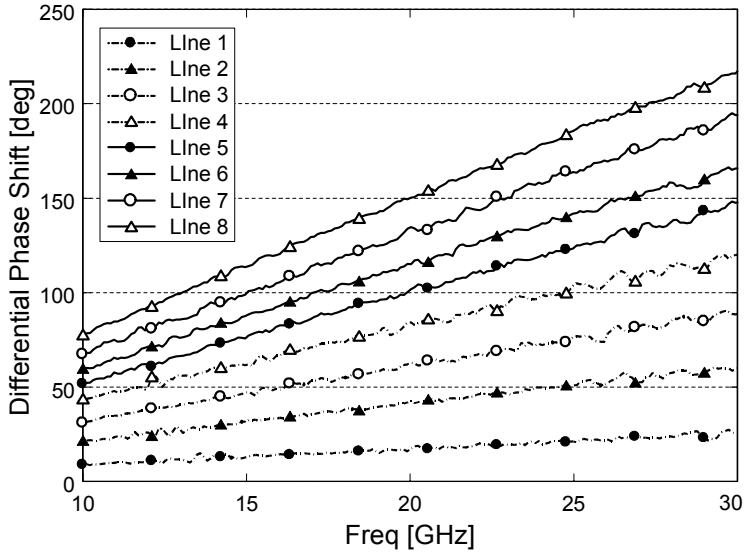

(b)

Fig. 40. Continued.

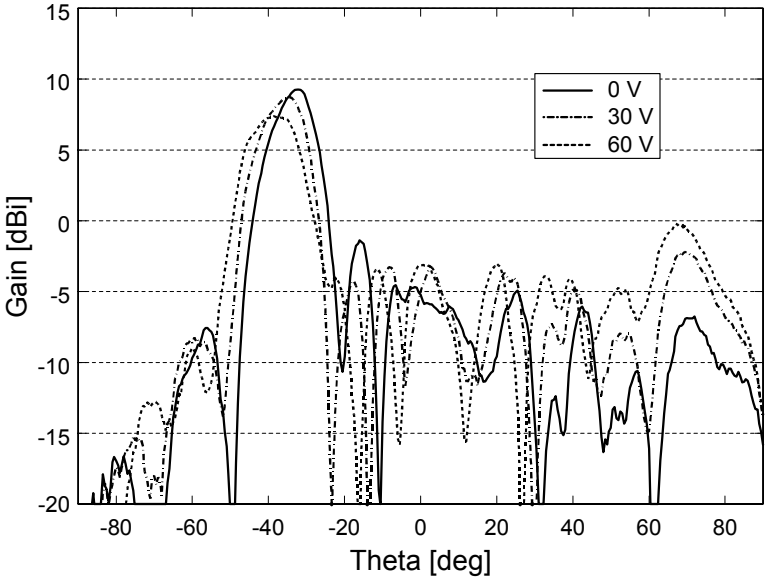

(a)

Fig. 41. Measured *H*-plane patterns for five beams steered by PET-controlled phase shifter; (a) first beam at −30°, (b) second beam at −15°, (c) third beam at 0°, (d) fourth beam at 15°, (e) fifth beam at 30°.

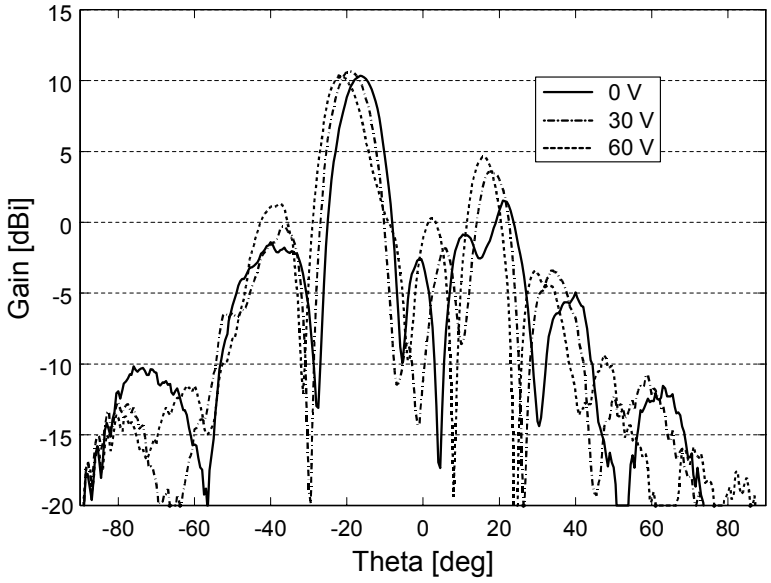

(b)

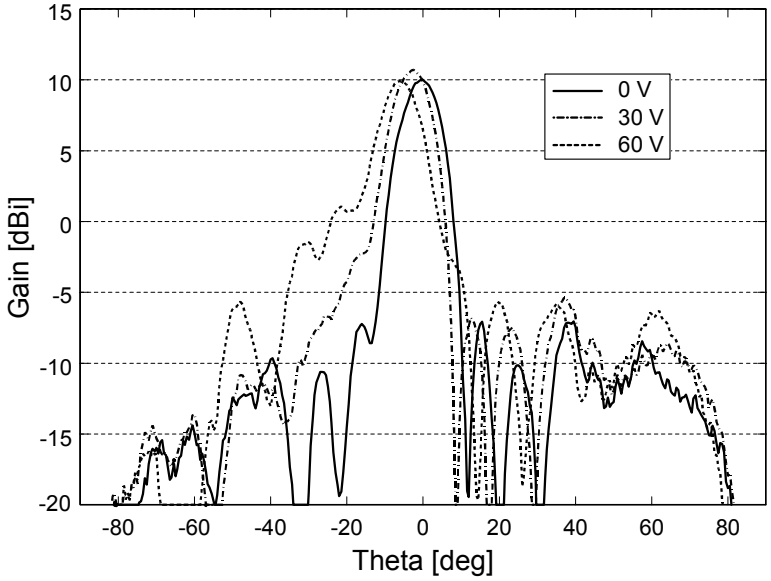

(c)

Fig. 41. Continued.

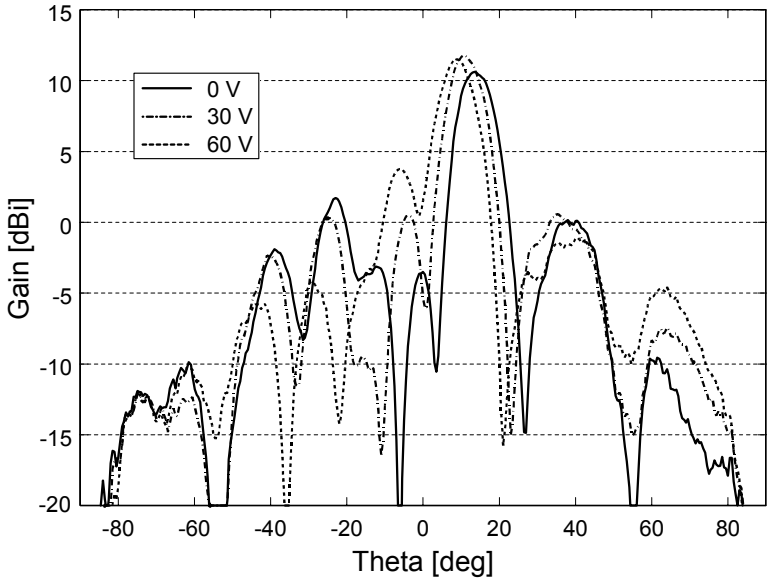

(d)

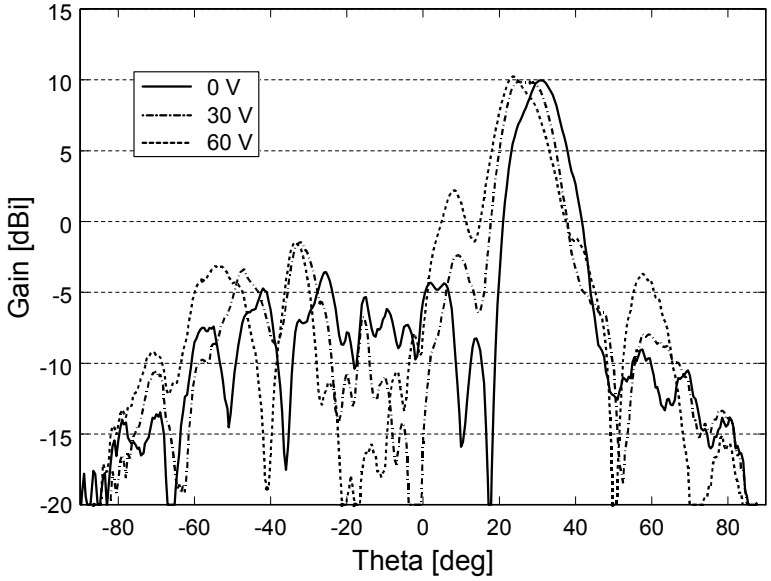

(e)

Fig. 41. Continued.

4. Conclusions

A piezoelectric transducer (PET)-controlled multiple beam phased array using a microstrip Rotman lens has been designed and tested successfully at 30 GHz. The designed Rotman lens has five beam ports and nine array ports matched using a quarterwave transformer. Five beams at the scan angles of 0°, ±15°, and ±30° are steered ±8° by a PET-controlled phase shifter with the external voltage between 0 V and 60 V. Resistive absorbers are used as dummy loads to reduce the reflections by the lens walls. The nine-element rectangular microstrip patch antenna array fed by the microstrip Rotman lens shows more than 10 dBi in antenna gain and more than 10 dB suppression in sidelobe levels. Return loss of better than 15 dB is achieved at 30 GHz. This phased array covers ±38° from the broadside using two PET-controlled phase shifters.

CHAPTER V

WIDEBAND ANTIPODAL TAPERED SLOT ANTENNA ARRAY AND TWO-DIMENSIONAL BEAM SCANNING

1. Introduction

Since Gibson developed a tapered slot antenna known as Vivaldi antenna [18], much research has focused on the design of such wideband antennas [19, 22-24, 26-28]. This type of antenna has been applied to satellite communication, remote sensing, and radio telescope for radio astronomy [19]. Endfire tapered slot antennas fabricated on dielectric substrates hold great potential to reduce cost and weight of antenna systems. Other advantages include the capability to produce a symmetrical beam in the *E*- and *H*-plane, or to tailor the beamwidth by varying the shape, length, dielectric thickness, and dielectric constant of the tapered slot antenna [22].

As a modified tapered slot antenna, an antipodal tapered slot antenna was proposed [20, 25]. Very wideband performance can be achieved using an antipodal tapered slot antenna with its inherently simple wideband transition from microstrip line to antipodal slot line. However, two tapered flares on different layers make higher cross-polarization compared with a traditional Vivaldi antenna. Naturally, the thinner substrate thickness gives the lower cross-polarization level. Langley *et al.* introduced a balanced antipodal Vivaldi antenna to reduce cross-polarization level using three-layered tapered slot flares fed by stripline [21]. Tapered slot antennas fabricated on microstrip or stripline use an

exponential taper known as Vivaldi, linear taper, broken linear taper, and constant width slot.

In this research, an antipodal exponentially-tapered slot antenna (ATSA) is designed to achieve two octaves of bandwidth, and low-cost one- and two-dimensional scanning schemes are demonstrated using ATSA arrays and piezoelectric transducer (PET)-controlled phase shifters. A 4×4 ATSA array is designed for two-dimensional scanning, and the beam is steered using two sets of PET-controlled phase shifters. One set consisting of four identical PET-controlled phase shifters is used to steer the beam in the *E*-plane, and the other is used for steering in the *H*-plane. Using two sets of PET-controlled phase shifters, the beam is steered over 30° in both planes.

2. Antipodal exponentially-tapered slot antenna

A. Design

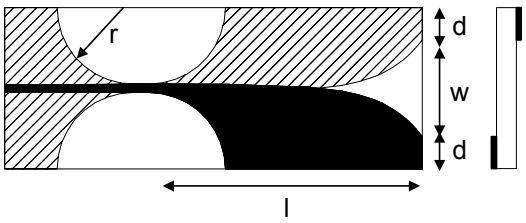

Fig. 42. The designed ATSA element.

Fig. 42 shows the designed antipodal exponentially-tapered slot antenna (ATSA). This antenna is fed using a microstrip line through a parallel-strip transition. Generally, with the wider width *d*, measured from the aperture edge to the substrate edge, the better

return loss results [24]. However, when it is used in an array, the total width of the single element should be sufficiently small to prevent grating lobe formation at the highest operating frequency.

The performance of a tapered slot antenna is sensititive to the thickness and dielectric constant of an antenna substrate. The acceptable range of the effective thickness derived experimentally is given as $0.005\lambda_o \leq t_{eff} \leq 0.03\lambda_o$. t_{eff} is defined as $t(\sqrt{\varepsilon_r}-1)$ [22]. From this experimental bound and the availability of material, an RT/Duroid 5880 with a dielectric constant of 2.2 and thickness of 0.38 mm is chosen as the substrate for antenna fabrication.

The antenna element is simulated with CST Microwave Studio® to determine the optimum opening rate and the slot width [65]. The slot flare is tapered exponentially with the opening rate T [1/mil] of 0.004, of which the shape is determined by

$$y = c_1 e^{Tx} + c_2 \tag{14}$$

where c_1 and c_2 are determined by the coordinates of the first and last point of the exponential curve.

Two ATSAs are designed with different dimensions, as shown at Table 3. Type A is designed for a 10 to 35 GHz *H*-plane array, and Type B is for a two-dimensional scanning array at *X*-band. The antenna widths ($2d+w$) of Type A and B are designed as 25.4 and 17.8 mm, respectively, considering the mechanical stability (stiffness) of material and the emperical design guideline [22]. These dimensions correspond to 0.85 λ_o and 0.6 λ_o at 10 GHz, where λ_o is the free space wavelength. The slot length is

designed as 43.2 mm for both types. The line widths of microstrip and parallel-strip line are 1.14 and 1.32 mm, respectively. The ground plane of microstrip line is tapered circularly for the transition to parallel-strip line.

Table 3. The dimensions of ATSA [unit: mm]

Design parameter	Type A	Type B
Slot length: *l*	43.2	43.2
Conductor width: *d*	5.08	2.54
Slot width: *w*	15.24	12.7
Radius of the transition: *r*	12.04	8.23

B. Performance

Fig. 43 shows the measured return losses of the designed ATSAs. The return losses of two antennas are better than 10 dB from 9 to 40 GHz. From the measured return loss and pattern, Type A is slightly better than Type B due to wider antenna width.

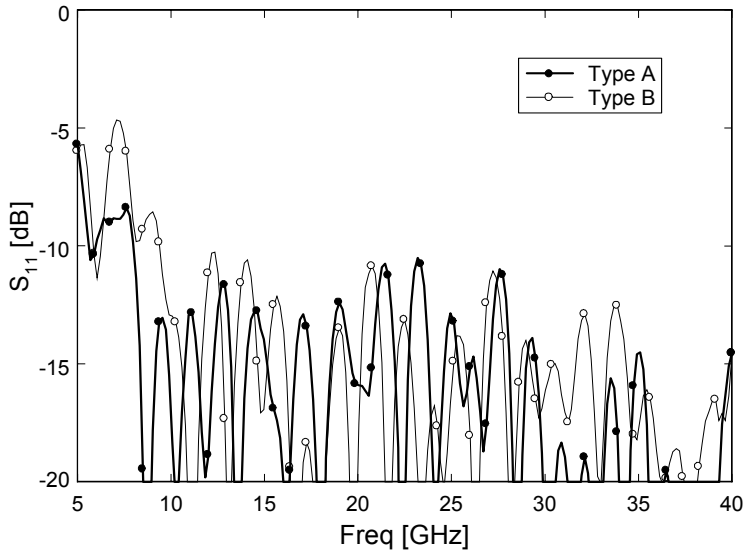

Fig. 43. The measured return loss of the designed ATSA elements.

Fig. 44 shows the *E*- and *H*-plane antenna patterns measured at 10, 20, and 35 GHz. The measured antenna gain varies 5 to 10 dBi over the operating frequencies. The cross-polarization levels are less than –10 dB for all frequencies.

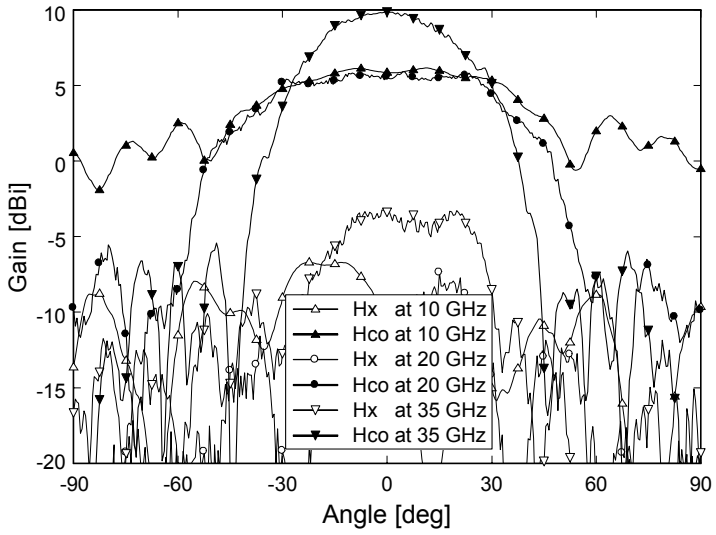

(a)

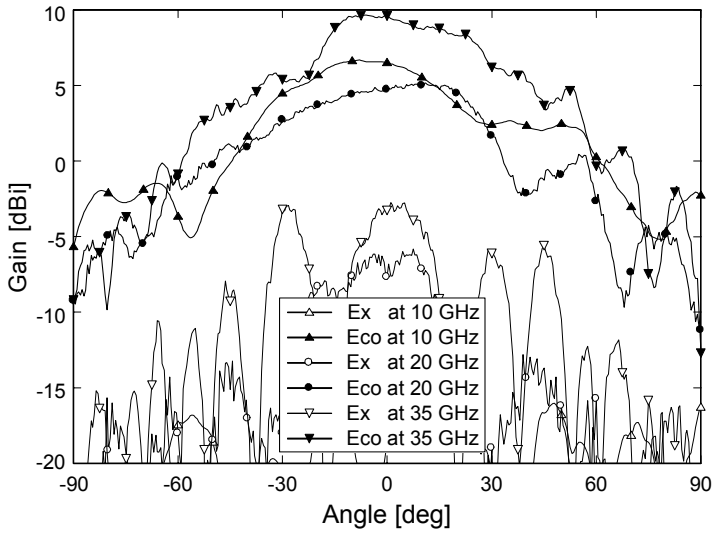

(b)

Fig. 44. The measured radiation patterns of the designed ATSA element (Type A); (a) *H*-plane, (b) *E*-plane.

3. Low cross-polarized antipodal tapered slot antenna array

A. Mirrored ATSA design

Though able to provide very wideband performance, ATSA elements and arrays traditionally suffer from high cross-polarization levels due to the placement of the tapered slot flares on different layer of the same substrate. This problem can be eliminated, however, by mirroring the elements in the array. Fig. 45 shows the conventional *E*- and *H*-plane arrays using ATSAs. As the slot flares are on the different layers of the substrate, the electric fields from each ATSA add up not only at co-polarized direction, but also at cross-polarized direction. Therefore, ATSA antennas and arrays suffer from high cross-polarization, although they have very simple structures and wideband performance.

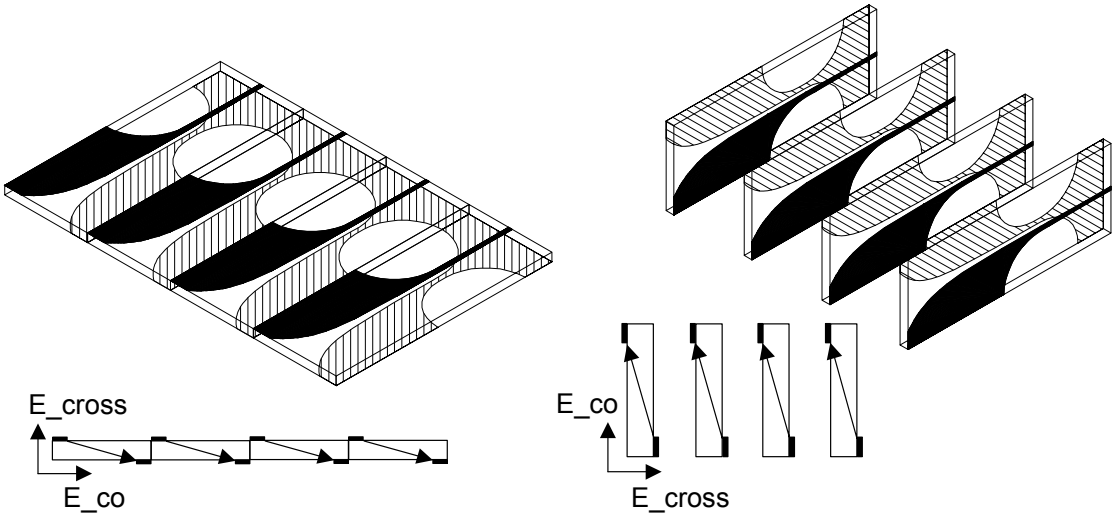

Fig. 45. Conventional ATSA array architecture in the *E*- and *H*-plane (the electric fields are shown in the front view).

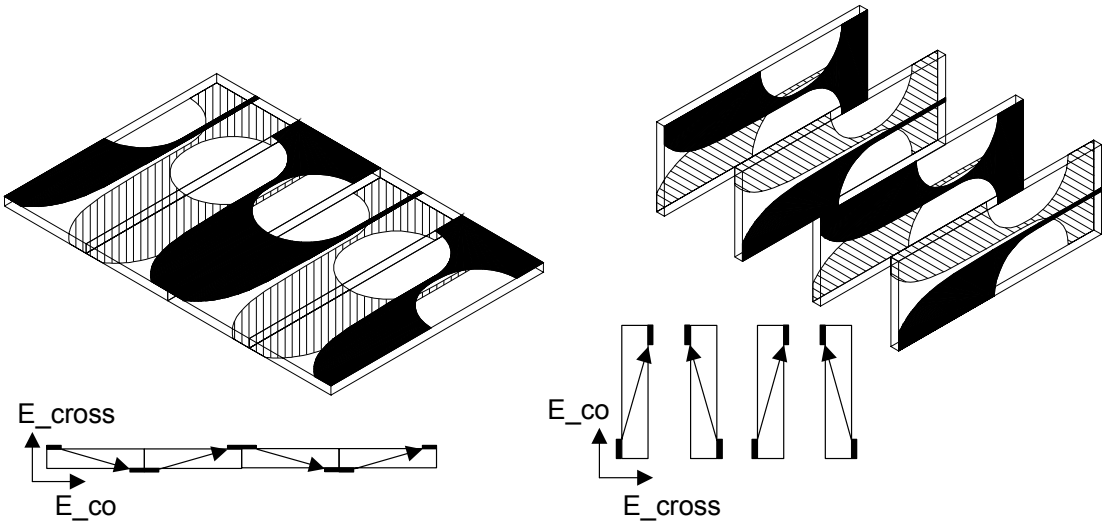

Fig. 46. Proposed mirrored ATSA array architecture in the *E*- and *H*-plane (the electric fields are shown in the front view).

Fig. 46 shows the new *E*- and *H*-plane architectures to reduce cross-polarization levels. The electric fields from each element are added up at co-polarized direction, and cancelled out at cross-polarized direction. Using a mirrored ATSA array, the cross-polarization levels are reduced greatly, maintaining the co-polarized patterns almost the same as those of a conventional array.

An ATSA element is designed to cover from 5 to 11 GHz for demonstration. The length and width of the designed ATSA are 43.2 mm and 17.8 mm, respectively. The slot flare is tapered exponentially. CST Microwave Studio® is used to optimize the slot flare and the slot width, and to simulate antenna patterns of its array. A wideband power divider with three-step Chebyshev impedance transformer is used to feed the *E*- and *H*-plane ATSA arrays. The array spacing is 17.8 mm which means $0.3\lambda_o$ at 5 GHz and $0.65\lambda_o$ at 11 GHz.

B. Measurements

The antenna is etched on an RT/Duroid 5880 substrate with the dielectric constant of 2.2 and the thickness of 0.787 mm. The measured return loss of the antenna array including the power divider is better than 10 dB in the target frequency range. Fig. 47 shows the antenna patterns of the *E*- and *H*-plane measured at 9 GHz. Using the mirrored array, the cross-polarization levels have been reduced by more than 20 dB at the broadside. As the cross-polarized electric fields from antenna elements are cancelled out, this mirrored array arrangement makes it possible to use thick substrate for easy fabrication.

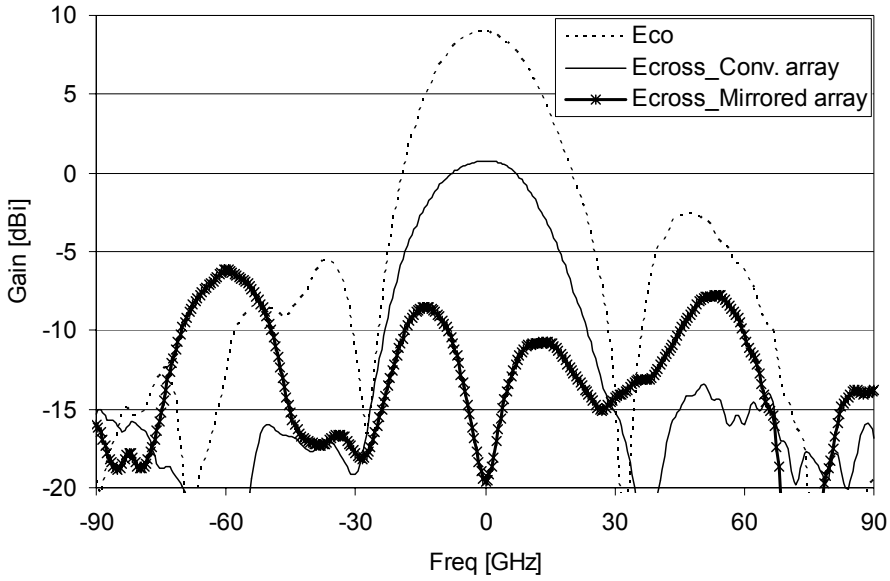

(a)

Fig. 47. Antenna patterns measured at 9 GHz; (a) *E*-plane, (b) *H*-plane.

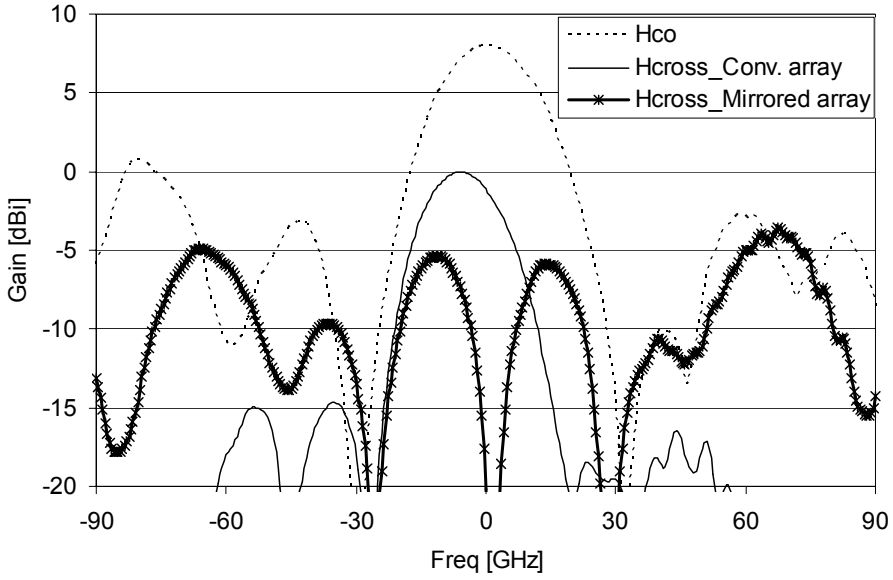

(b)

Fig. 47. Continued.

Fig. 48 shows the measured cross-polarization level reductions of the conventional and mirrored arrays shown in Figs. 45 and 46. In the conventional array, the cross-polarized electric fields are added up at the broadside. Therefore, the cross-polarization level is only 10 dB down (at 11 GHz) from the co-polarization level at the broadside. This is due to the placement of the tapered slot flares on different layer of the substrate. The co-polarized patterns and gains are almost same in both arrays. However, in the mirrored array, the cross-polarization levels are ideally null at the broadside, because the cross-polarized electric fields are cancelled out at the broadside. The measured results show great reductions in cross-polarization levels for the mirrored arrays.

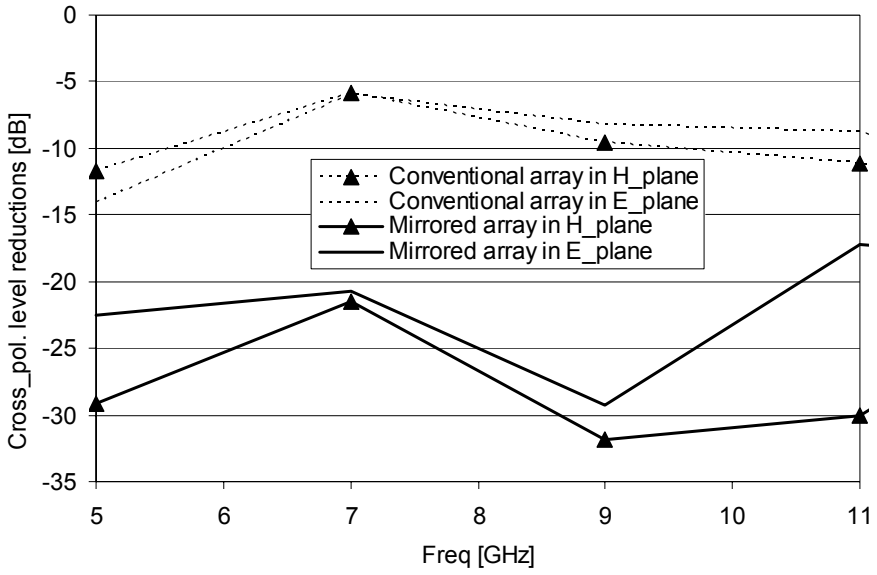

Fig. 48. Measured cross-polarization level reductions from the co-polarized patterns at the broadside in the *E*- and *H*-plane.

4. Wideband 1×4 *H*-plane phased array

Fig. 49 (a) shows the configuration of the wideband 1×4 *H*-plane array. Type A design is used for the antenna element, and the antenna spacing is designed as 6.1 mm in the *H*-plane, which corresponds 0.2 λ_o at 10 GHz and 0.7 λ_o at 35 GHz. Because the spacing is sufficiently small to cover 10 to 35 GHz, the array itself has very wide bandwidth performance. The antipodal antennas and the mirrored elements are placed alternately in the *H*-plane to cancel out the cross-polarized fields at the broadside.

Four perpendicular microstrip transitions are used to connect the phase shifter to feed the *H*-plane array, as shown in Fig. 49 (b). As the electric fields are decoupled at the transition, the degradation in the insertion loss and return loss is measured beyond 20

GHz. To improve the performance of the transition at *Ka*-band, a Coax of 50 Ohm is inserted between the perpendicularly connected microstrip lines. This modified transition gives better performance up to 35 GHz.

Fig. 49 (c) shows the photograph of the fabricated phased array. The key components are a 1×4 *H*-plane array and a multi-line PET-controlled phase shifter. In addition, a wideband power divider, which is designed using four-section Chebyshev impedance transformer, is connected to the PET-controlled phase shifter to feed the array.

The PET-controlled phase shifter shown in Fig. 49 (c) is fabricated on an RT/Duroid 6010 (ε_r=10.2) with the thickness of 0.38 mm. A 1.27 mm thick TMM10 (ε_r=9.2) is used as the perturber. The maximum progressive phase shift of 90° at 35 GHz is designed to achieve the scan angle of 20°. The phase shift is proportional to the coverage length of the triangularly shaped perturber. Therefore, the length of the perturber over each microstrip line is designed to be integer multiples of each other at 1.2, 2.4, and 3.6 cm, achieving a progressive phase shift. The line spacing at the phase shifter is designed as 10 mm, considering T/R modules to be connected between the array and the phase shifter. Therefore, a space adapter from 10 to 6.1 mm is used to connect the array and the phase shifter.

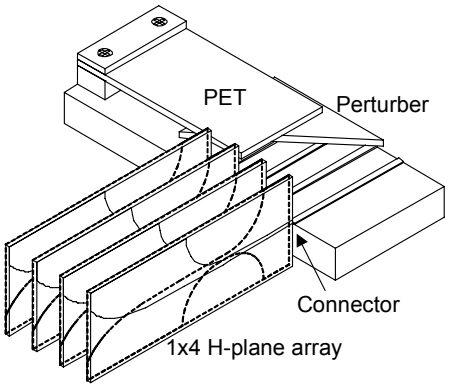

(a)

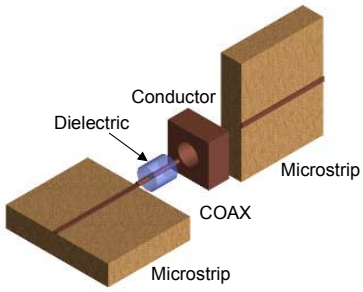

(b)

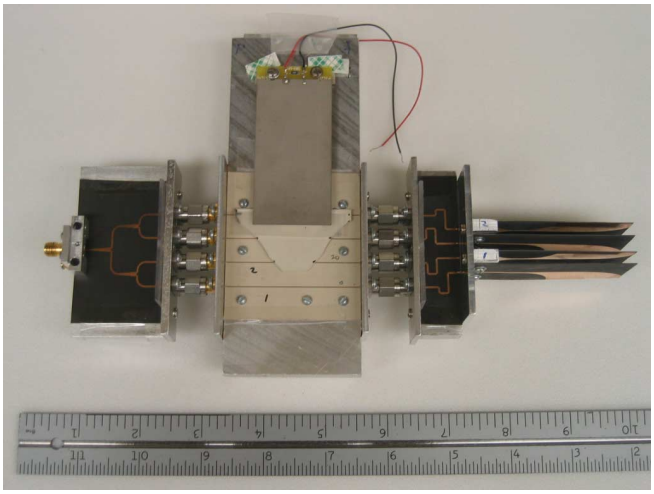

(c)

Fig. 49. The configuration of the 1×4 *H*-plane array and perpendicular transition; (a) the 1×4 *H*-plane array, (b) perpendicular microstrip transition connector, (c) photograph of the fabricated 1×4 *H*-plane array.

Fig. 50 shows the measured *S*-parameters and differential phase shifts of the phase shifter. The return loss is better than 10 dB for the target frequencies, and the insertion loss is less than 4 dB at 35 GHz with full perturbation. The insertion loss includes the losses due to the connectors and line lengths. Fig. 51 shows the steered beam patterns measured at 10, 12, 19, 21, 32, and 35 GHz. The beam is steered in the *H*-plane using the PET-controlled phase shifter with the external voltage of 40 V. The antenna gain of the phased array is more than 3 dBi including all losses due to the components, and each beam is steered more than 20 ° at the entire frequency ranges. The antenna gain will be increased using T/R modules to be developed.

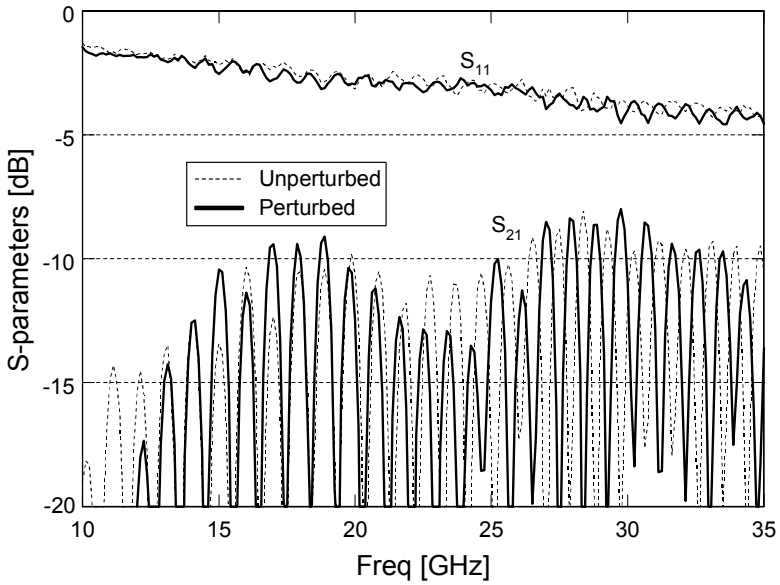

(a)

Fig. 50. The measured performance of the PET-controlled phase shifter; (a) *S*-parameters, (b) differential phase shifts.

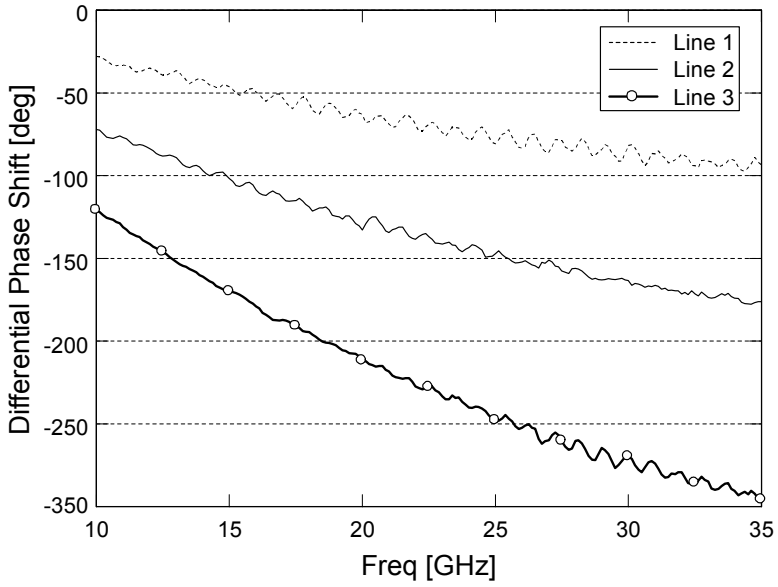

(b)

Fig. 50. Continued.

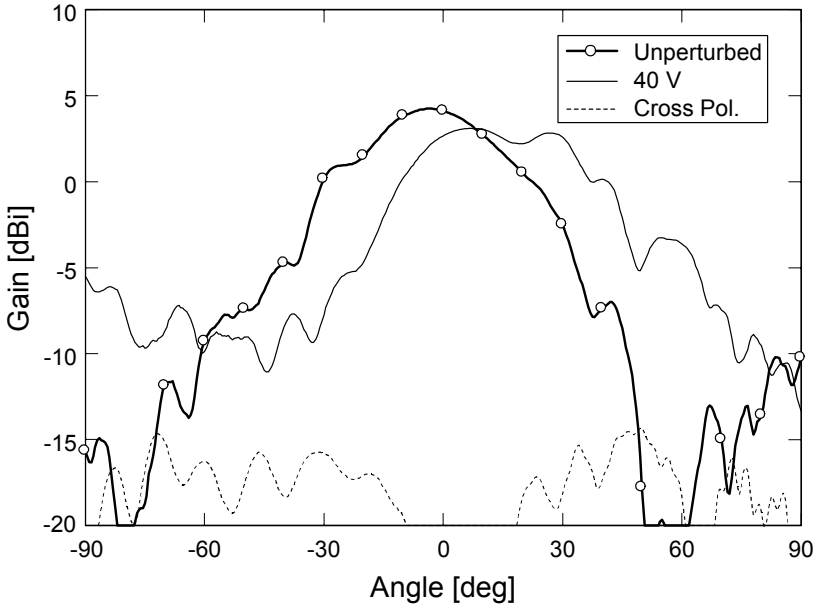

(a)

Fig. 51. The measured *H*-plane beam patterns of 1×4 *H*-plane array; (a) at 10 GHz, (b) at 12 GHz, (c) at 19 GHz, (d) at 21 GHz, (e) at 32 GHz, (f) at 35 GHz.

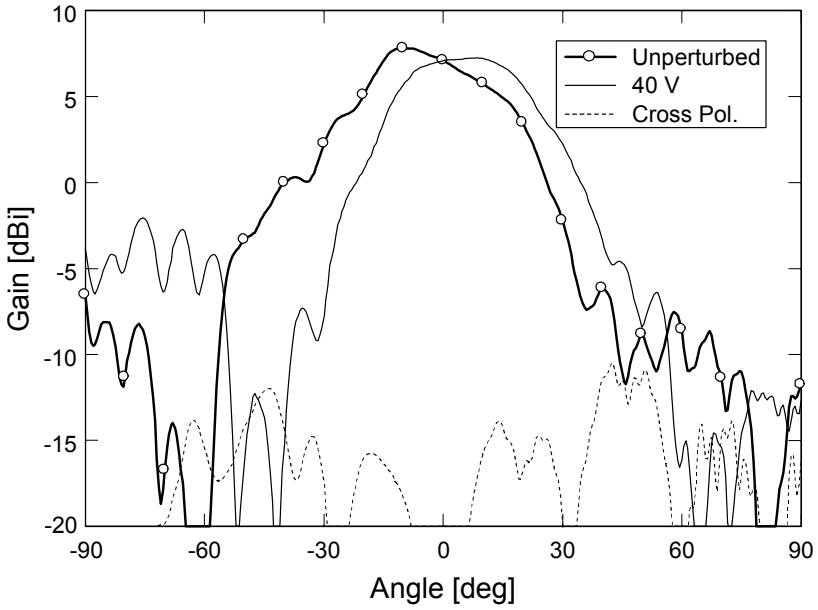

(b)

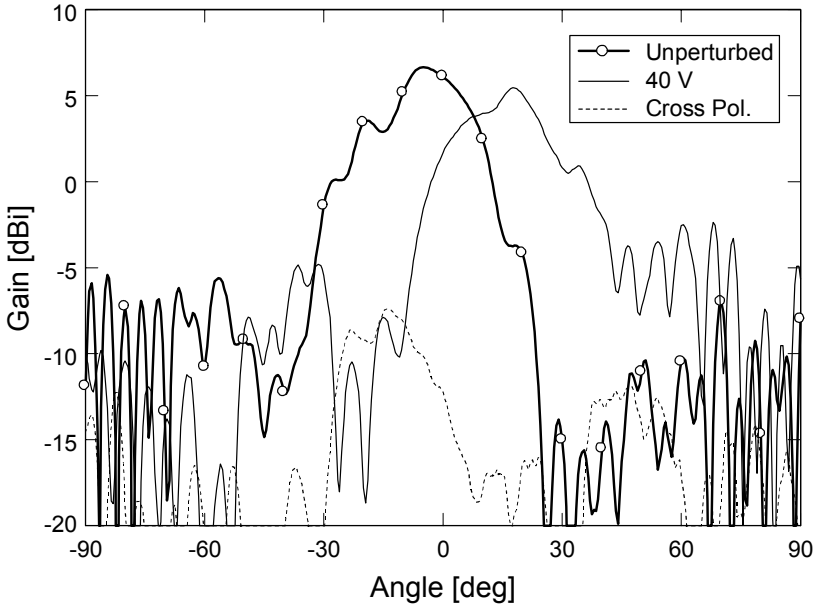

(c)

Fig. 51. Continued.

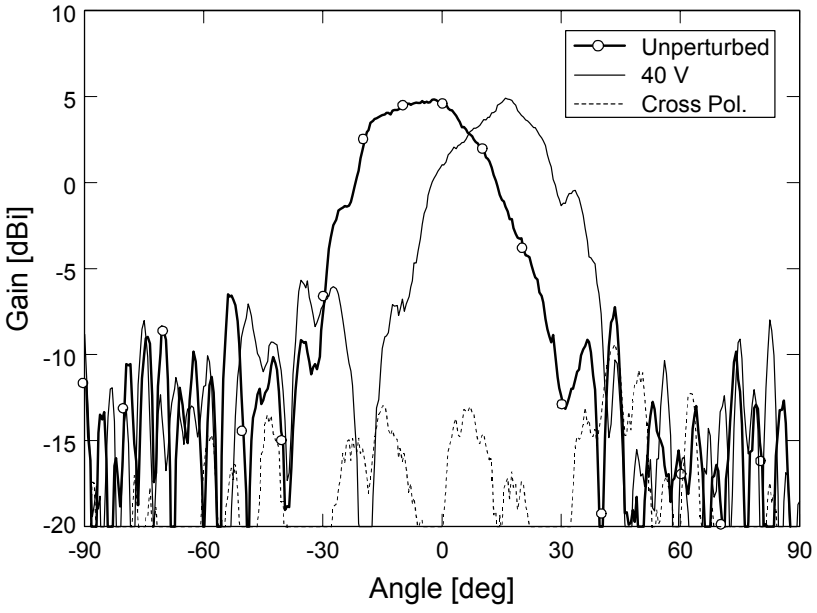

(d)

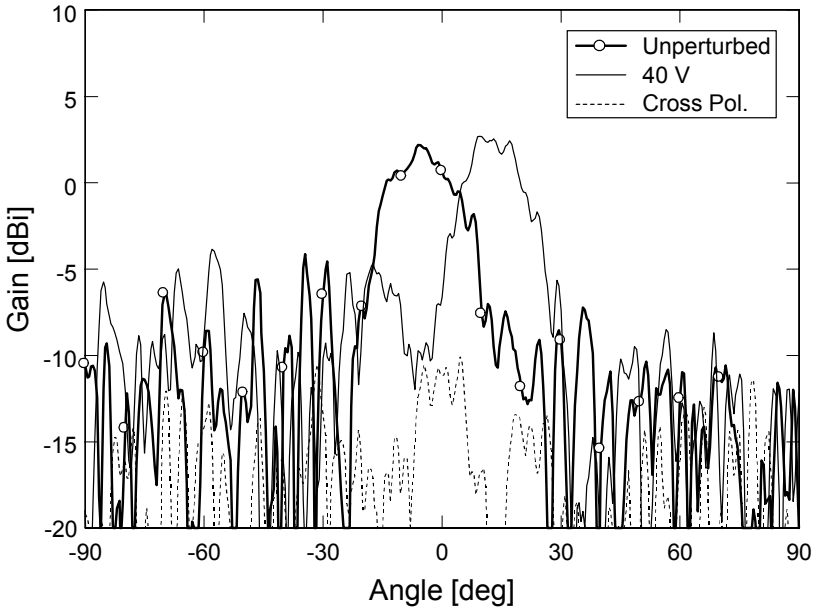

(e)

Fig. 51. Continued.

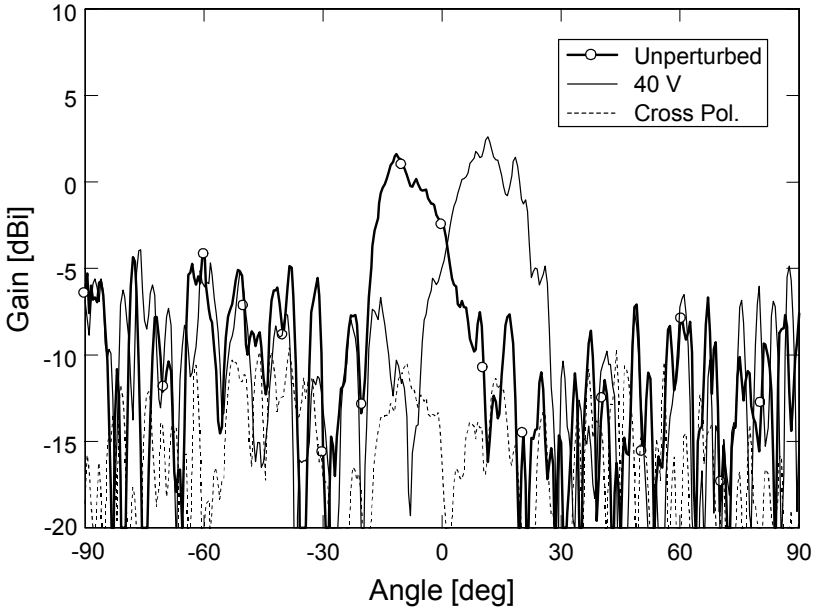

(f)

Fig. 51. Continued.

5. 4×4 two-dimensional scanning array

A. Configuration of a two-dimensional scanning array controlled by PET.

Fig. 52 shows the entire configuration of a two-dimensional scanning array operated by PET-controlled phase shifters. The operating frequency is *X*-band for concept demonstration. Four 1×4 *E*-plane phased arrays with a PET-controlled phase shifter are stacked on the *H*-plane, and another PET-controlled phase shifter for scanning in the *H*-plane is placed after four wideband power dividers. A 4×4 ATSA array is designed using Type B antenna. Although this antenna element itself has very wideband performance, the beam steering is demonstrated at 8 to 12 GHz to avoid grating lobes. The *E*-plane antenna spacing at 10 GHz is $0.6\lambda_o$ limited by the ATSA element width,

and the spacing in the *H*-plane is designed as $0.474\lambda_o$ at 10 GHz. These spacings are acceptable for the scanning up to 30°. This array system is free of grating lobe up to 12 GHz.

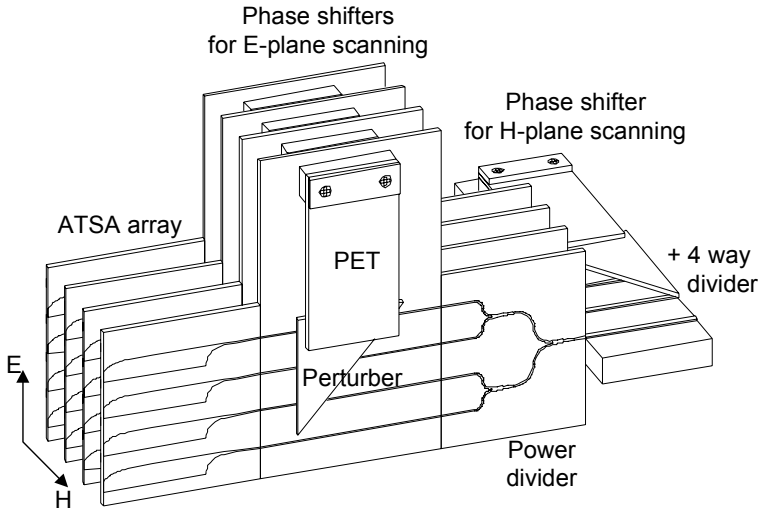

Fig. 52. Configuration of two-dimensional scanning array controlled by PETs.

B. Design of PET-controlled phase shifters

Two sets of PET-controlled phase shifters are fabricated to steer the beam in both planes. One set consisting of four PET-controlled phase shifters is used to steer the beam in the *E*-plane, and the other one is used to steer in the *H*-plane. Four identical phase shifters for beam steering in the *E*-plane should have the same performance in the progressive phase shift. The progressive phase shifts of 100° using 50 V are designed on four microstrip lines to achieve a scan angle of 30°. The PET is deflected by an external voltage, and this voltage causes the air gap between the microstrip line and perturber to

change. Because the phase shift is proportional to the coverage length of the triangular perturber, the perturber's length over each microstrip line is designed to be 2, 4, and 6 cm at each line for progressive phase shift, respectively.

The differential phase shift $n\Delta\phi$ on the nth microstrip line caused by the perturbation is calculated as

$$n\Delta\phi = nL_1 \cdot \frac{2\pi}{\lambda_o}\left(\sqrt{\varepsilon_{eff}(f)} - \sqrt{\varepsilon'_{eff}(f)}\right), \quad n = 1, 2, 3 \tag{15}$$

where L_1 is the length of perturber over the first microstrip line, and $\varepsilon_{eff}(f)$ and $\varepsilon'_{eff}(f)$ are the effective relative permittivities of the unperturbed and perturbed microstrip line, respectively. The progressive phase shift between any two neighboring microstrip lines is $\Delta\phi$.

The PET-controlled phase shifter is fabricated on an RT/Duroid 5880 (ε_r=2.2) with the thickness of 0.38 mm. An RT/Duroid 6010.2 with a dielectric constant of 10.2 and thickness of 1.27 mm is used as the dielectric perturber for the phase shifter. However, it is noted that a higher permittivity of the perturber than that of the substrate degrades the performance of phase shifter by high insertion loss at a high frequency range (over 20 GHz) due to leaky wave mode generation with the large amount of phase shift [1]. The phase shifter performance measured at *X*-band shows the insertion loss below 3 dB and the return loss over 10 dB with perturbation, as shown in Fig. 53 (a). Fig. 53 (b) shows the differential phase shifts achieved for one of the PET-controlled phase shifters used for beam steering in the *E*-plane.

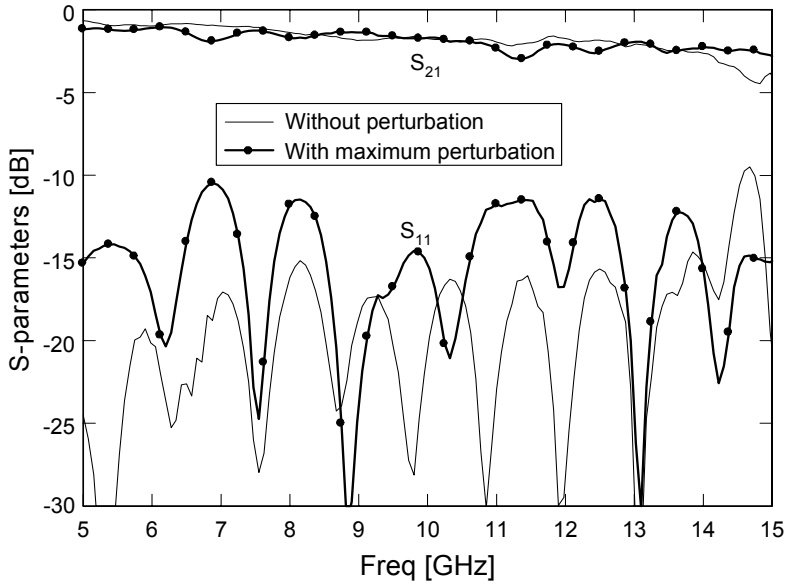

(a)

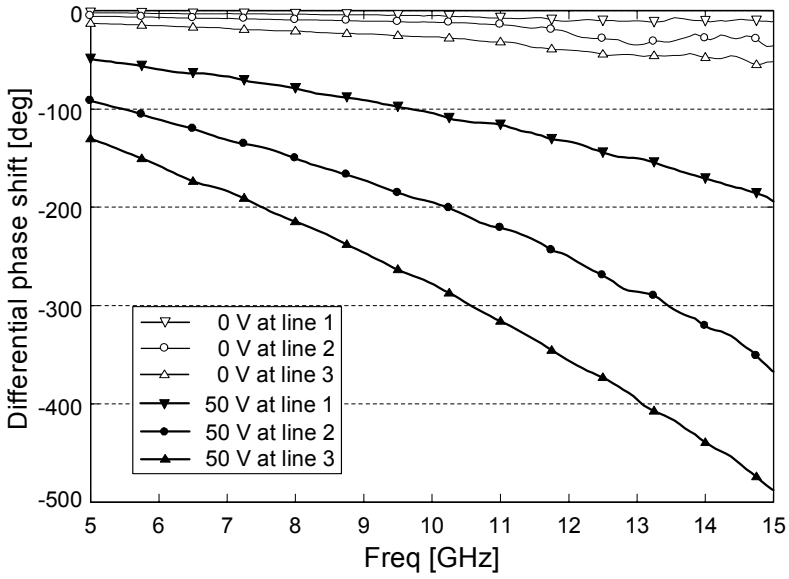

(b)

Fig. 53. Measured performance of the PET-controlled phase shifter with an external voltage of 50 V; (a) *S*-parameters, (b) differential phase shifts.

C. 1×4 *E*-plane phased array

Fig. 54 (a) shows the photograph of the fabricated 1×4 *E*-plane array, and the measured beam steering patterns are shown in Fig. 54 (b). It can be seen that a beam steering of over 30° has been achieved. The bent microstrip lines in Fig. 54 (a) are used to maintain the same phases at the antenna inputs of the *E*-plane array.

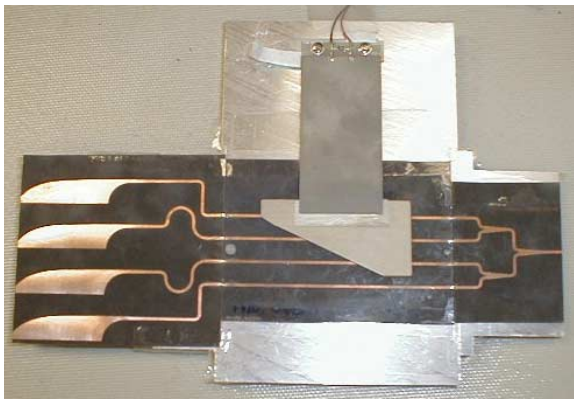

(a)

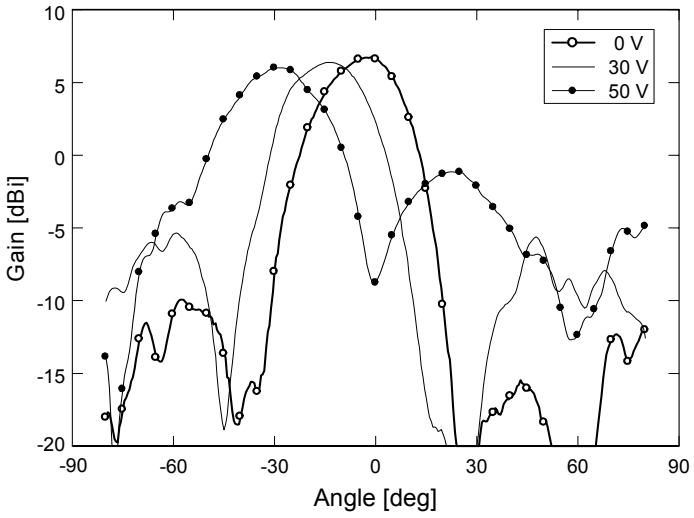

(b)

Fig. 54. Photograph and beam steering of 1×4 *E*-plane array; (a) photograph, (b) beam steering performance.

D. 4×4 two-dimensional phased array

Fig. 55 shows the photograph of the fabricated 4×4 ATSA array controlled by PET-controlled phase shifters. The radiation patterns of the designed antenna element (Type B) are similar with the those of Type A shown in Fig. 44.

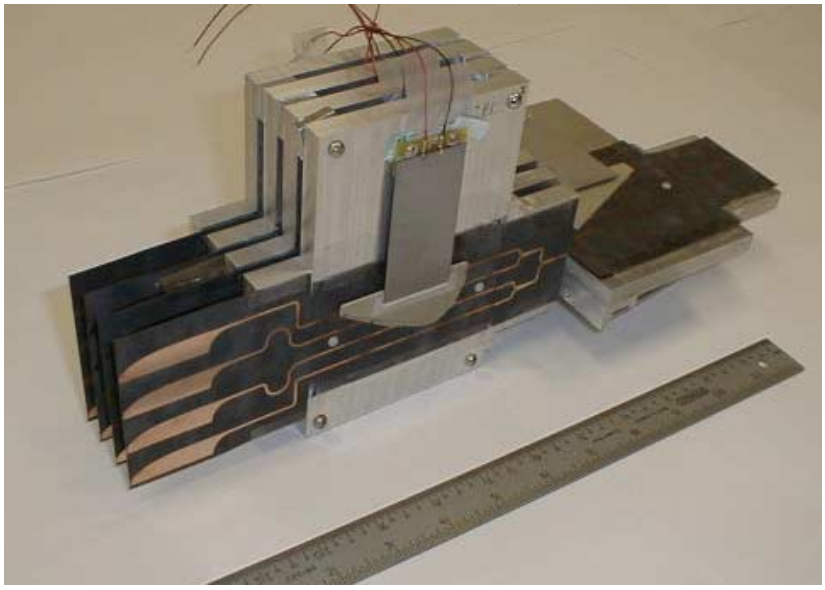

Fig. 55. Photograph of the fabricated 4×4 ATSA array operated by PET-controlled phase shifters.

Figs. 56, 57, and 58 show the beam steering of the 4×4 two-dimensional array in the *H*-plane and *E*-plane measured at 8, 10, and 12 GHz, respectively. The gain is over 8 dBi including all losses of phase shifters and connections, and the cross-polarization levels are less than −10 dB. The beam is steered over 30° in each plane using each set of phase shifters with an external voltage. The unexpected high sidelobe in the measured patterns is believed due to the unshielded phase shifters, the incomplete progressive

phase shifts on four *E*-plane phase shifters, and the phase delay in the fabricated microstrip transitions and soldering points. These radiation patterns could be further improved by an additional optimization process and finer fabrication tolerances. Although the beam steering is shown in one direction, the beam may be steered in the other direction by another sets of phase shifters as demonstrated in [58].

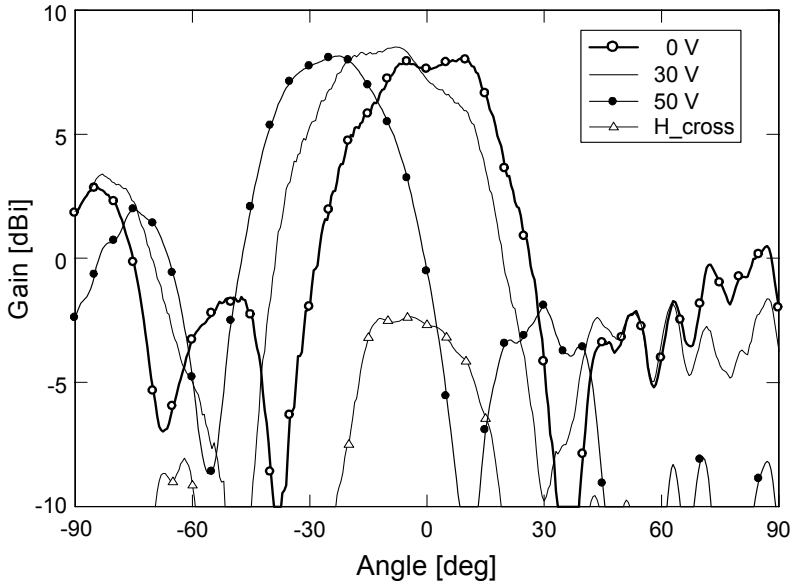

(a)

Fig. 56. Measured scanning pattern of the 4×4 ATSA array operated by PET-controlled phase shifters at 8 GHz; (a) *H*-plane, (b) *E*-plane.

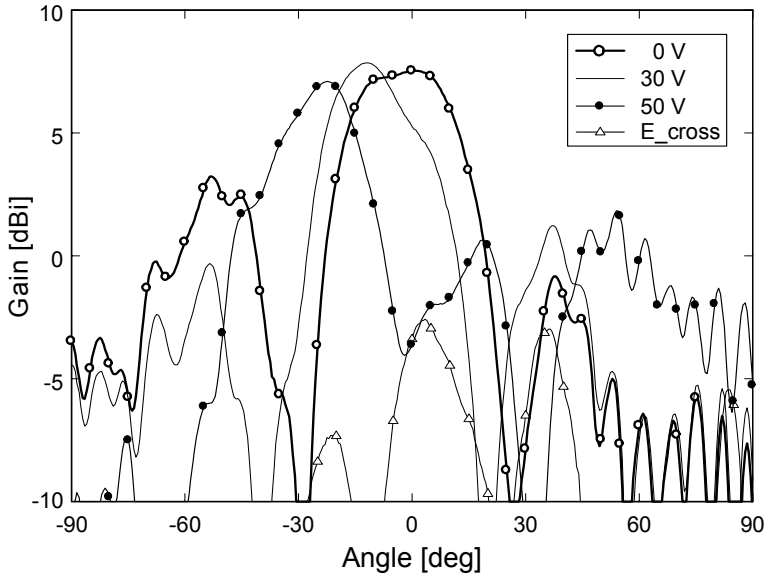

(b)

Fig. 56. Continued.

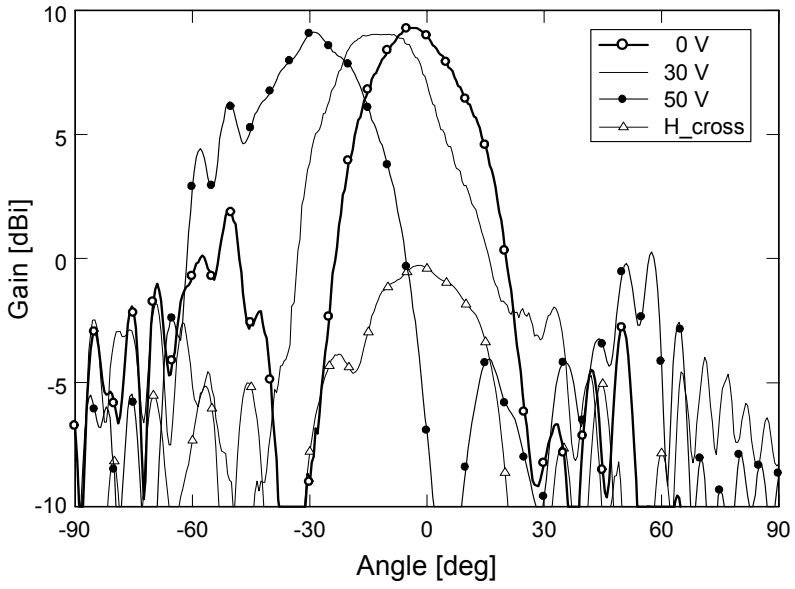

(a)

Fig. 57. Measured scanning pattern of the 4×4 ATSA array operated by PET-controlled phase shifters at 10 GHz; (a) *H*-plane, (b) *E*-plane.

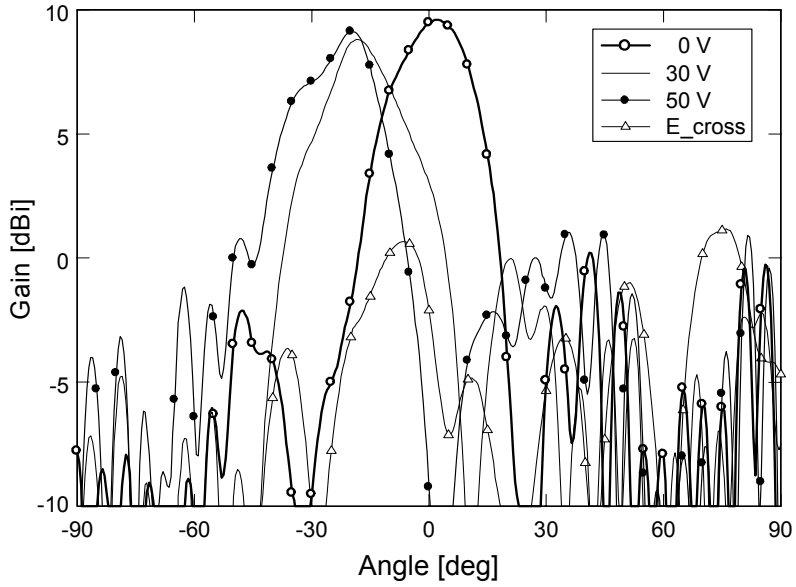

(b)

Fig. 57. Continued.

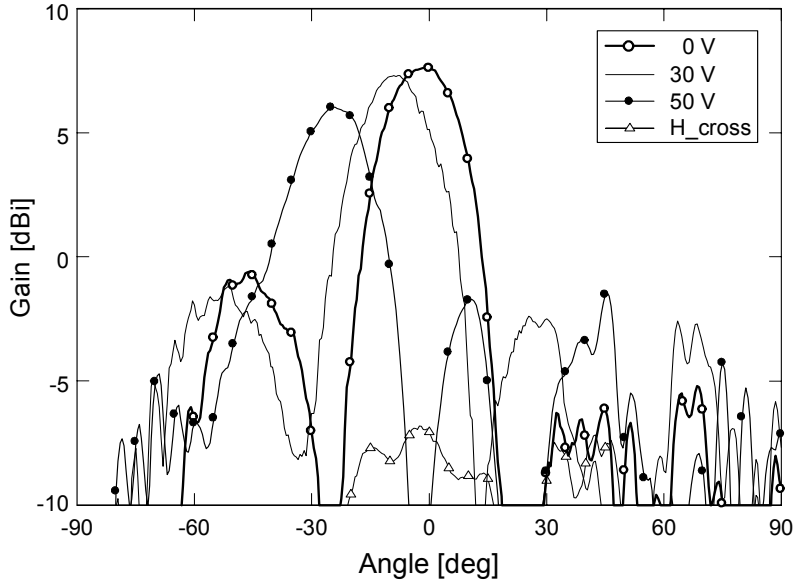

(a)

Fig. 58. Measured scanning pattern of the 4×4 ATSA array operated by PET-controlled phase shifters at 12 GHz; (a) *H*-plane, (b) *E*-plane.

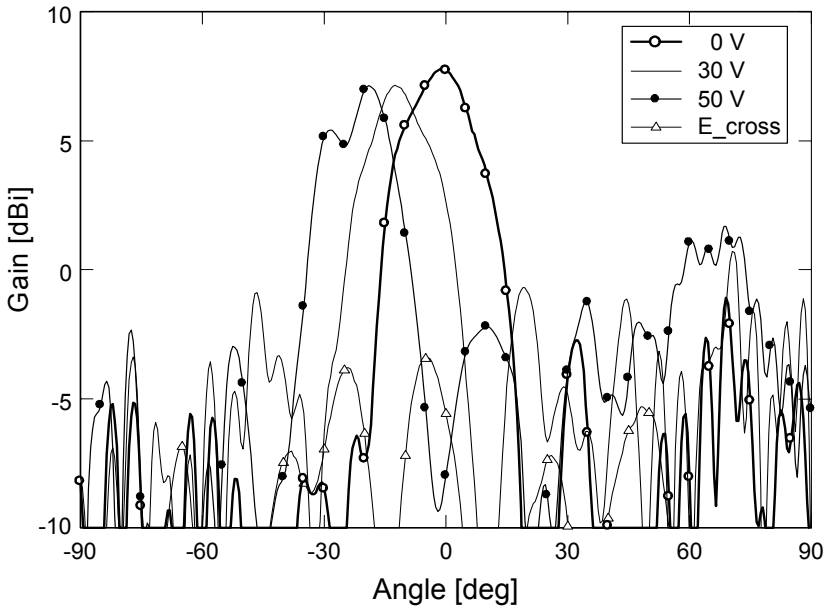

(b)

Fig. 58. Continued.

6. Conclusions

Ultra wideband antipodal exponentially-tapered slot antennas (ATSAs) have been designed, and one- and two-dimensional scanning schemes using piezoelectric transducer (PET)-controlled phase shifters have been demonstrated successfully. The antenna elements cover from 9 to 40 GHz, and the antenna gain varies from 5 to 10 dBi over the operating frequencies. The 4×4 ATSA array operated at *X*-band shows more than 8 dBi in antenna gain including all losses of phase shifters and connections, and more than 10 dB suppression in cross-polarization levels. The beam is steered over 30° in the *H*- and *E*-plane using PET-controlled phase shifters with the external voltages

between 0 and 50 V. The 1×4 ATSA phased array with the scanning capability of 20° was also developed for a multi-channel full-duplex transceiver operating from 10 to 35 GHz. A new ATSA array architecture using “mirrored” elements was used to reduce cross-polarization levels.

CHAPTER VI*

MICROWAVE CIRCUITS USING DOUBLE-SIDED PARALLEL-STRIP LINES

1. Introduction

The transition between an unbalanced line (microstrip, coplanar waveguide) and a balanced line (double-sided parallel-strip line, coplanar stripline) is called a balun. This transition is frequently used to measure microwave circuits using balanced transmission line. Although microstrip line has been preferred because of its planar structure and easy analysis due to the quasi-TEM mode, balanced lines are often useful to feed printed antennas [25, 66], or to fabricate microwave components such as balanced mixers [67].

Recently, coplanar striplines (CPSs) have been extensively used for these purposes. However, CPSs have considerable limitations: (1) to realize low characteristic impedance requires extremely narrow strip or slot dimensions; and (2) to design planar microwave components such as power dividers and junctions requires complex circuit structures compared with their microstrip counterparts. The advantages of double-sided parallel-strip lines are: easy realization of low characteristic impedance line; simplicity in circuit structures of wideband transitions; and good performance of balanced

---

microwave components.

Since double-sided parallel-strip line structure consists of two identical microstrip lines, one on top of another, it can be analyzed easily using image theory as found in the literature [68, 69]. Circularly or linearly tapered transitions to achieve wideband performance have been reported [70, 71]. In this research, ultra wideband microstrip to double-sided parallel-strip transitions using tapered ground strips are presented. The design and performance of a bandpass filter, lowpass filter, and rat-race hybrid using double-sided parallel-strip lines are demonstrated. These results show that double-sided parallel-strip lines can be applied to a broad range of balanced microwave circuits.

2. Analysis of double-sided parallel-strip line

A double-sided parallel-strip line is a balanced line, as shown in Fig. 59. The field distribution in this line remains unchanged if an infinite sized perfect electric conductor is inserted at the center of the substrate and parallel to the strips. Placing this conductor at a distance *h/2* from either strip will convert the double-sided parallel-strip line into a combination of two identical microstrip lines placed back to back. Therefore, the design of the double-sided parallel-strip line is simply related to the design of the microstrip line. For the same strip width, the characteristic impedance of a double-sided parallel-strip line with dielectric separation h is twice the characteristic impedance of a microstrip line with dielectric thickness $t=h/2$. The effective dielectric constant remains the same in this situation [66]. The closed-form design equation for double-sided parallel-strip line can be found in [72].

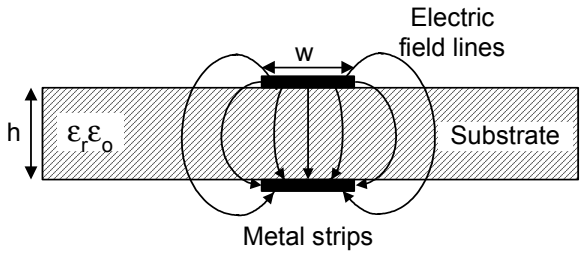

Fig. 59. Cross section of a double-sided parallel-strip transmission line.

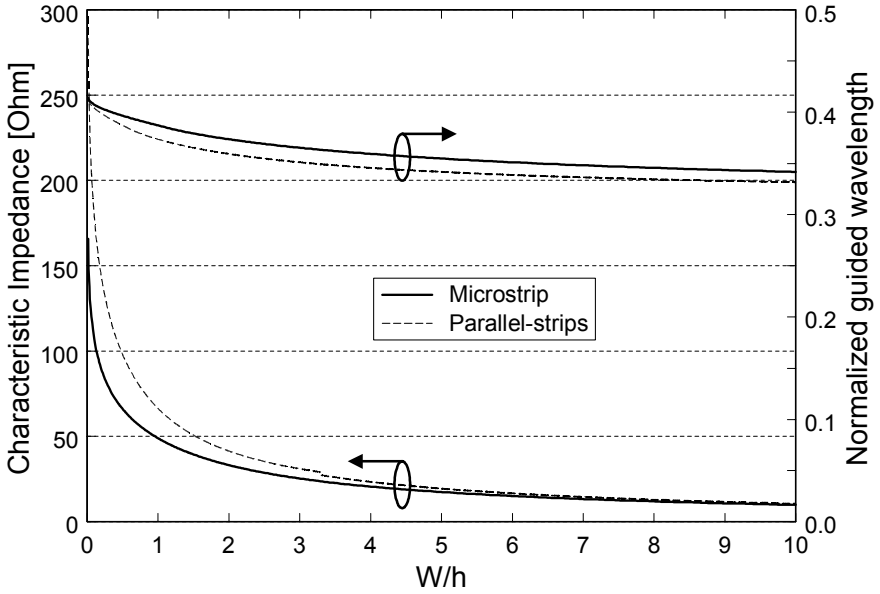

Fig. 60. The characteristic impedance and normalized guided wavelength of microstrip line and double-sided parallel-strip line.

Fig. 60 shows the characteristic impedances and the normalized guided wavelengths of microstrip and double-sided parallel-strip line on the substrate with a dielectric constant of 10. The normalized guided wavelength in Fig. 60 is defined as the ratio of the guided wavelength λ_g to the free space wavelength λ_o. A double-sided parallel-strip line has wider linewidth compared with microstrip line with the same

characteristic impedance. The double-sided parallel-strip line gives shorter wavelength than a microstrip line for the same linewidth.

3. Transitions from microstrip line to double-sided parallel-strip line

Wideband transitions from microstrip line to double-sided parallel-strip line are developed. The ground plane of the microstrip line is partially removed (step tapered), as shown in Fig. 61 (a), or tapered linearly or circularly, as shown in Fig. 61 (b) and (c). The radius *R* used in the circularly tapered transition is 7.6 mm.

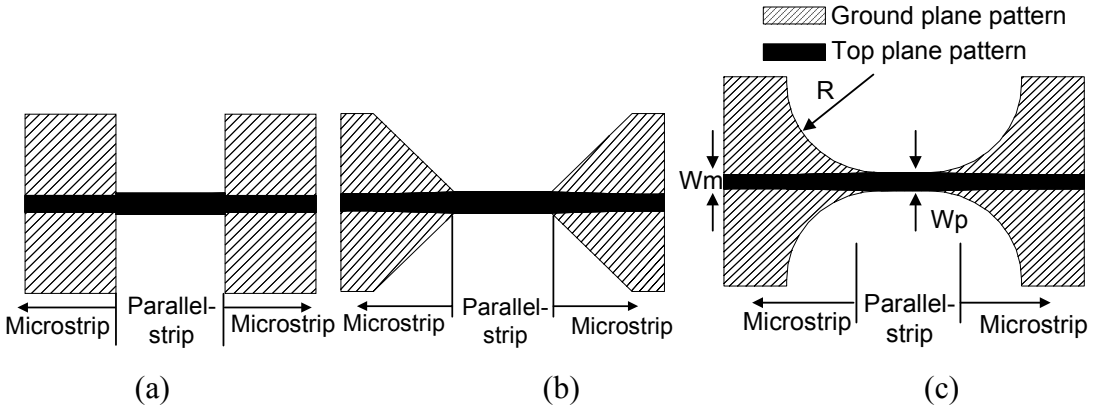

Fig. 61. Configurations of the back-to-back transition from microstrip line to double-sided parallel-strip line; (a) step tapered, (b) linearly tapered, (c) circularly tapered.

The transition is fabricated on two different substrates. To evaluate the transition performance, two back-to-back transitions are designed for the measurement purpose. Fig. 62 (a) shows the measured *S*-parameters including two microstrip to coaxial line connector effects. The return loss is better than 10 dB from 1 to 30 GHz achieving several octave bandwidth for several types of tapering, as shown in Fig. 61. Fig. 62 (b)

shows the measured *S*-parameters of the circularly tapered transition with a radius *R* of 7.6 mm. The widths of 50 Ω lines are 0.94 mm on double-sided parallel-strip line and 0.56 mm on microstrip line.

When the input impedance at a transition varies as a function of frequency, the transition has the limited bandwidth. However, in these transitions, the line impedance at any points of the line is almost the same (50 Ω). Ideally, these transitions should be frequency independent. The differences in *S*-parameter measurements are mainly due to the small discontinuities of electromagnetic fields at the transitions determined by how the tapered ground strip is smooth. As Fig. 62 (a) shows, the circularly tapered transition gives a slightly better performance due to its structural smoothness. The measured *S*-parameters of a microstrip line of the same length (50 mm) are also shown for comparison in Fig. 62 (b). From the results, the insertion loss is less than 1 dB for a back-to-back microstrip to parallel-strip transition. For a single transition, it is less than 0.5 dB. Other losses are due to the transmission line and two coaxial-to-microstrip connectors.

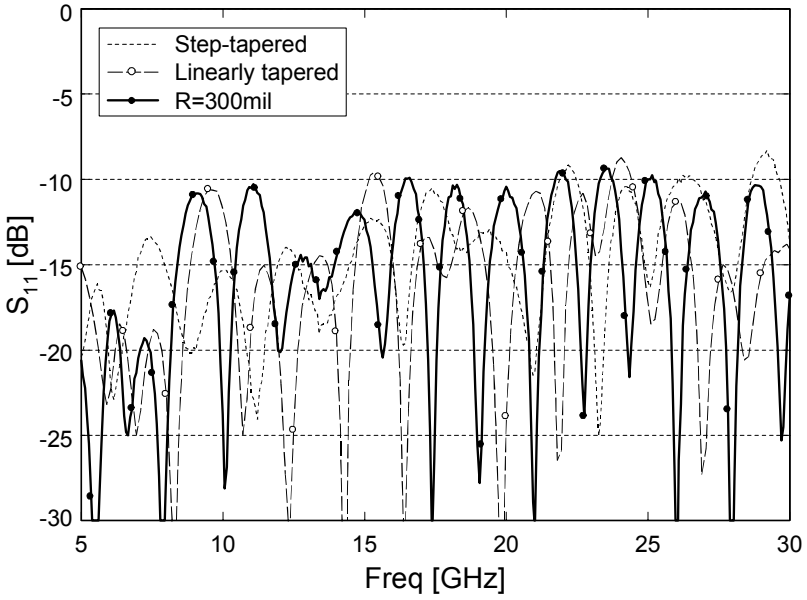

(a)

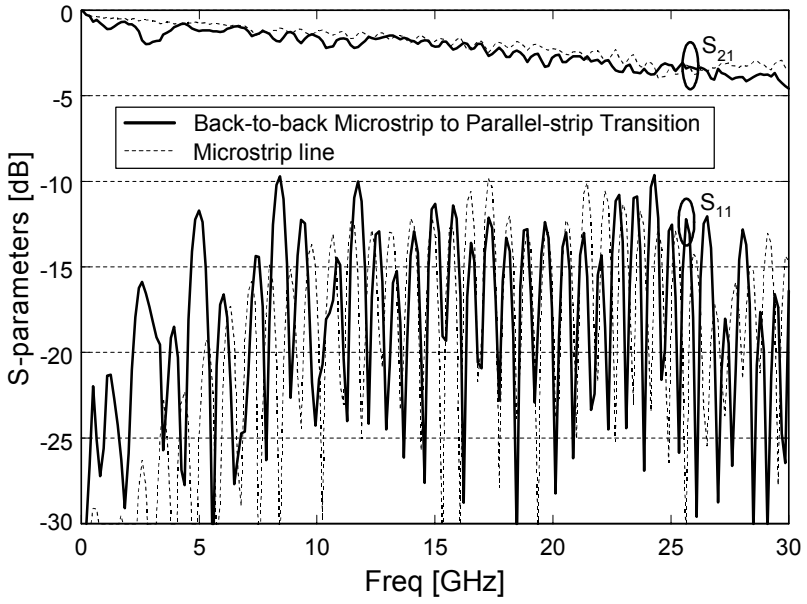

(b)

Fig. 62. Measured *S*-parameters of the back-to-back transition from microstrip line to double-sided parallel-strip line fabricated on the substrate of; (a) RT/Duroid 5880 (ε_r=2.2, h=0.787 mm), (b) RT/Duroid 6010.2 (ε_r=10.2, h=0.635 mm, R=7.62 mm).

4. Bandpass filter using double-sided parallel-strip line

The schematic of a double-sided parallel-strip bandpass filter is shown in Fig. 63 (a). The circuit has the same structure on the upper and bottom sides of the substrate. The filter consists of five sections of parallel stubs spaced 0.25 λ_g apart where λ_g is the guided wavelength of the double-sided parallel-strip line at the center frequency of the bandpass filter [73]. The dimensions of the circuit elements in the bandpass filter are as follows: 1) the width of the stub line W_1 = 0.25 mm; 2) the length of the stub L_1 = 10.7 mm; 3) the spacing of the stubs L_2 = 5.33 mm; 4) the width of the 50 Ω thru-line W_2 = 0.94 mm. The substrate used is an RT/Duroid 6010.2 with a dielectric constant of 10.2 and thickness of 0.635 mm.

In order to investigate the performance of the circuit, a transmission-line model is used. Fig. 63 (b) shows the equivalent circuit of the designed filter. The admittance looking into the stub Y_t is given simply as

$$Y_t = jY_{os}\tan(\beta_1 L_1) \tag{16}$$

where Y_{os} and β_1 are the characteristic admittance of the stub line and the propagation constant, respectively. The *ABCD* matrix of the single parallel stub section shown in Fig. 63 (b) is expressed as

$$\begin{bmatrix} \cos\beta l & jZ_o\sin\beta l \\ jY_o\sin\beta l & \cos\beta l \end{bmatrix}\begin{bmatrix} 1 & 0 \\ 2Y_t & 1 \end{bmatrix}\begin{bmatrix} \cos\beta l & jZ_o\sin\beta l \\ jY_o\sin\beta l & \cos\beta l \end{bmatrix}. \tag{17}$$

Y_o is the characteristic admittance of the 50 Ω thru-line and l is 0.125 λg. The frequency response of the filter can be obtained from the matrix manipulation for five parallel stub sections using *Y*-, *ABCD*-, and *S*-parameter calculations. Two circularly

tapered microstrip to parallel-strip transitions (introduced in the section 3) are used to facilitate the measurements. One transition is placed on the left side and the other on the right side of the filter shown in Fig. 63 (a). The measured and calculated *S*-parameters are shown in Fig. 63 (c). The discrepancies between the measured and calculated results for the filter are attributed to the zero-loss assumption in the transmission-line model, the dispersion, and coupling between the sections.

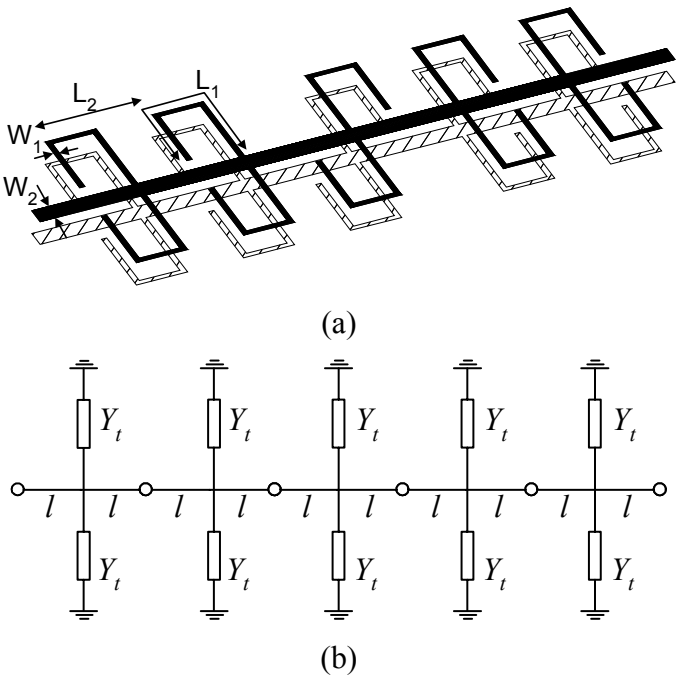

Fig. 63. Double-sided parallel-strip bandpass filter; (a) geometry, (b) equivalent circuit, (c) measured/simulated *S*-parameters.

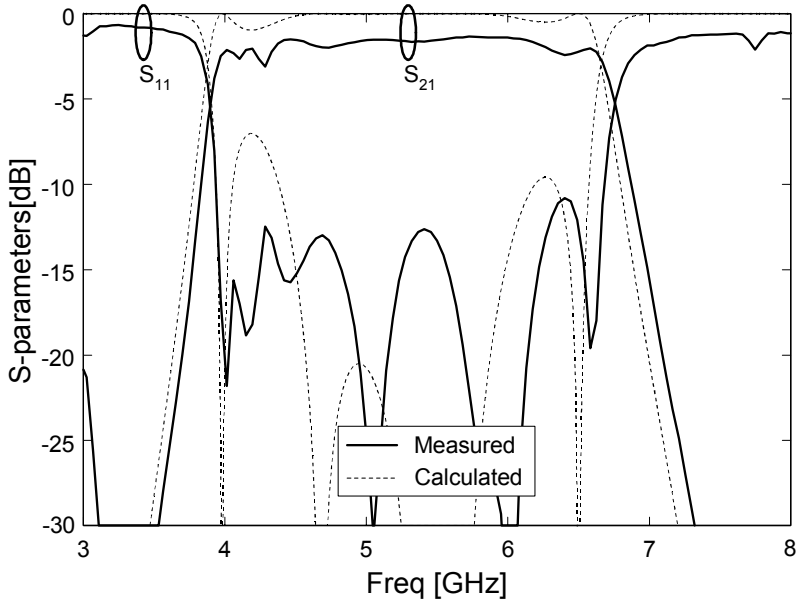

(c)

Fig. 63. Continued.

5. Stepped-impedance lowpass filter using double-sided parallel-strip line

A stepped-impedance lowpass filter is designed using double-sided parallel-strip line with a low impedance line of 10 Ω and high impedance line of 100 Ω. The lowpass filter is designed to give the maximally flat response using the insertion-loss method explained in [60]. The cutoff frequency is 2 GHz. An RT/Duroid 5880 substrate with a dielectric constant of 2.2 and thickness of 0.788 mm is used to fabricate the filter. Fig. 64 (a) shows the filter configuration. The line lengths ($L_3 \sim L_8$) of the stepped impedance lines are 1.68, 8.33, 6.3, 11.38, 4.57, and 3.05 mm, respectively. The corresponding line widths ($W_3 \sim W_5$) of 10, 50, and 100 Ω are 18.29, 3, and 0.627 mm, respectively. The measured results show the stopband suppression level of 17 dB at 2.5 GHz, and are

matched well with the results simulated using IE3D, as shown in Fig. 64 (b). It would be difficult to design a stepped-impedance lowpass filter using low impedance line on CPS due to the required narrow strip and slot widths.

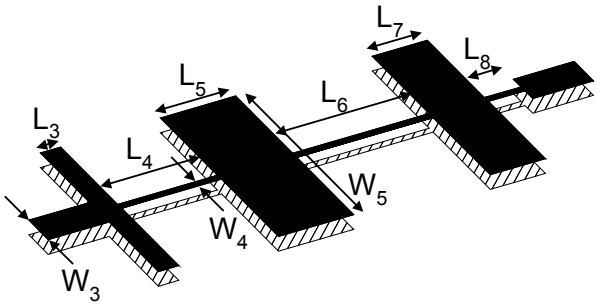

(a)

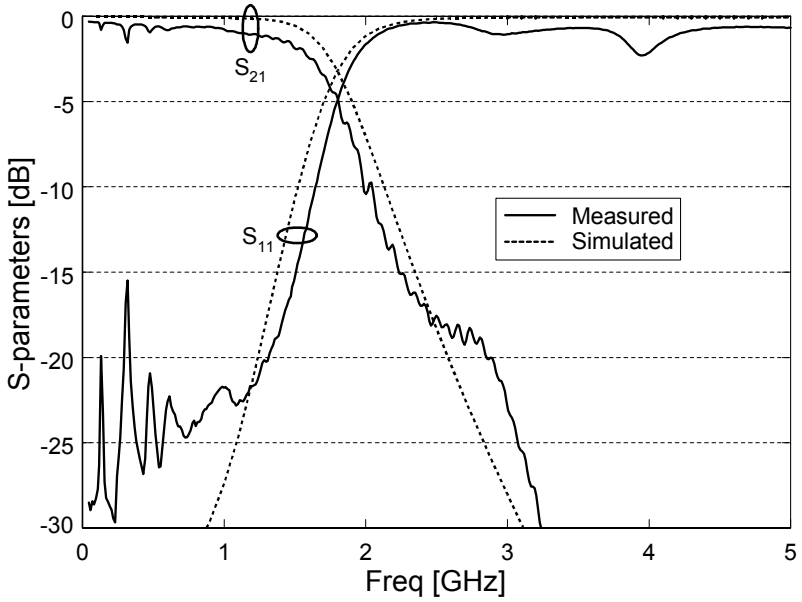

(b)

Fig. 64. Double-sided parallel-strip lowpass filter; (a) geometry, (b) measured/simulated *S*-parameters.

6. Rat-race hybrid coupler using double-sided parallel-strip line

As shown in the schematic of Fig. 65(a), the double-sided rat-race hybrid consists of the symmetrical ring structures on the upper and bottom sides of the substrate. The rat-race hybrid is fabricated on an RT/Duroid 5880 substrate with a dielectric constant of 2.2 and thickness of 0.787 mm. The characteristic impedances of the feed line and ring are 50 Ω and 70.7 Ω, respectively. The line widths of those characteristic impedances are 3 and 2.96 mm, respectively. The circumference of the ring is 1.5 λ_g, where λ_g is the guided wavelength of a parallel-strip line at 5 GHz. Four ports are separated by the angular rotation of 60°. Fig. 65(b) shows the measured *S*-parameters with the results simulated using IE3D. A maximum amplitude imbalance of 3 dB (in S_{41} and S_{21}) is achieved from 3.7 to 6.2 GHz. The maximum phase imbalance of ±10° from the original phase difference of 180° is maintained in this frequency range. The *S*-parameters of a symmetrical four-port network, such as a rat-race coupler, can also be simply calculated using the even-odd-mode analysis technique [74].

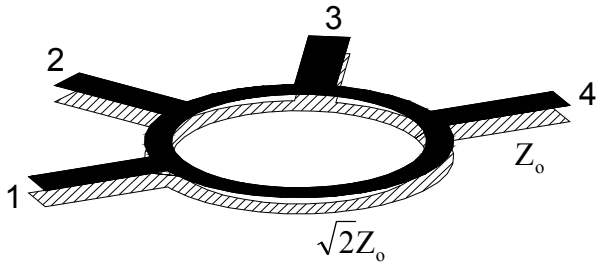

(a)

Fig. 65. Double-sided parallel-strip rat-race hybrid coupler; (a) geometry, (b) measured/simulated *S*-parameters.

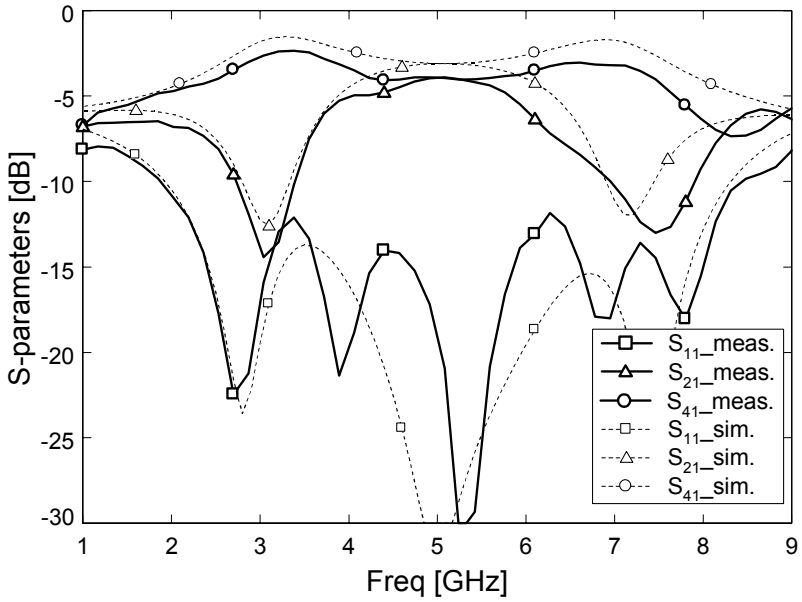

(b)

Fig. 65. Continued.

7. Conclusions

Ultra wideband baluns from microstrip line to double-sided parallel-strip line have been designed and measured. The measured return loss of the tapered transitions shows better than 10 dB from 1 to 30 GHz. Balanced bandpass filter, lowpass filter, and rat-race hybrid coupler using double-sided parallel-strip line have also been designed successfully with good performance. Double-sided parallel-strip lines can have many applications in balanced microwave circuits.

CHAPTER VII

WIDEBAND LOW-COST PHASED ARRAY RADAR

1. Introduction

Rapid progress in telecommunication and radar technology is placing increasing demands on wireless system performance and functionality. Personal communication systems, for example, can now accommodate multiple functions and protocols (e.g., GPS, UMTS, PCS) within a single RF front end. A parallel process of convergence is preparing to take place within the military arena. Modern naval and aerospace vehicles are required to provide a large and increasing number of sensing functions, leading to a proliferation in the number of onboard phased arrays and radar systems. To combat this problem, current research programs seek to integrate multiple systems and functions operating in different frequency bands into a single wideband system [75].

Although broadband phased array systems are a longstanding topic of interest [76], progress has recently been made using wideband tapered slot antennas together with true-time delay phase shifters [58, 77, 78]. In [58], a low-cost four-channel 10-21 GHz phased array transceiver was demonstrated for communications applications.

In this research, extremely wideband phased arrays are demonstrated as an enabling technology for low-cost multi-band and multifunction radar systems. Two designs are used, one operating at 3-12 GHz band and the other at 8-20 GHz band. The designs use antipodal exponentially-tapered slot antennas (ATSAs) in a novel mirrored

array architecture to achieve wideband performance and low cross-polarization. Beam steering is achieved across the complete operating bandwidth using low-cost piezoelectric transducer (PET)-controlled phase shifters. A broadband monolithic microwave integrated circuit (MMIC) power amplifier (PA) is integrated into this design in order to address the traditional challenge of broadband microwave power generation. This PA operates over the 2-20 GHz decade band with more than 29 dBm of output power and 15.8 dB of gain.

System tests demonstrating pulse-radar target ranging and phased-array beam steering are performed with excellent results for each array design. This approach is scalable in size and function for application to a variety of systems, with extended bandwidth and reduced cost in comparison with the state-of-the-art. These results are accordingly expected to stimulate further advances in microwave front-end designs for multifunction RF phased arrays and radars.

2. Antenna, array, and phase shifter

This section describes the design of the antenna elements, phase shifters, and antenna arrays to cover 8-20 GHz band. These components are illustrated in the photograph shown in Fig. 66. The key components are a 1×4 *H*-plane array of ATSAs and a multi-line PET-controlled phase shifter. In addition, there is a 1×4 wideband Chebyshev power divider. These components are inexpensive, can be easily operated over wide bandwidths, and can be scaled depending on the requirements of the design. As an antenna element, Type A antenna, explained in Chapter 5, is used to fabricate the

antenna array to cover 8 to 20 GHz. The array spacing is chosen as 9.4 mm, corresponding to 0.25 λ_o at 8 GHz and 0.63 λ_o at 20 GHz, to prevent grating lobe formation when the beam is steered in the *H*-plane. In addition, the ATSA elements are combined using a new "mirrored" array architecture.

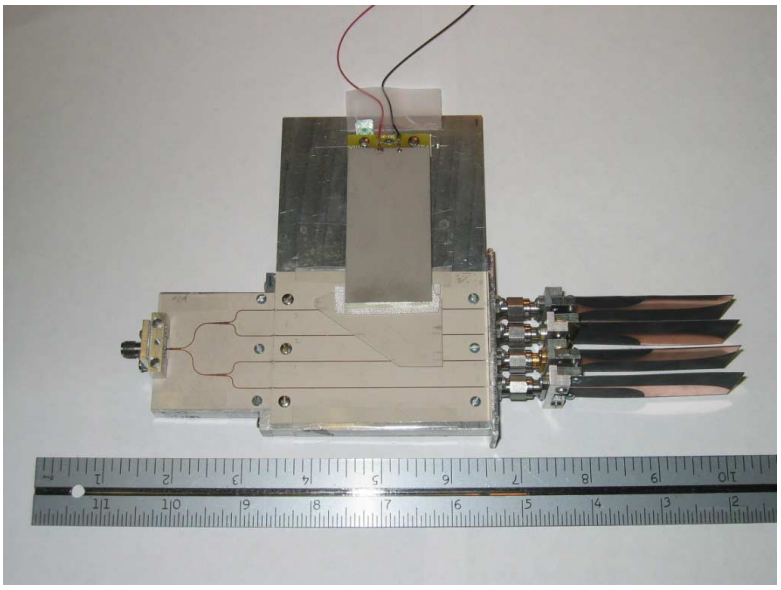

Fig. 66. Configuration of a 1×4 *H*-plane array operated by a PET-controlled phase shifter.

A PET-controlled phase shifter is designed to steer the beam. This phase shifter provides a true time delay (TTD) phase shift capable of linear operation over a wide range of frequencies. The phase shifter is fabricated on an RT/Duroid 6010.2 (ε_r=10.2) with the thickness of 0.38 mm. A TMM10 with a dielectric constant of 9.2 and thickness of 1.27 mm is used as the dielectric perturber for the phase shifter. The incremental length of the perturber over the microstrip line is 15 mm, and the voltage applied to steer

the beam varies from 0 to 60 V. The maximum progressive phase shift of 100° at 20 GHz is designed to achieve the scan angles of 30°.

Fig. 67 shows the measured *S*-parameters and differential phase shifts for the 8-20 GHz design. The return loss is better than 10 dB for the operating frequency ranges, and the insertion loss is less than 4 dB at 20 GHz with full perturbation. This insertion loss includes the losses due to the connectors and line lengths. Fig. 68 shows the steered beam patterns measured from 8-20 GHz. Each beam is steered about 30° away from the broadside in the *H*-plane.

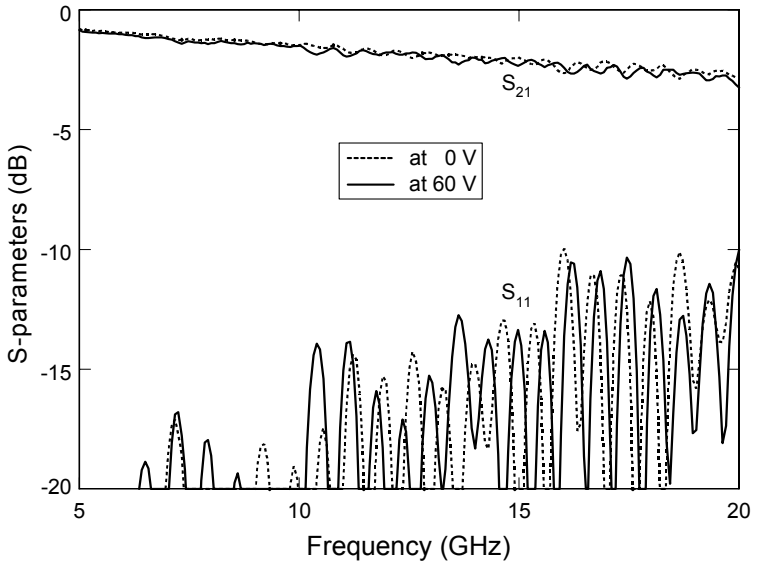

(a)

Fig. 67. Measured performance of the phase shifter operating from 8-20 GHz; (a) *S*-parameters, (b) differential phase shift.

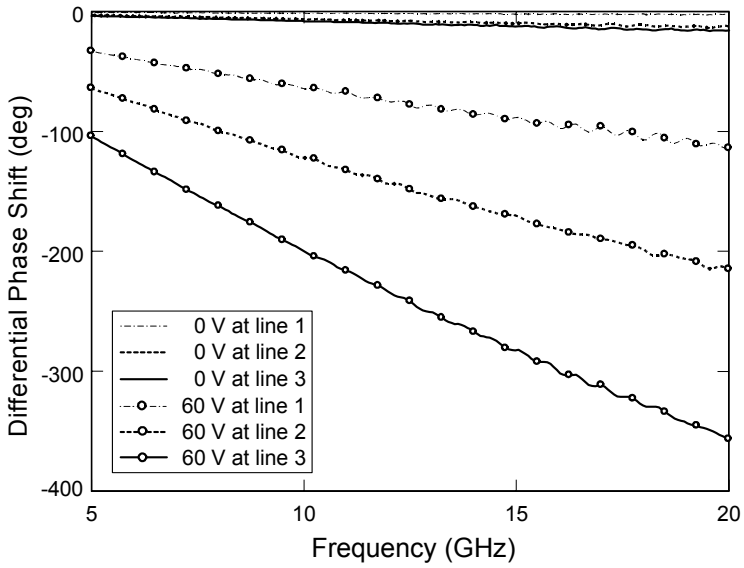

(b)

Fig. 67. Continued.

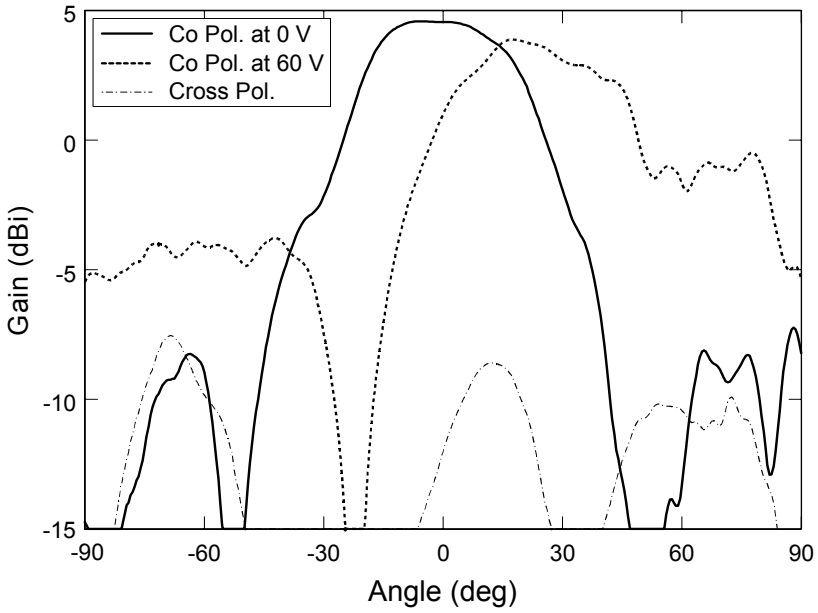

(a)

Fig. 68. Measured beam steering patterns at; (a) 8 GHz, (b) 16 GHz, and (c) 20 GHz.

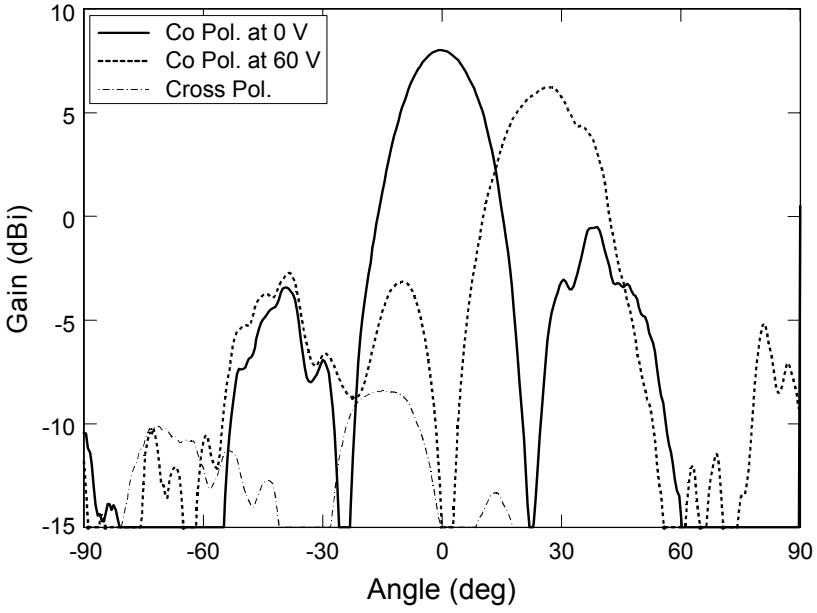

(b)

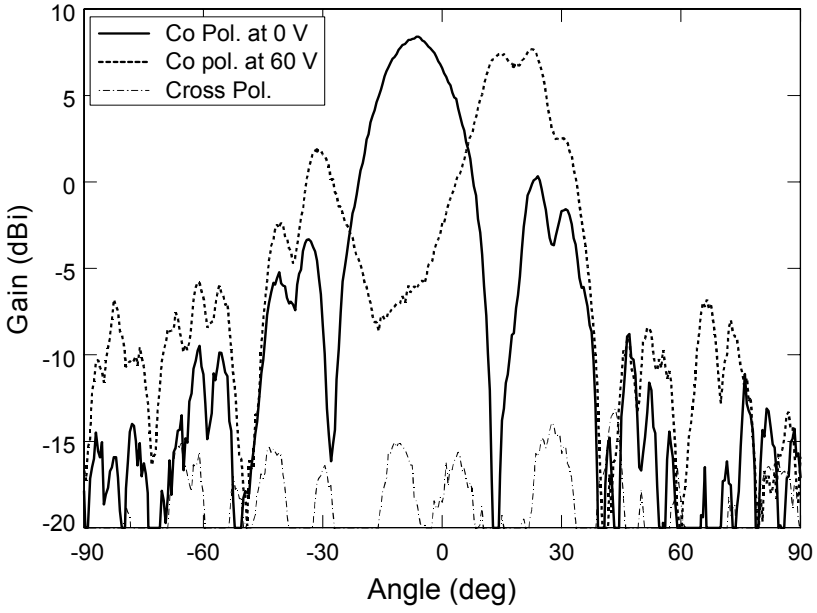

(c)

Fig. 68. Continued.

The other phased array is designed to cover 3-12 GHz band using the same technique explained above. The design parameters of the 3-12 GHz phased array is described in Table 4.

Table 4. The design parameters of the 3-12 GHz phased array

Design parameter	Dimension
Dielectric constant of the antenna substrate, ε_r	2.33
Thickness of the antenna substrate [mm]	0.79
Slot length of the antenna: l [mm]	130
Edge width: d [mm]	15
Slot width: w [mm]	80
Substrate dielectric constant of the phase shifter, ε_r	2.2
Substrate thickness of the phase shifter [mm]	0.38
Perturber dielectric constant of the phase shifter, ε_r	10.2
Perturber thickness of the phase shifter [mm]	1.27
Incremental length of the perturber over the microstrip line, ΔL [mm]	17

3. 2-20 GHz MMIC-based amplifiers

The goal of this research is to demonstrate low-cost, extremely wideband phased arrays for pulse radar applications. Such a demonstration would not be possible, however, without a wideband broadband power amplifier (PA) for the transmitter and low-noise amplifier (LNA) for the receiver. To meet this need, a 2-20 GHz MMIC-based LNA and PA are assembled and incorporated within the system. Fig. 69 illustrates the method of integration. Each MMIC amplifier is solder-mounted on a gold/nickel-plated copper-molybdenum carrier. The copper-molybdenum alloy matches the thermal coefficient of expansion for gallium arsenide and provides thermal dissipation for the MMIC; the gold has low resistance to minimize ohmic loss in the ground path; the

nickel makes it possible to solder to the carrier. Alumina thin-film networks (TFNs) provide 50-Ω lines at the input and output of the MMIC and dc bias pads for the bias wires. External bias capacitors are placed between the bias pads and MMIC, with care taken to minimize bondwire lengths in order to ensure low-frequency stability. The capacitors and TFNs are mounted on the carrier using conductive epoxy, and 1-mil gold wire is used for all RF connections between the MMICs and the off-chip components.

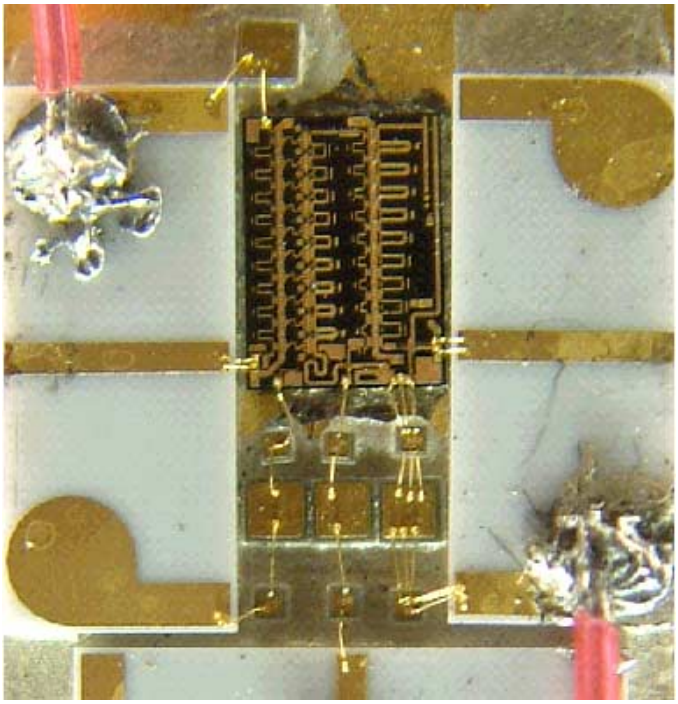

Fig. 69. The photograph of the assembled PA module including the TGA2509 MMIC, the 50-Ω lines at the input and output, and the bias networks.

LNA MMICs covering the 2-20 GHz decade band are currently widely available from multiple vendors. In this system, two Velocium ALH102C LNA chips are used to build up the receive LNA for the radar. Across the 2-20 GHz band, gain of each device

varies from 8 to 12 dB, and noise figure varies from 2 to 4 dB. The power dissipation totals 220 mW for both chips.

High-power MMIC amplifiers operating at 2-20 GHz band have only recently begun to enter the commercial market. This system uses the TriQuint TGA2509 MMIC power amplifier. This chip provides over 29 dBm of power with at least 15.8 dB gain across the 2-20 GHz band, performance that surpasses previously published results for amplifiers of this class [79-81]. The layout of the chip is included in Fig. 69. The chip size is 7.5 mm^2. The first stage of this distributed amplifier utilizes cascode cells to enhance the gain while providing an option for automatic gain control. The second stage utilizes common source cells to provide high output power over the entire band. Both stages employ capacitive division on each cell to extend the upper band edge to 20 GHz. Gate bias is provided through the gate termination resistor, while the drain bias is provided through an on-chip low-pass network. The drain voltage is 12 V, and total power consumption is 13.2 W. As illustrated in Fig. 70, small-signal gain exceeds 15.8 dB and saturation power exceeds 29 dBm over the entire 2-20 GHz band.

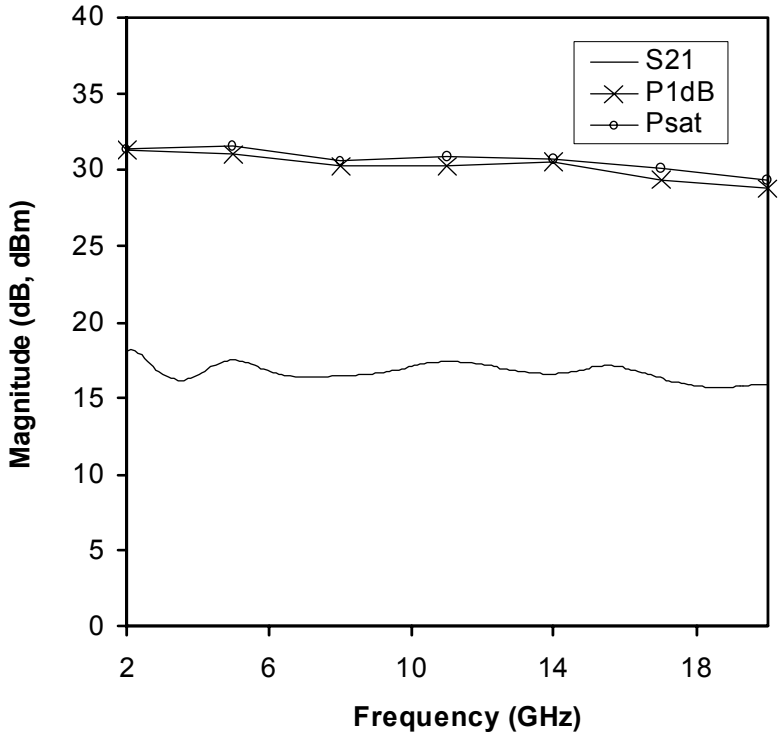

Fig. 70. Gain and output power of the PA MMIC versus frequency.

4. System test

For system-level measurements, the PET-controlled antenna arrays are incorporated with the MMIC-based amplifier modules and tested using the setup shown in Fig. 71. A pulse-modulated synthesized source feeds an HP 8349B wideband driver amplifier that in turn feeds the 2-20 GHz PA module. The PA drives the PET-controlled phased array previously shown in Fig. 66. An identical PET-controlled array is used for the receiver so that both phased arrays can be controlled using the same bias voltage. Alternatively, a single antenna array can be used with the addition of a wideband duplexer switch. The receiving phased array feeds the 2-20 GHz LNA module, which in

turn feeds an HP8472B Schottky diode detector and an IF amplifier. The detected waveform is compared with a timing signal to determine target range.

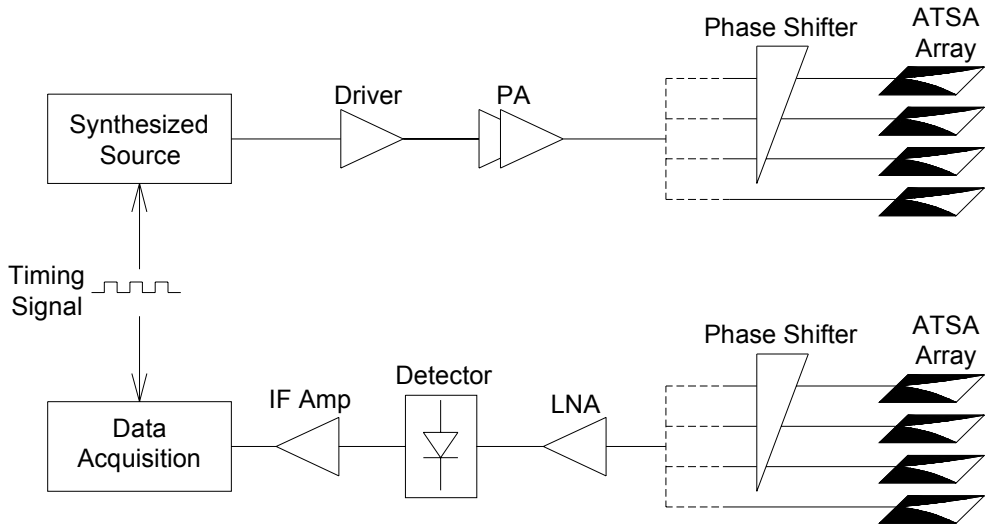

Fig. 71. System block diagram illustrating the test setup for the beam-steerable pulse radar.

A movable 1×1 m aluminum reflector serves as the target. The transmitter projects a pulse-modulated signal onto the target, and the receiver picks up the return signal. The distance between the target and the radar is varied, and the radar detects the variation in this distance by measuring the time delay between the received signal and the timing signal. The results presented in this research use an RF transmit signal that is pulse modulated at a pulse-repetition frequency (PRF) of 20 MHz and at a duty cycle of 10 %. All measurements are taken inside a 30-foot indoor range.

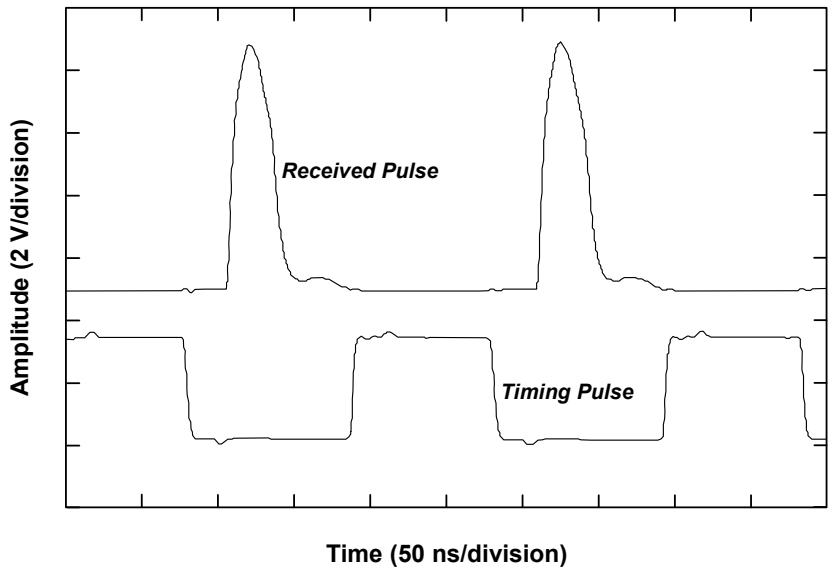

Fig. 72. The detected waveform of the received signal can be compared with the waveform of the timing signal in order to measure target range.

Fig. 72 shows an example of a received pulse waveform and timing reference signal. The measurement shown in this figure uses a transmit signal at 5.8 GHz to range a target located 175 inches away from the 3-12 GHz radar system. Ranging tests are conducted at 5.8 GHz for the 3-12 GHz array and at 14 GHz for the 8-20 GHz. As shown in Fig. 73, the measured and expected time delays agree very well. The average error is ±0.14° at 5.8 GHz and ±0.13° at 14 GHz, which corresponds to an average error of about ±0.8 inches at both frequencies.

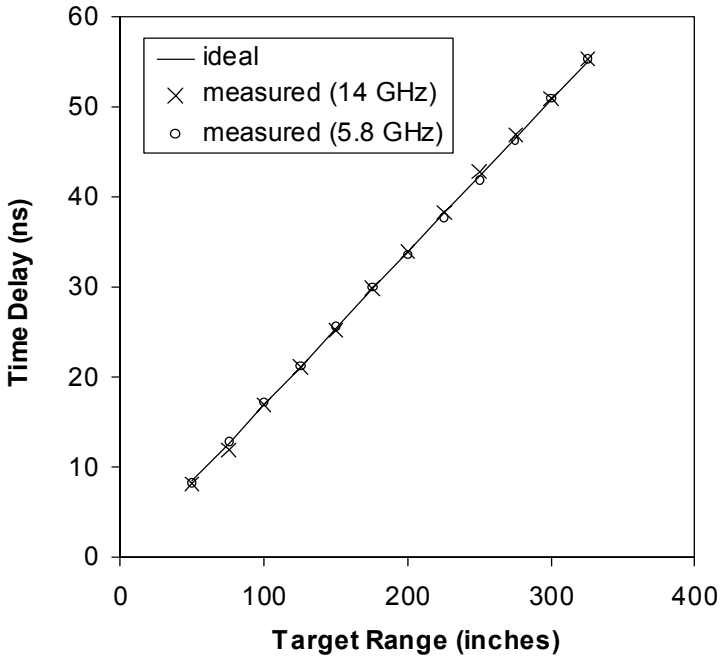

Fig. 73. Comparison between measured and ideal time delays for varying target ranges.

Target position can be determined by varying the beam steering angle. The maximum external bias voltage to the PET phase shifters is 60 V. Cross-polarization is less than 17 dB below the co-polarization. This excellent linear polarization is due to the mirrored array approach described in Chapter V, which reduces cross-polarization levels by more than 20 dB at 20 GHz. Imperfections in the measured patterns are due to multiple factors: the incomplete progression in the phase shifts, the phase mismatches in the connection points between the phase shifter and the antennas, imperfect flatness in the antenna elements, and reflections from the circuit elements. The radiation patterns, nonetheless, can be further improved by an additional optimization process or by finer fabrication tolerances. Finally, effective isotropic radiated power (EIRP) varies

approximately from 35-38 dBm over the 8-20 GHz range.

5. Conclusions

Multiple radar systems can be consolidated within a single multifunction phased array radar system. This research has demonstrated an inexpensive approach for producing such a system using cross-polarization suppressed ATSA arrays, piezoelectric true-time-delay phase shifters, and decade bandwidth 1-W monolithic power amplifiers. The technology is inherently scalable to larger arrays and should have wide-ranging impact on wideband multifunction radar design.

CHAPTER VIII

SUMMARY AND RECOMMENDATIONS

1. Summary

In this dissertation, piezoelectric transducer (PET)-controlled devices and beam steering schemes using PETs have been developed to achieve better performance with novel ideas. As new transmission lines, double-sided parallel-strip lines and ultra wideband transitions have been introduced and several balanced microwave circuits using parallel-strip lines have been designed and measured.

A multi-line phase shifter controlled by PET enables the design of a phased array with many advantages: low-cost, low-loss, wideband performance, no matching circuit required, high power handling, low power consumption, and easy fabrication. However, several disadvantages have also been reported: alignment difficulty, high bias voltage, slow response time, and hysteresis phenomena [82]. PET-controlled devices use electronically perturbed transmission lines. The perturbation is controlled by the small movement achieved using PET.

In Chapter II, PET-controlled devices for microwave applications have been developed. An increased phase shift has been achieved using a PET-controlled perturbation on coplanar waveguide (CPW), rather than on microstrip. The electromagnetic fields on CPWs are less confined than those on microstrip lines, thereby making them more sensitive to perturbers placed above the guide. As other applications,

novel dielectric perturbation and frequency tuning techniques using PET have been introduced to design a low-loss QPSK modulator and a frequency agile slot dipole. The resonant frequency of a slot dipole is shifted by varying the effective dielectric constant of the slot using an external dielectric perturbation. This technique thus provides the ability to change the resonant or operating frequency.

In Chapter III, a dual beam phased array and a monopulse antenna using bi-directionally-fed microstrip patch array have been discussed. An independently controllable dual beam phased array with the same polarization has been designed. A single or dual beam is synthesized by controlling the phases on both sides of the series-connected microstrip patch array. Two beams having the same polarization are obtained by feeding both sides of four series fed 1×8 microstrip patch antenna arrays, and each beam is steered in the *H*-plane using a PET-controlled phase shifter. Additionally, a simple-structured bi-directionally-fed microstrip patch array has been designed to achieve a sum/difference pattern. A sum/difference pattern with an excellent front-to-back ratio and low cross-polarization levels is realized by adjusting the phases of the input signals to both sides of a bi-directionally-fed microstrip array.

In Chapter IV, a multiple beam phased array has been demonstrated. Numerous techniques have been reported to generate multiple beams. Typical techniques include lens-based beamformers such as Ruze, Rotman, and R-KR, as well as circuit-based beamformers including Blass and Butler matrix. A simple and low-cost multiple beam phased array to overcome the drawback of the switched beam antenna array has been designed using a microstrip Rotman lens and a PET-controlled phase shifter. A

microstrip Rotman lens with five beam ports and nine array ports is used as a feed for a multiple beam antenna to make the scan angle of 0°, ±15°, and ±30° at *Ka*-band. Using two PET-controlled phase shifters, the five beams are steered ±8° completely covering ±38° from the broadside.

In Chapter V, wideband antenna arrays and novel beam scanning schemes have been introduced. Vivaldi-type antennas are commonly used to achieve wideband performance. However, a balun is necessary to feed the antenna, and the bandwidth is limited by the transition performance. Very wideband performance can be achieved using an antipodal tapered slot antenna because of its inherently simple wideband transition from microstrip line to parallel-strip line. An antipodal exponentially-tapered slot antenna (ATSA) has been designed to cover from 10 to 35 GHz. Low-cost one- and two-dimensional scanning schemes have been demonstrated using ATSA arrays and PET-controlled phase shifters. A 4×4 ATSA array is designed for two-dimensional scanning, and the beam is steered using two sets of PET-controlled phase shifters. One set consisting of four identical PET-controlled phase shifters is used to steer the beam in the *E*-plane, and the other is used for the *H*-plane. Using two sets of PET-controlled phase shifters, the beam is steered over 30° in both planes. 1×4 *E*- and *H*-plane arrays are also designed for one-dimensional scanning.

In Chapter VI, double-sided parallel-strip lines as balanced lines have been demonstrated to realize very wideband transitions from microstrip lines and balanced circuits. As a balanced line, the parallel-strip line makes it possible to realize a low impedance line. It also allows the design of compact wideband baluns and junctions.

Wideband transitions (or baluns) from parallel-strip line to microstrip line, a typical unbalanced transmission line, have been realized to cover several octave bandwidth, and several microwave circuits including a bandpass filter, a lowpass filter, and a rat-race hybrid have been designed as examples of new balanced circuits using parallel-strip lines.

In Chapter VII, a wideband low-cost phased array radar has been developed. The radar system operates using a modulated pulse over the 3 to 20 GHz band, and consists of PET-controlled phase shifters, microwave monolithic integrated circuits (MMIC) of power amplifier and low noise amplifier, and ATSA arrays. The accurate average error of ±0.13° at 14 GHz was achieved in target ranging test.

2. Recommendations for future research

Further circuit optimization and developments are suggested for the future. Using the inherent wideband capability of a PET-controlled phase shifter, a wideband phased array system covering many channels can be designed. An antipodal tapered slot antenna may be designed to cover a bandwidth of more than two octaves in two-dimensional array. This technique can be further developed for wideband two-dimensional scanning. In Chapter III, a one-dimensional monopulse antenna has been developed. This monopulse antenna aray can be expanded in two-dimensions.

REFERENCES

[1] T.-Y. Yun and K. Chang, "Analysis and optimization of a phase shifter controlled by a piezoelectric transducer." *IEEE Trans*. *Microwave Theory Tech*., vol. 50, no. 1, pp. 105-111, Jan. 2002.

[2] J. J. Lee, "Lens antennas," In *Handbook of Microwave and Optical Components,* vol. 1, K. Chang, ed. New York: Wiley, 1989, pp. 595-626.

[3] B. Schoenlinner, X. Wu, J. P. Ebling, G. V. Eleftheriades, and G. M. Rebeiz, "Wide-scan spherical-lens antennas for automotive radars," *IEEE Trans*. *Microwave Theory Tech*., vol. 50, no. 9, pp. 2166-2175, Sept. 2002.

[4] D. H. Archer, "Lens-fed multiple beam arrays," *Microwave Journal*, vol. 27, pp. 171-195, Sept. 1984.

[5] J. P. Shelton, "Focusing characteristics of symmetrically configured bootlace lenses," *IEEE Trans. Antennas Propagat.*, vol. 26, no. 4, pp. 513-518, July 1978.

[6] T. Katagi, S. Mano, and S. I. Sato, "An improved design method of Rotman lens antennas," *IEEE Trans. Antennas Propagat.*, vol. 32, no. 5, pp. 524-527, May 1984.

[7] W. Rotman and R. F. Turner, "Wide-angle microwave lens for line source applications," *IEEE Trans. Antennas Propagat.*, vol. 11, no. 6, pp. 623-632, Nov. 1963.

[8] R. C. Hansen, "Design trades for Rotman lenses," *IEEE Trans. Antennas Propagat.*, vol. 39, no. 4, pp. 464-472, Apr. 1991.

[9] Y. M. Tao and G. Y. Delisle, "Lens-fed multiple beam array for millimeter wave indoor communications," in *IEEE Antennas Propagat. Soc. Int. Symp.*, Montreal, Canada, July 1997, vol. 4, pp. 2206-2209.

[10] J. Kim and F. Barnes, "Scaling and focusing of the Rotman lens," in *IEEE Antennas Propagat. Soc. Int. Symp.*, Boston, MA, July 1997, vol. 2, pp. 773-776.

[11] M. E. Russell, A. Crain, A. Curran, R. A. Campbell, C. A. Drubin, and W. F. Miccioli, "Millimeter-wave radar sensor for automotive intelligent cruise control," *IEEE Trans*. *Microwave Theory Tech*., vol. 45, no. 12, pp. 2444-2453, Dec. 1997.

[12] J. Lee, J. Lee, and H. Tae, "Design of a nonradiative dielectric Rotman lens in the millimeter wave frequency," in *IEEE MTT-S Int. Microwave Symp. Dig*., Phoenix, AZ, May 2001, vol. 1, pp. 551-554.

[13] K. K. Chan, W. B. Wallace, and R. R. Blasing, "Design of a broadband and wide scan angle Rotman lens," in *IEEE Antennas Propagat. Soc. Int. Symp.*, Dallas, TX, May 1990, pp. 988-991.

[14] A. F. Peterson and E. O. Rausch, "Scattering matrix integral equation analysis for the design of a waveguide Rotman lens," *IEEE Trans. Antennas Propagat.*, vol. 47, no. 5, pp. 870-878, Apr. 1999.

[15] L. Musa and M. S. Smith, "Microstrip port design and sidewall absorption for printed Rotman lenses," *IEE Proc. Microwaves, Antennas and Propagation*, pt. H, vol. 136, no. 1, pp. 53-58, Feb. 1989.

[16] P. S. Hall and S. J. Vetterlein, "Review of radio frequency beamforming techniques for scanned and multiple beam antennas," *IEE Proc. Microwaves, Antennas and Propagation*, pt. H, vol. 137, no. 5, pp. 293-303, Oct. 1990.

[17] J. R. James and P. S. Hall, *Handbook of Microstrip Antennas*. London, U.K.: Peter Peregrinus, 1989.

[18] P.J. Gibson, "The Vivaldi aerial," in *Proc. 9th Eur. Microwave Conf*., Brighton, U.K., June 1979, pp. 101-105.

[19] K. S. Yngvesson, D. H. Schaubert, T. L. Korzeniowski, E. L. Kollberg, T. Thungren, and J. F. Johansson, "Endfire tapered slot antennas on dielectric substrates," *IEEE Trans. Antennas Propagat*., vol. 33, pp. 1392-1400, Dec. 1985.

[20] E. Gazit, "Improved design of the Vivaldi antenna," *IEE Proc. Microwaves,*

Antennas and Propagation, vol. 135, pp. 89-92, Apr. 1988.

[21] J. Langley, P. Hall, and P. Newham, "Balanced antipodal Vivaldi antenna for wide bandwidth phased arrays," *IEE Proc. Microwaves, Antennas and Propagation*, vol. 143, pp. 97-102, Apr. 1996.

[22] K. S. Yngvesson, T. L. Korzeniowski, Y.-S. Kim, E. L. Kollberg, and J. F. Johansson, "The tapered slot antenna – a new integrated element for millimeter-wave applications," *IEEE Trans. Microwave Theory Tech.*, vol. 37, pp. 365-374, Feb. 1989.

[23] T.-H. Chio and D. H. Schaubert, "Parameter study and design of wide-band widescan dual-polarized tapered slot antenna arrays," *IEEE Trans. Antennas Propagat*., vol. 48, pp. 879-886, June 2000.

[24] S. Sugawara, Y. Maita, K. Adachi, K. Mori, and K. Mizuno, "A mm-wave tapered slot antenna with improved radiation pattern," in *IEEE-MTT Int. Symp.*, Denver, CO, June 1997, pp. 959-962.

[25] N. Fourikis, N. Lioutas, and N. V. Shuley, "Parameter study and the co- and crosspolarisation characteristics of tapered planar and antipodal slotline antennas," *IEE Proc. Microwaves, Antennas and Propagation*, vol. 140, pp. 17-22, Feb. 1993.

[26] E. Thiele and A. Taflove, "FD-TD analysis of Vivaldi flared horn antennas and arrays," *IEEE Trans. Antennas Propagat*., vol. 42, pp. 633-641, May 1994.

[27] U. Kotthaus and B. Vowinkel, "Investigation of planar antennas for submillimeter receivers," *IEEE Trans. Microwave Theory Tech.*, vol. 37, pp. 375-380, Feb. 1989.

[28] M. Kragalott, W. R. Pickles, and M. S. Kluskens, "Design of a 5:1 bandwidth stripline notch array from FDTD analysis," *IEEE Trans. Antennas Propagat*., vol. 48, pp. 1733-1740, Nov. 2000.

[29] Y.-H. Suh and K. Chang, "A high-efficiency dual-frequency rectenna for 2.45- and 5.8-GHz wireless power transmission." *IEEE Trans*. *Microwave Theory Tech*., vol.

50, no. 7, pp. 1784-1789, July 2002.

[30] Y.-H. Suh and K. Chang, "Coplanar stripline resonators modeling and applications to filters." *IEEE Trans*. *Microwave Theory Tech*., vol. 50, no. 5, pp. 1289-1296, May 2002.

[31] G. H. Haertling, "Piezoelectric and electrooptic ceramics," In *Ceramic Materials for Electronics*, R. C. Buchanan, ed. New York: Marcel Dekker, 1986, ch. 3.

[32] T.-Y. Yun and K. Chang, "A low-loss time-delay phase shifter controlled by piezoelectric transducer to perturb microstrip line." *IEEE Microwave Guided Wave Letters*, vol. 10, no. 3, pp. 96-98, Mar. 2000.

[33] S.-G. Kim, T.-Y. Yun, and K. Chang, "Time-delay phase shifter controlled by piezoelectric transducer on coplanar waveguide," *IEEE Microwave & Wireless Components Letters*, vol. 13, pp. 19-20, Jan. 2003.

[34] S.-G. Kim and K. Chang, "Simple microwave QPSK modulator using piezoelectric transducers," *IEE Electronics Letters*, vol. 40, pp. 1493-1494, Nov. 2004.

[35] S.-G. Kim and K. Chang, "Frequency tunable CPW-fed slot dipole using a piezoelectric transducer," *IEE Electronics Letters*, vol. 39, pp. 991-992, June 2003.

[36] S.-G. Kim and K. Chang, "Independently controllable dual-feed dual-beam phased array using piezoelectric transducers," *IEEE Antennas & Wireless Propagat. Letters*, vol. 1, pp. 81-83, 2002.

[37] S.-G. Kim and K. Chang, "Low-cost monopulse antenna using bi-directionally-fed microstrip patch array," *IEE Electronics Letters*, vol. 39, pp. 1428-1429, Oct. 2003.

[38] S.-G. Kim and K. Chang, "Piezoelectric transducer controlled multiple beam phased array using microstrip Rotman lens at Ka-band," to appear in *IEEE Microwave & Wireless Components Letters.*

[39] S.-G. Kim and K. Chang, "Ultra wideband 8 to 40 GHz beam scanning phased

array using antipodal exponentially-tapered slot antennas," in *IEEE MTT-S Int. Microwave Symp. Dig*., Fort Worth, TX, June, 2004, vol. 3, pp.1757-1760.

[40] S.-G. Kim and K. Chang, "Ultra wideband exponentially-tapered antipodal Vivaldi antennas," in *IEEE Antennas Propagat. Soc. Int. Symp*., Monterey, CA, June 2004, vol. 3, pp. 2273-2276.

[41] S.-G. Kim and K. Chang, "Ultra wide-band transitions and new microwave components using double-sided parallel-strip lines," *IEEE Trans. Microwave Theory Tech*., vol. 52, no. 9, pp. 2148-2152, Sept. 2004.

[42] K. C. Gupta, R. Garg, I. Bahl, and P. Bhartia, *Microstrip Lines and Slotlines*. 2nd Ed. Norwood, MA: Artech House, 1996, ch. 7.

[43] J. Uher and W. J. R. Hoefer, "Tunable microwave and millimeter-wave band-pass filters," *IEEE Trans. Microwave Theory Tech*., vol. 39, no. 4, pp. 643-653, Apr. 1991.

[44] B. S. Virdee, "Current techniques for tuning dielectric resonators," *Microwave Journal*, pp. 130-138, Oct. 1998.

[45] A.T. Kolsrud, M.-Y. Li, and K. Chang, "Dual-frequency electronically tunable CPW-fed CPS dipole antenna," *IEE Electronics Letters*, vol. 34, pp. 609-611, Apr. 1998.

[46] J.M. Carrere, R. Staraj, and G. Kossiavas, "Small frequency agile antennas," *IEE Electronics Letters*, vol. 37, pp. 728-729, June 2001.

[47] G. Le Ray, M. Himdi, and J.P. Daniel, "Frequency agile slot-fed patch antenna," *IEE Electronics Letters*, vol. 32, pp. 2-3, Jan. 1996.

[48] C. Luxey, L. Dussopt, J.-L. Le Sonn, and J.-M. Laheurte, "Dual-frequency operation of CPW-fed antenna controlled by pin diodes," *IEE Electronics Letters*, vol. 36, pp. 2-3, Jan. 2000.

[49] J.-M. Laheurte, "Switchable CPW-fed slot antenna for multifrequency operation,"

IEE Electronics Letters, vol. 37, pp. 1498-1500, Dec. 2001.

[50] E. G. Magill, and H. A. Wheeler, "Wide-angle impedance matching of a planar array antenna by a dielectric sheet," *IEEE Trans*. *Antennas Propagat*., vol. 14, pp. 49-53, Jan. 1966.

[51] N. K. Das and D. M. Pozar, "PCAAMT – Personal computer aided analysis of multilayer transmission lines", ver. 1.0, Amherst, MA: Univ. of Massachusetts June 1990.

[52] "IE3D," ver. 9.0, Freemont, CA: Zeland Software Inc., Jan. 2002.

[53] R. C. Hansen, *Phased Array Antennas*. New York: John Wiley & Sons, Inc., 1998, ch. 6 and 10.

[54] S. M. Sherman, *Monopulse Principles and Techniques*. Dedham, MA: Artech House, 1984.

[55] C. C. Ling and G. M. Rebeiz, "94 GHz integrated horn monopulse antennas," *IEEE Trans*. *Antennas Propagat*., vol. 40, no. 8, pp. 981-984, Aug. 1992.

[56] S. Lin, Y. Qian, and T. Itoh, "A low noise active integrated antenna receiver for monopulse radar applications," in *Proc. IEEE MTT-S Int*. *Microwave Symp. Dig*., Phoenix, AZ, May 2001, pp1395-1398.

[57] K. Chang, M. Yin, and W. X. Zhang, "Coupled tapered slot-line antenna with sum/difference beams," in *Proc. Asia-Pacific Microwave Conference*, Sydney, Australia, Dec. 2000, pp. 1335-1338.

[58] T.-Y. Yun and K. Chang, "A low-cost 8 to 26.5 GHz phased array antenna using a piezoelectric transducer controlled phased shifter," *IEEE Trans. Antennas Propagat*., vol. 49, no. 9, pp. 1290-1298, Sept. 2001.

[59] T. Metzler, "Microstrip series arrays." *IEEE Trans*. *Antennas Propagat*., vol. 29, no. 1, pp. 174-178, Jan. 1981.

[60] D. M. Pozar, *Microwave Engineering*, 2nd Ed. New York: Wiley, 1998, ch. 5 and 8.

[61] S. Kanamaluru, M. Y. Li, and K. Chang, "Analysis and design of aperture coupled microstrip patch antennas and arrays fed by dielectric image line." *IEEE Trans. Antennas Propagat.*, vol. 44, no. 7, pp. 964-974, July 1996.

[62] T. Katagi, S. Mano, and S. I. Sato, "Comments on corrections to 'An improved design method of Rotman lens antennas,'" *IEEE Trans. Antennas Propagat.*, vol. 43, no. 6, pp. 634, June 1995.

[63] S. Romisch, D. Popovic, N. Shino, R. Lee, and Z. Popovic, "Multi-beam discrete lens arrays with amplitude-controlled steering." in *IEEE MTT-S Int. Microwave Symp. Dig.*, Philadelphia, PA, June 2003, vol. 3, pp. 1669-1672.

[64] W. L. Stutzman and G. A. Thiele, *Antenna Theory and Design*. New York: John Wiley & Sons, Inc., 1998, ch. 3.

[65] "Microwave Studio", ver. 4, Darmstadt, Germany: CST, 2003.

[66] R. Garg, P. Bhartia, I. Hahl, and A. Ittipiboon, *Microstrip Antenna Design Handbook*. Norwood, MA: Artech House, 2001.

[67] M. A. Smith, K. J. Anderson, and A. M. Pavio, "Decade-band mixer covers 3.5 to 35 GHz," *Microwave Journal*, pp. 163-171, Feb. 1986.

[68] H. A. Wheeler, "Transmission-line properties of parallel strips separated by a dielectric sheet," *IEEE Trans. Microwave Theory Tech.*, vol. 12, pp. 172-185, Mar. 1965.

[69] J. M. Rochelle, "Approximations for the symmetrical parallel-strip transmission line," *IEEE Trans. Microwave Theory Tech.*, vol. 23, pp. 712-714, Aug. 1976.

[70] B. Climer, "Analysis of suspended microstrip taper baluns," *IEE Proc. Microwaves, Antennas and Propagation*, Pt. H, vol. 135, no. 2, pp. 65-69, Apr. 1988.

[71] C. Y. Ho, "New analysis techniques builds better baluns," *Microwave & RF*, pp.99-102, 1985.

[72] B. C. Wadell, *Transmission Line Design Handbook*. Norwood, MA: Artech House, 1991.

[73] K. Goverdhanam, R. N. Simons, and L. P. B. Katehi, "Coplanar stripline propagation characteristics and bandpass filter," *IEEE Microwave and Guided Wave Letters*, vol. 7, pp. 214-216, Aug. 1997.

[74] J. Reed and G. J. Wheeler, "A method of analysis of symmetrical four-port networks," *IRE Trans. Microwave Theory Tech*., vol. 4, pp. 246-252, Oct. 1956.

[75] P.F. McManmon, E.A. Watson, and M.T. Eismann, "Suggestions for low cost multifunction sensing," in *Proc. IEEE Aerospace Conf.*, Aspen, CO, March 1998, pp. 283-306.

[76] G.J. Laughlin, E.V. Byron, and T.C. Cheston, "Very wide-band phased-array antenna," *IEEE Trans. Antennas Propagat*., vol. 20, no. 6, pp. 699-704, Nov. 1972.

[77] C. Hemmi, R.T. Dover, F. German, and A. Vespa, "Multifunction wide-band array design," *IEEE Trans. Antennas Propagat*., vol. 47, no. 3, pp. 425-431, Mar. 1999.

[78] K. Trott, B. Cummings, R. Cavener, M. Deluca, J. Biondi, and T. Sikina, "Wideband phased array radiator," in *Proc. IEEE Int. Symp. Phased Array Systems Technology*, Boston, MA, Oct. 2003, pp. 383-386.

[79] K.I. Jeon, J.H. Lee, S.W. Paek, D.W. Kim, W.S. Lee, C.R. Lim, H. Cha, H. Choi, and K.W. Chung, "A 5 to 27 GHz MMIC power amplifier," in *IEEE-MTT Int. Symp*., Boston, MA, June 2000, pp. 541-544.

[80] J.J. Komiak, W. Kong, and K. Nichols, "High efficiency wideband 6 to 18 GHz power amplifier MMIC," in *IEEE-MTT Int. Symp*., Seattle, WA, June 2002, pp. 905-907.

[81] C. Wang, C.T. Rodenbeck, M.R. Coutant, and K. Chang, "A novel broadband T/R module for phased array applications in wireless communications," in *IEEE-MTT Int. Symp*., Seattle, WA, June 2002, pp. 1325-1328.

[82] T.-Y. Yun, "One-dimensional photonic bandgap (PBG) structures and piezoelectric transducer (PET) controlled devices for microwave applications," Ph.D. dissertation, Texas A&M University, College Station, May 2001.

APPENDIX A

DERIVATION OF LENS PARAMETERS [7]

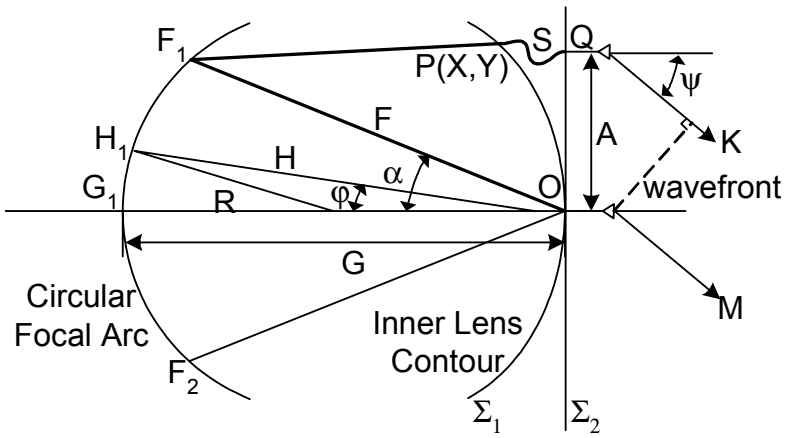

Fig. A1. Microstrip Rotman lens parameters.

In Fig. A1, the lens contours are shown by the curves Σ_1 and Σ_2. The inner contour Σ_1 is determined by the lens equations and locates the position of the probe transitions between the lens and microstrip line to arrays. The outer contour Σ_2 is straight and defines the position of the radiating elements that comprise the line source. Corresponding elements on contours Σ_1 and Σ_2 are connected by microstrip lines. The scan angle ψ is the same as a focal angle in this design.

The contour Σ_1 is defined by the two coordinates (X, Y) that are specified relative to a point O on the central axis of the lens. Elements on the straight contour Σ_2 are similarly determined by the single coordinate A, measured relative to the point O. O lies

on contours Σ_1 and Σ_2, and is connected by a transmission line of electrical length *S*. The point *P*(*X*,*Y*) is connected to a typical element *Q*(*A*) which lies on Σ_2 by the transmission line of electrical length *S*. Since the three parameters *X*, *Y*, and *S* are independent, the straight-front-face lens has three degrees of freedom to be stipulated. These three degrees of freedom are used to obtain wide-angle scanning characteristics by selecting two symmetrical off-axis focal points F_1 and F_2, and one on-axis focal point G_1, having coordinates (-$F\cos\alpha$, $F\sin\alpha$), (-$F\cos\alpha$, $F\sin\alpha$), and (-G_1,*O*), respectively, relative to the point *O*. A central ray which passes through the origin of the lens is represented by $\overrightarrow{F_1OM}$. $\overrightarrow{F_1PQK}$ represents any other ray which originates from the point F_1. F_1, F_2, and G_1 are points of perfect focus for radiation at angles to the axis of -α, +α, and 0°, respectively. The electrical wavelength λ_g in the lens is approximated to $\lambda_o/\sqrt{\varepsilon_r}$, and λ_g in microstrip line is $\lambda_o/\sqrt{\varepsilon_{eff}}$. So these electrical wavelengths should be considered in derivation of lens equations. The equations for optical path-length equality between a general ray and the ray through the origin become

$$\overrightarrow{(F_1P)}+\frac{\sqrt{\varepsilon_{eff}}}{\sqrt{\varepsilon_r}}S+\frac{1}{\sqrt{\varepsilon_r}}A\sin\alpha=F+\frac{\sqrt{\varepsilon_{eff}}}{\sqrt{\varepsilon_r}}S_o, \tag{A1}$$

$$\overrightarrow{(F_2P)}+\frac{\sqrt{\varepsilon_{eff}}}{\sqrt{\varepsilon_r}}S-\frac{1}{\sqrt{\varepsilon_r}}A\sin\alpha=F+\frac{\sqrt{\varepsilon_{eff}}}{\sqrt{\varepsilon_r}}S_o, \tag{A2}$$

and

$$\overrightarrow{(G_1P)} + \frac{\sqrt{\varepsilon_{eff}}}{\sqrt{\varepsilon_r}} S = G + \frac{\sqrt{\varepsilon_{eff}}}{\sqrt{\varepsilon_r}} S_o \tag{A3}$$

where

$$\overrightarrow{(F_1P)^2} = F^2 + X^2 + Y^2 + 2FX\cos\alpha - 2FX\sin\alpha, \tag{A4}$$

$$\overrightarrow{(F_2P)^2} = F^2 + X^2 + Y^2 + 2FX\cos\alpha + 2FX\sin\alpha, \tag{A5}$$

and

$$\overrightarrow{(GP)^2} = (G+X)^2 + Y^2. \tag{A6}$$

$\overrightarrow{F_1P}$, $\overrightarrow{F_2P}$, and $\overrightarrow{GP}$ are the path lengths from focal points F_1, F_2, and G_1, respectively, to the point P on the inner lens contour. A set of parameters which are normalized relative to the focal length F is now defined,

$$x = \frac{X}{F},\ y = \frac{Y}{F},\ g = \frac{G}{F},\ \eta = \frac{A}{F},\ s = \frac{S}{F},\ a_O = \cos\alpha,\ b_O = \sin\alpha.$$

Eqs. (A4) to (A6) become

$$\frac{\overrightarrow{(F_1P)^2}}{F^2} = 1 + x^2 + y^2 + 2a_o x - 2b_o y,$$

$$\frac{\overrightarrow{(F_2P)^2}}{F^2} = 1 + x^2 + y^2 + 2a_o x + 2b_o y,$$

and

$$\frac{\overrightarrow{(GP)^2}}{F^2} = (g+x)^2 + y^2.$$

The normalized forms of (A1) and (A4) are now combined.

$$\frac{\overrightarrow{(F_1P)^2}}{F^2} = (1-\frac{\sqrt{\varepsilon_{eff}}}{\sqrt{\varepsilon_r}}s-\frac{1}{\sqrt{\varepsilon_r}}b_o\eta)^2$$
$$= 1+\frac{\varepsilon_{eff}}{\varepsilon_r}s^2+\frac{1}{\varepsilon_r}b_o^2\eta^2-\frac{1}{\sqrt{\varepsilon_r}}2b_o\eta+\frac{\sqrt{\varepsilon_{eff}}}{\varepsilon_r}2b_o s\eta-\frac{\sqrt{\varepsilon_{eff}}}{\sqrt{\varepsilon_r}}2s \qquad \text{(A7)}$$
$$= 1+x^2+y^2+2a_o x-2b_o y.$$

Since the off-axis focal points are located symmetrically about the center axis, the lens contours must also be symmetrical. Therefore, (A7) remains unchanged and can be separated into two independent equations if η is replaced by $-\eta$ and y by $-y$. One equation contains only odd powers of y and η while the other contains the even terms. Thus,

$$-\frac{1}{\sqrt{\varepsilon_r}}2b_o\eta+\frac{\sqrt{\varepsilon_{eff}}}{\varepsilon_r}2b_o s\eta=-2b_o y\,, \qquad \text{(A8)}$$

or

$$y=\frac{1}{\varepsilon_r}\eta(1-\frac{\sqrt{\varepsilon_{eff}}}{\sqrt{\varepsilon_r}}s)\,.$$

also,

$$x^2+y^2+2a_o x=\frac{\varepsilon_{eff}}{\varepsilon_r}s^2+\frac{1}{\varepsilon_r}b_o^2\eta^2-\frac{\sqrt{\varepsilon_{eff}}}{\sqrt{\varepsilon_r}}2s\,. \qquad \text{(A9)}$$

Eqs. (A3) and (A6), relating to the on-axis focus, are likewise combined.

$$\frac{\overrightarrow{(GP)^2}}{F^2}=(g-\frac{\sqrt{\varepsilon_{eff}}}{\sqrt{\varepsilon_r}}s)^2=(g+x)^2+y^2\,, \qquad \text{(A10)}$$

or

$$x^2 + y^2 + 2gx = \frac{\varepsilon_{eff}}{\varepsilon_r} s^2 - \frac{\sqrt{\varepsilon_{eff}}}{\sqrt{\varepsilon_r}} 2gs \,. \tag{A11}$$

After algebraic manipulation, (A9) and (A11) give the following relation between s and η:

$$as^2 + bs + c = 0 \tag{A12}$$

where

$$a = \left[1 - \frac{1}{\varepsilon_r}\eta^2 - \left(\frac{g-1}{g-a_o} \right)^2 \right] \frac{\varepsilon_{eff}}{\varepsilon_r},$$

$$b = \left[2g\left(\frac{g-1}{g-a_o} \right) - \frac{(g-1)}{(g-a_o)^2} \frac{1}{\varepsilon_r} b_o^2 \eta^2 + \frac{1}{\varepsilon_r} 2\eta^2 - 2g \right] \frac{\sqrt{\varepsilon_{eff}}}{\sqrt{\varepsilon_r}}$$

and

$$c = \left[\frac{1}{\varepsilon_r} \frac{g b_o^2 \eta^2}{g-a_o} - \frac{1}{\varepsilon_r^2} \frac{b_o^4 \eta^4}{4(g-a_o)^2} - \frac{1}{\varepsilon_r} \eta^2 \right].$$

For fixed values of design parameters α and g, s can be computed as a function of η from (A12). These values of s and η are substituted into (A8) and (A11) to determine x and y, completing the solution for the lens design.

APPENDIX B

LENS CONTOUR CALCULATIONS AND PHASE ABERRATIONS

The variables x, y, and s as a function of η have been computed for the straight-front-face lens design from (A8), (A11), and (A12), and are listed for the following parameters: α=30°, F=2.7λ_o, g=1.1, η=0 < 0.6λ_o > 3.0λ_o, and r=R/F=0.651. The value of g has been selected to optimize the lens design for the given scan angle α. This lens contour drawn from Table B1 is shown graphically in Fig. B1.

Table B1. The calculated lens contour [mil]

η	S	-X	Y
0	0	0	0
236.2	3.5	14.0	158.1
472.4	13.7	56.0	313.3
708.7	28.9	125.2	463.6
944.9	43.3	219.3	610.1

This procedure gives the lens which has three perfect focal points corresponding to the angles $\pm\alpha$ and 0°. For wide-angle scanning the lens must focus well, not only at these three points, but also at all intermediate angles along the focal arc. However, the equation does not guarantee the optical aberration of zero at intermediate angles. The optical aberrations of the lens are defined as the difference in path lengths between a central ray through the origin and any other ray, both of which are traced from an arbitrary point on the focal arc through the lens and terminate normal to the emitted wavefront.

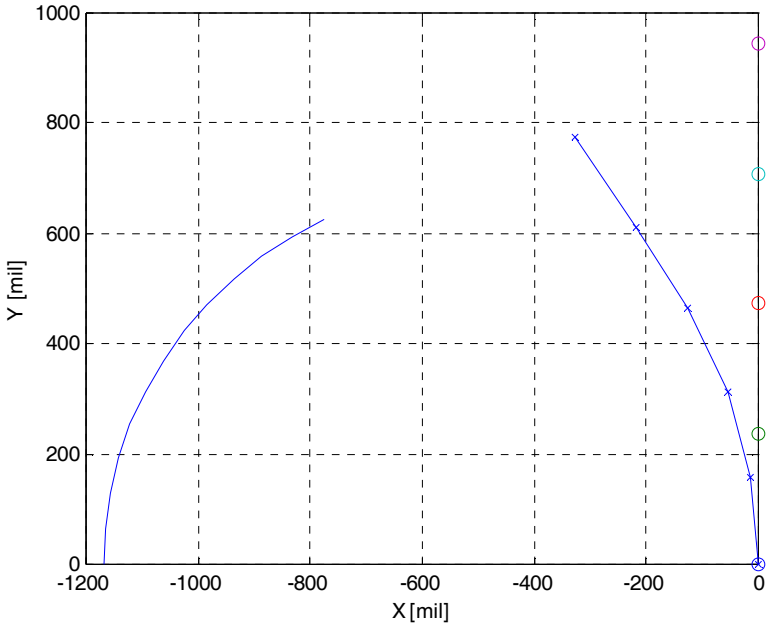

Fig. B1. The lens contour.

This path length error is a function both of the scan angle θ and the position along the lens contour η, and may be derived geometrically [in a manner similar to that of (A1) through (A6)] from Fig. A1 as

$$\Delta l = \frac{\Delta L}{F} = (h^2 + x^2 + y^2 + 2hx\cos\theta - 2hy\sin\theta)^{0.5} - h + \frac{\sqrt{\varepsilon_{eff}}}{\sqrt{\varepsilon_r}} s + \frac{1}{\sqrt{\varepsilon_r}} \eta \sin\theta \qquad \text{(B1)}$$

where ΔL is the path length error and $h(=H/F)$ is the normalized distance from a point on the focal arc to the origin O of surface Σ_1. H is computed by the law of cosines from the triangle with sides R, H, and $(G\text{-}R)$, and included angle θ; θ is the angle between central axis and an arbitrary point on the focal arc, and R is the radius of the focal arc which is determined by the three points G_1, F_1, and F_2.

Fig. B2 shows the calculated path length errors as a function of θ. The maximum error is less than 2×10^{-3} cm at θ =17.5°. This error gives negligible effect on the radiation pattern as affirmed in the calculation of array factor.

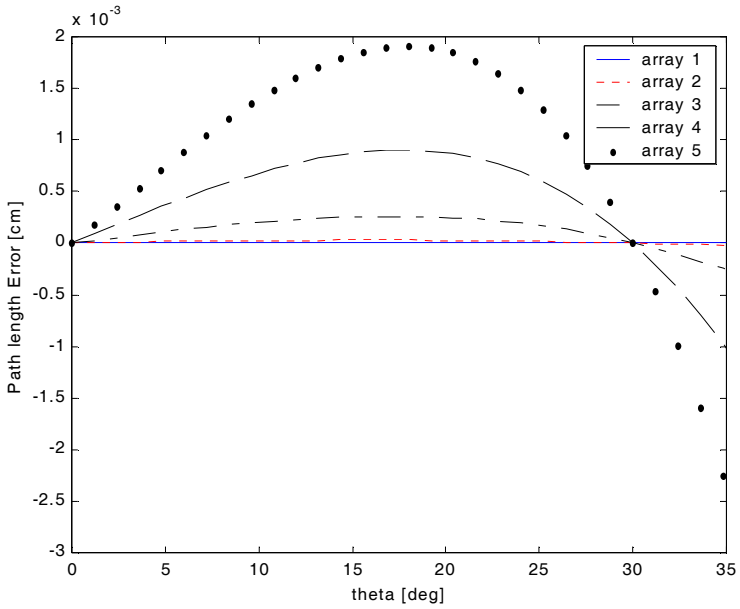

Fig. B2. The calculated path length errors.

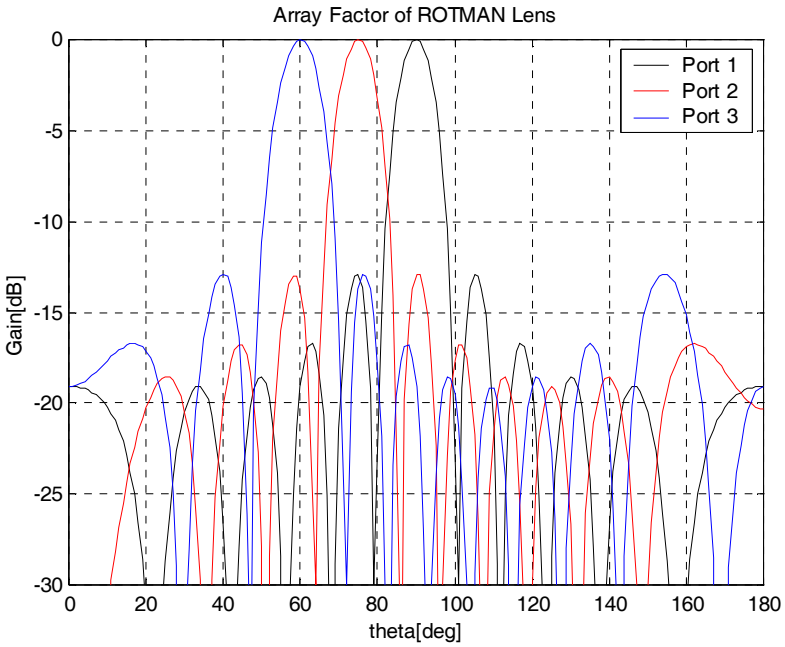

Fig. B3. The calculated array factor located at 30, 15, and 0°.

VITA

Sang Gyu Kim was born in Taegu, Republic of Korea on Oct. 9, 1967. He received a Bachelor of Science degree and a Master of Science degree in electronic engineering from Kyungpook National University in Feb. 1991 and Feb. 1993, respectively. He joined SK Telecom where he worked to develop and optimize a code-division-multiple-access (CDMA) cellular system and IMT-2000 system until 2000. Next, he started working towards his Ph.D. degree in electrical engineering at Texas A&M University, College Station, TX, and was directed by Dr. Kai Chang in the Electromagnetics and Microwave Laboratory. His graduate research projects have been supported by grants from the U.S. Army, the NASA Glenn Research Center, the Texas Telecommunications and Informatics Task Force (TITF), and the National Science Foundation. His primary research interests include passive and active microwave circuits, wideband and multiple-beam phased-array antenna systems, and CDMA system engineering.

He can be reached through Professor Kai Chang, Department of Electrical Engineering, Texas A&M University, College Station, TX 77843-3128.